Synthesis of Ti_2AlC, Ti_3AlC_2 and Ti_3SiC_2 MAX phase ceramics; and their composites with c-BN.

By:

Tokoloho Rampai

Centre for Materials Engineering

University of Cape Town

Supervisor:

Professor C. Lang

Centre for Materials Engineering

University of Cape Town

Special field: Ceramics

October 2011

Dissertation in full fulfilment of the requirements for the degree of M.Sc. (Materials Engineering)

PLAGIARISM DECLARATION

1. I know that plagiarism is wrong. Plagiarism is to use another's work and pretend that it is one's own.

2. I have used the numbering system for citation and referencing. Each contribution to, and quotation in, this thesis from the work(s) of other people has been attributed, and has been cited and referenced.

3. This dissertation is my own work.

4. I have not allowed, and will not allow, anyone to copy my work with the intention of passing it off as his or her own work.

Signature _____

Date _____

ACKNOWLEDGEMENTS

Firstly I would like to say thank you to the all powerful, all loving and the Almighty God, for His unconditional love for me and His light and protection in my hardest and darkest days. The angels He sent my way whenever I needed comfort or guidance or help getting through troublesome times, for this and all other things, I thank You and know that I was never alone.

My deepest thanks go to my supervisor, Professor Candace Lang, for her time, patience, encouragement and never ending support for everything I do and everything I am. She has inspired me beyond expectations; I am motivated to achieve beyond my wildest dreams. Prof. I feel you should know that you have become my idea of what a woman today ought to be, caring, patient, loving, inspiring and most importantly, fiercely intelligent. If I am half the woman you are by the end of my days, I will be content.

I would also like to thank Dr. M. Herrmann for his endless and bottomless well of knowledge and his willingness to share it. Your guidance to me was priceless and more valuable than you could ever know. To Prof. I. Sigalas I would like to say thank you for your time and direction which you gave without difficulty. To Wits and Element Six (Pty) Ltd, I would like to convey my heartfelt gratitude for allowing me to use your facilities, resources and staff during my research.

I would also like to thank the Centre of Excellence in Strong Materials (CoE-SM), the department of Science and Technology (DST), and Element Six (Pty) Ltd for showing enough belief in me to provide financial support to enable the whole project to come to life. To UCT, I would like to say thank you for nurturing me and moulding me into an exceptional member of society. And also to the Centre for Materials Engineering and my colleagues there, I would like to say thank you, you are all magnificent and this has made the centre my home.

My special thanks go to my colleagues from the school of Chemical and Metallurgical Engineering, at Wits. To Peter (Peter-paedia), thank you for your intellectual and technical help whenever I needed it. To Amanda (Manda-panda) thank you for all the help you have given me, professional, academic and most importantly personal (I am lucky to have known you).

And lastly I would like to thank my family. Hopolang; you have changed my life for the better, you have added endless days of sunshine in my life and thank you for always waking up with a smile. Sesi, thank you for everything you have done for us since mom and dad passed away, we really do appreciate it. Ramranky, thank you for everything you have done for me since the first day I came to UCT, you have truly changed my life. Hlu, thank you for always reminding us that life is worth living with a smile, you will forever be my smooch!

ABSTRACT

MAX phase ceramics are ternary ceramics with both metallic and ceramic properties. The existing backing materials in grinding wheels can be made of ceramics or metals. In these applications, ceramics have the disadvantage of low toughness, and most metals have the disadvantages of relatively high density and intolerance to some very high temperatures. The MAX phases have a combination of the main advantages of both metals and ceramics: they are soft and machinable yet also heat-tolerant, strong and lightweight. Cubic boron nitride (c-BN) is a widely used abrasive in grinding wheels, which is exceeded in hardness only by diamond. Composites of c-BN and selected MAX phases may result in materials of some interesting and useful properties for application in industry.

Firstly MAX phases, Ti_3SiC_2; Ti_3AlC_2 and Ti_2AlC were synthesised, then reaction couples of MAX-cBN are made in order to investigate the best conditions for composite synthesis, and to analyse the interfacial phases which occur. Finally, the MAX-cBN composites were synthesised from the reaction couple studies. The following results were obtained:

1. Samples synthesised to obtain Ti_3AlC_2 were largely composed of the Ti_2AlC, and thus synthesis of the Ti_3AlC_2 MAX phase was deemed unsuccessful.
2. Nearly pure samples of Ti_2AlC and Ti_3SiC_2 were successfully synthesised with high densities, 99.16% and 98.21%, respectively, of the theoretical density.
3. Reaction couple studies revealed that the Ti_3SiC_2/c-BN couple was successfully made at 1400°C, 10MPa pressure for 30 minutes, and Ti_2AlC/c-BN couple was successfully made at 1500°C, 10MPa pressure for 30 minutes. The interfacial phases characterised by XRD and SEM found here were TiN, TiC, TiB_2 and AlN for the latter and TiN, TiS_2 and TiB_2 for the former.
4. These conditions were used to successfully synthesise MAX/c-BN composites where both could react and still remain intact. The interfacial phases characterised by XRD and SEM found here were TiAl, TiC, TiB_2 and AlN for Ti_2AlC/c-BN and TiN, TiC, TiS_2 and TiB_2 for Ti_3SiC_2/c-BN.

From these results the following conclusion was drawn:

- Ti_2AlC and Ti_3SiC_2 are fully compatible with c-BN in order to synthesise a composite with notable properties such as the fracture toughness, suggested by the observed fracture mechanism seen from the fracture surface of these composites.

TABLE OF CONTENTS

LISTOF ILLUSTRATIONS

LIST OF FIGURES

LIST OF TABLES

LIST OF EQUATIONS

GLOSSARY

IKB	Incipient Kink Band
KBs	Kink Boundaries
KNE	Kinking Nonlinear Elastic
CG	Coarse Grained
FG	Fine Grained
NMEs	Nonlinear Mesoscopic Solids
RRR	Residual Resistivity Ratio
TEC	Thermal Expansion Coefficients
DTA	Differential Thermal Analysis
CVD	Chemical Vapour Deposition
HIP	Hot Isostatic Pressing
HP	Hot Pressing
c-BN	cubic Boron Nitride
h-BN	hexagonal Boron Nitride
w-BN	wurtzite Boron Nitride
Topotactic	internal atomic displacements, which may include loss or gain of material, so that the initial and final lattices are in coherence

CHAPTER ONE:
INTRODUCTION

1.1 Background to the study

The MAX Phases, which are novel carbide and nitride ternary ceramics, have a combination of the main advantages of both metals and ceramics: they are soft and machinable yet also heat-tolerant, strong and lightweight. This combination of properties is mainly due to the layered crystal structures of the MAX phases, which endow the materials with high fracture toughness. Composites of these materials and traditional ceramics could have applications which can prove to be very beneficial to industry.

Ceramic materials are known to be the most convenient option for high temperature, wear or corrosive applications. They are known to have low reactivity, high hardness and relatively low density; these advantages are however coupled with one major disadvantage - the low toughness. Metals, conversely, are generally machinable, have a better toughness than ceramics, and conduct heat efficiently. Most metals, nevertheless, are heavy and are not tolerant to some very high temperatures.

Cubic boron nitride (c-BN) is a widely used abrasive in grinding wheels, which is exceeded in hardness only by diamond [1]. Unlike diamond, c-BN is not chemically reactive with ferrous materials; in fact; it is chemically inert in the presence of ferrous metals up to 1227-1327°C [2]. Sintered c-BN grinding wheels allow ferrous metals, chilled cast irons and hardened steels to be machined [2]. Carriers for abrasives are generally made out of materials which are easy to machine to the required shapes. In most cases, the compacted c-BN powder is cemented on tungsten carbide or ceramic substrates. Grinding wheels typically have abrasive bodies embedded, at least partially, into a carrier material. Figure 1.1 shows a disc shaped grinding wheel, where A is the grinding surface which contains the abrasive bodies, B is the carrier body and C is a central bore which serves as a connection region to the motor [1].

Figure 1. 1: Resin grinding wheel with the resin abrasives found in region A (after ECVV.com [3]).

The disadvantage of some current grinding wheels is that the known carrier materials can be used in a very limited range of conditions. Depending on the degree of hardness of the work piece being cut, the carrier material can be either too hard or too soft, which leads to an unfavourable grinding power of the abrasive body embedded in the carrier material. This is observed in many applications in which the temperature increases during the machining process. With the increase in temperature the carrier material weakens, which can lead to a loss of the abrasive bodies during the grinding process or, alternatively, to a further penetration of the abrasive bodies into the carrier material. A drawback of tools with metallic carrier materials, such as materials containing iron or copper, is very high friction between the carrier material and the work piece. The binding of the abrasive bodies with the carrier material is not always sufficiently strong, resulting in reduced grinding power of the grinding wheel [1].

1.2 Problems to be investigated

The MAX phase ceramics decompose at elevated temperature and ambient pressures (from 850°C to above 2300°C)[4,5,6], depending on the type and degree of impurities. c-BN diffusion processes occur at such temperatures because the covalent bonds are strong and need higher temperatures to break or rearrange. Therefore the aim of the work presented here is to find a temperature low enough where the MAX phases have not decomposed but high enough to start the reaction of the c-BN to synthesis a MAX phase/c-BN composite. (Otherwise we have a decomposed MAX and a non reacted cBN.) A second problem to be investigated is the compatibility of selected MAX phases with c-BN and the stability of the composite.

1.3 Hypothesis

It is possible to make the MAX phase ceramics which are (a) thermodynamically stable, and (b) compatible with c-BN in composites.

.

CHAPTER TWO:
LITERATURE REVIEW

2.1 The MAX phase ceramics

Jeitschko and Nowotny [7] first synthesized Ti_3SiC_2 in 1967 and determined its structure, from a non-fully pure sample. Initial suggestions that Ti_3SiC_2 was not a typical carbide came in 1972, when Nickl *et al.* [8], working on chemically vapour deposited films of Ti_3SiC_2, showed that it was anomalously soft for a carbide. The fabrication of single-phase, bulk samples however proved challenging; Pampuch [9] fabricated samples that were about 85 percent pure by volume in 1989. Using these samples, Pampuch showed that Ti_3SiC_2 was almost three times as stiff as titanium metal (with the same density) [10,11].

Barsoum and co-workers synthesized Ti_3SiC_2, reporting that it was stiff, lightweight, machinable, made from relatively inexpensive raw materials, resistant to oxidation and thermal shock, and capable of remaining strong up to temperatures in excess of 1300°C in air [10]. In addition, they also identified more than 50 closely related compounds [10], named $M_{n+1}AX_n$ or "MAX" phases because of their composition, as shown in figure 2.1(a) [10].

MAX phases are unique carbide and nitride ternary ceramics with the general formula $M_{n+1}AX_n$, where:
M - early transition metals (red in the periodic table in figure 2.1 (a))
A - group A elements, usually IIIA and IVA (dark blue in the periodic table in figure 2.1 (a))
X - C or N (black in the periodic table in figure 2.1 (a))
and n is 1, 2 or 3, as shown in 2.1 (b) [10].

These materials, synthesised by different researchers over the years, naturally form three groups based on the ratio of atoms of the M, A and X elements, the 211, 312, and 413 classes [10].

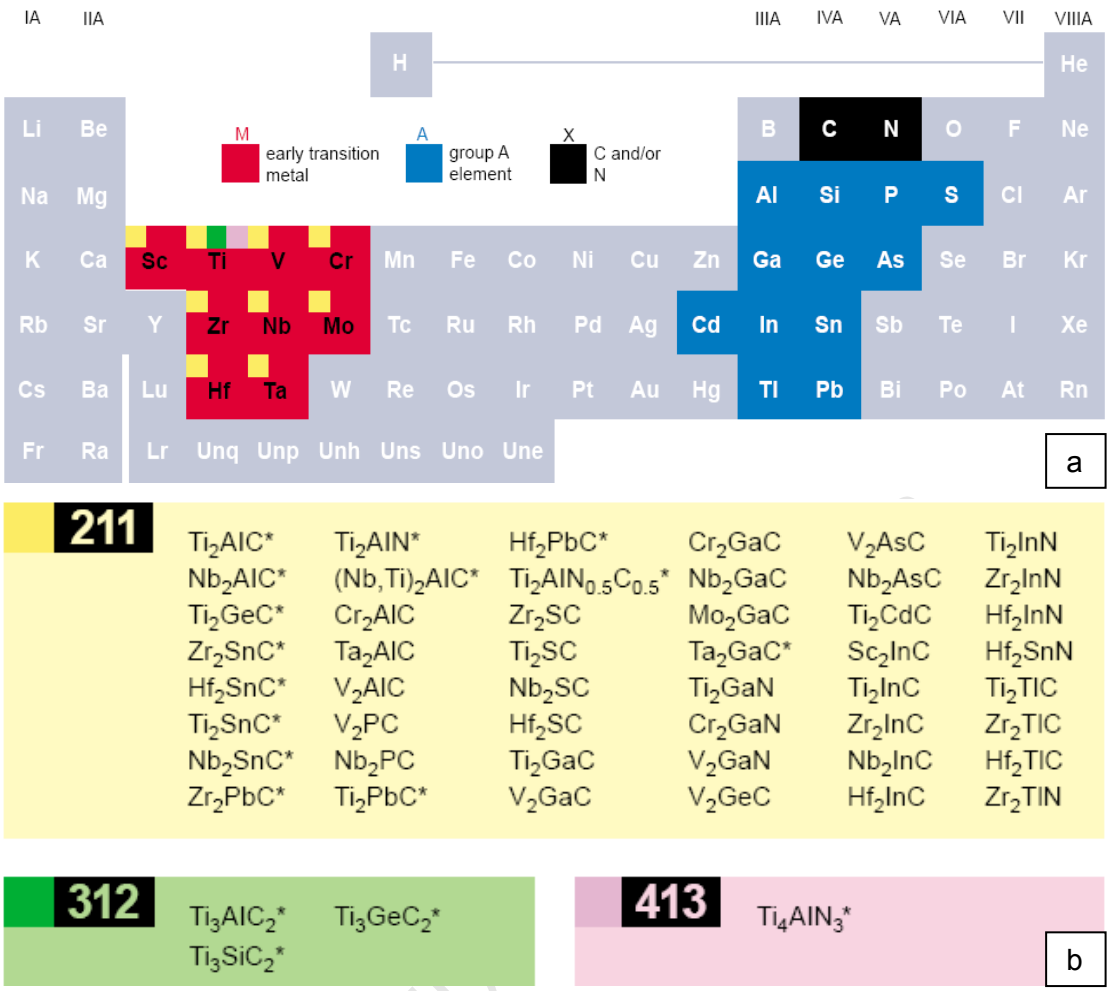

Figure 2. 1: Periodic table illustrating the designation of the MAX phases (a), and their three classes (b). (After Barsoum and El-Raghy, who synthesised the materials marked with asterisks [10]).

Barsoum and El-Raghy [10] report that these materials are in general stiff, lightweight, machinable, and resistant to oxidation and thermal shock. Ti_3SiC_2 for example, like a metal is deformable, machinable, thermally and electrically conductive, resistant to thermal shock and plastic at elevated temperatures. Like a ceramic it is refractory (its decomposition temperature is greater than 2000°C), oxidation resistant, quite stiff and relatively light (4.5 grams per cubic centimetre). Its thermal expansion is also relatively low, similar to typical ceramics [10].

2.1.1 Structure and bonding

The crystal structure of the MAX phases is hexagonal, with almost close-packed M layers interleaved with layers of a pure group A element, and the X atoms filling the octahedral sites between the M and A layers. The M6X octahedra are identical to those found in the rock salt structure of the corresponding binary MX carbides (e.g. Ti_2AlC and TiC). The A-group elements are located at the centres of trigonal prisms that are slightly larger, and thus better able to accommodate the larger A-atoms, than the octahedral sites. The A-group is found every third layer in the 211 compounds, every fourth layer in the 312 compounds and every fifth layer in the 413 compounds, figure 2.2 [10].

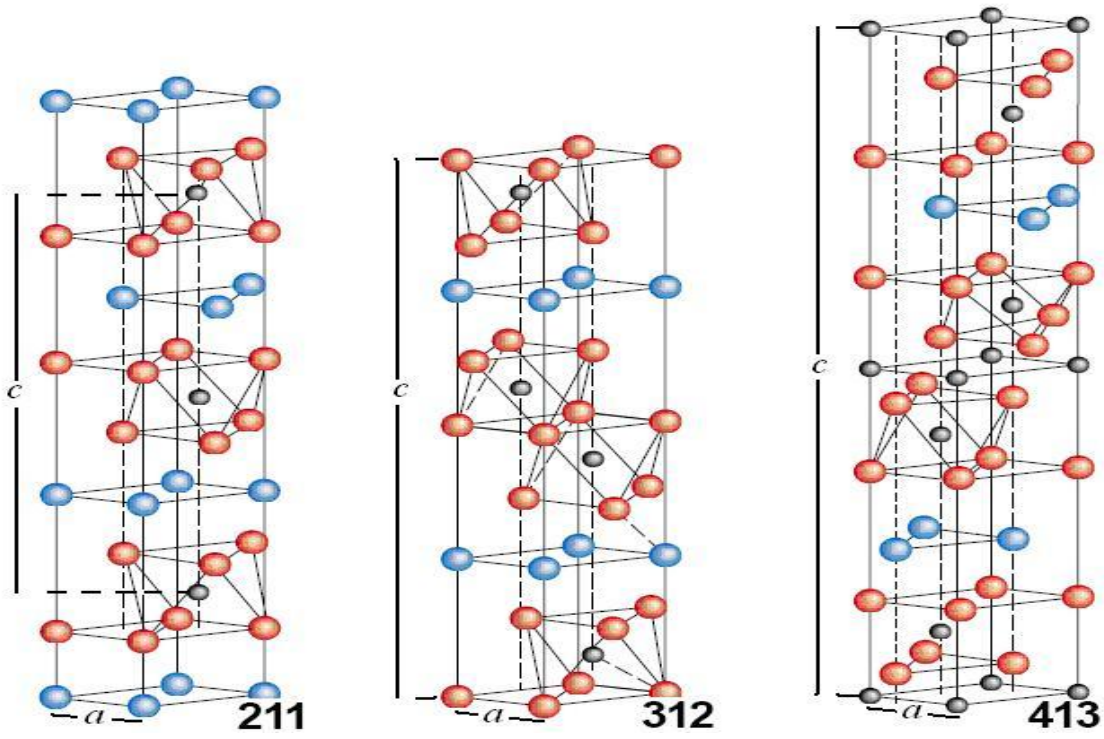

Figure 2. 2: The crystal structures of the three classes of MAX phases. M group atoms are red; A Group atoms are blue and X group atoms are black. (After Barsoum and El-Raghy [10]).

Given the close chemical and structural similarities of the MAX and MX phases (Ti_2AlN and TiN for example), a similar approach to describing the structure is commonly used. In the MAX phases, like the MX phases, it is useful to consider the ternary MAX phases to be interstitial compounds in which the A-and X-atoms fill the interstitial sites between the M-atoms [10]. In such a scheme, the *c*-parameter of the 211 phases, comprising four M-layers per unit cell (figure

2.2), should be ≈ 4 times the *a*-parameter, for a *c/a* ratio of ≈4, as observed. Similar arguments for the 312 phases, with six M-layers per unit cell, predict a *c/a* ratio of ≈ 6, and the 413 phases a *c/a* ratio of ≈ 8. The actual *c/a* ratios are, respectively, ≈ 5.8, -6 and 7.8, supporting the notion of interstitial compounds. The lattice parameters and theoretical density of selected MAX phases are shown in Table 2.1 [10].

Table 2. 1: Summary of some selected MAX phases, their theoretical densities and lattice parameters in brackets (after Barsoum [10]).

IIIA	IVA	VA	VIA
Al	Si	P	S
Ti_2AlC, 4.11 (3.04, 13.60)			Ti_2SC, 4.62 (3.216, 11.22)
V_2AlC, 4.82 (2.914, 13.19)		V_2PC, 5.38 (3.077, 10.91)	Zr_2SC, 6.20 (3.40, 12.13)
Cr_2AlC, 5.24 (2.86, 12.8)	Ti_3SiC_2, 4.52 (3.0665, 17.671)	Nb_2PC, 7.09 (3.28, 11.5)	$Nb_2SC_{0.4}$ (3.27, 11.4)
Nb_2AlC, 6.50 (3.10, 13.8)			Hf_2SC (3.36, 11.99)
Ta_2AlC, 11.82 (3.07, 13.8)			
Ti_2AlN, 4.31 (2.989, 13.614)			
Ti_3AlC_2, 4.5 (3.075, 18.578)			
Ti_4AlN_3, 4.76 (2.988, 23.372)			

2.1.2 Microstructure

The microstructure of the MAX phases reveals a layered structure which forms kink boundaries when dislocations form and slide across one another, in opposite directions under stress. Kink bands typically form when layered materials are loaded parallel to the layers. Any cracks that start to separate the layers are arrested by the kink boundaries, the cracks extending only into the area defined by the kink boundaries and not beyond them, as shown in figure 2.3 [10].

Barsoum [10] describes the formation of kink bands by this analogy: to form a kink band, stand a deck of cards on one end and carefully add weight on top. For small loads, the cards will buckle elastically (if the load is removed, the cards snap back to their original shape). However, at a maximal load the cards will buckle irreversibly, forming one or more kink bands where the layers bend sharply and remain bent. For a kink band to form, part of the crystal that is forming the kink band must be able to glide relative to the part that is not; furthermore, the layers must detach from each other [10].

Unlike metals, MAX phases do not distort by plastic deformation, but rather by breaking off of microscopic flakes from the surface. Even after the initiation of damage, the MAX phases can still carry substantial loads because of the damage tolerance which is built into the structure at the atomic level. In most ceramic materials, once damage is initiated, the point of damage becomes weaker, resulting in further damage and further weakness and eventually rupture [10].

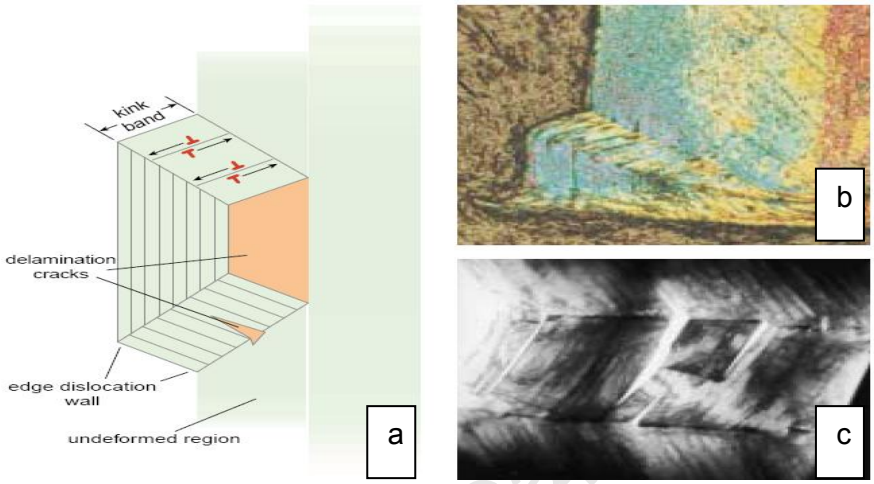

Figure 2. 3: Illustration of the kink bands seen in the microstructure of MAX phases. (After Barsoum and El-Raghy [10]).

Transmission electron microscopy (TEM) [12,13] and high-resolution transmission electron microscopy (HRTEM) [12,14] studies of Ti_3SiC_2 revealed the presence of only perfect dislocations lying in the basal planes with a Burgers vector b = $\frac{1}{3}\langle 11\bar{2}0\rangle$ or 1.54 Å in length. Every dislocation is of a mixed nature with an edge and screw component [14,15,16]. Barsoum and Randovic [9] observed that to understand the mechanical properties of the MAX phases it should also be understood that only basal plane dislocations exist. These dislocations are mobile and multiply, even at temperatures as low as -196°C. Because they are confined to the basal planes, the dislocations arrange themselves either in arrays (pileups) on the same basal planes (figure 2.4 (a)), or in walls (low- and high-angle grain boundaries) normal to the basal planes (4(a)). The walls have both tilt and twist components [14,15,16].

In Figure 2.4 (a) both dislocation walls and pile-ups are confined to the basal planes. The + and - signs denote the orientations of the screw dislocations in the wall. Dislocation interactions, other than orthogonal are very unlikely to occur, and have not been reported to date. This fact has

very far-reaching ramifications, in that substantial deformation can now occur without work hardening in the classic sense. Given that non-basal dislocations would have Burgers vectors >*c* (viz.>11–23 Å), their presence is highly unlikely. Furthermore, as a result of their high *c*/*a* ratios, twinning is unlikely [15,17].

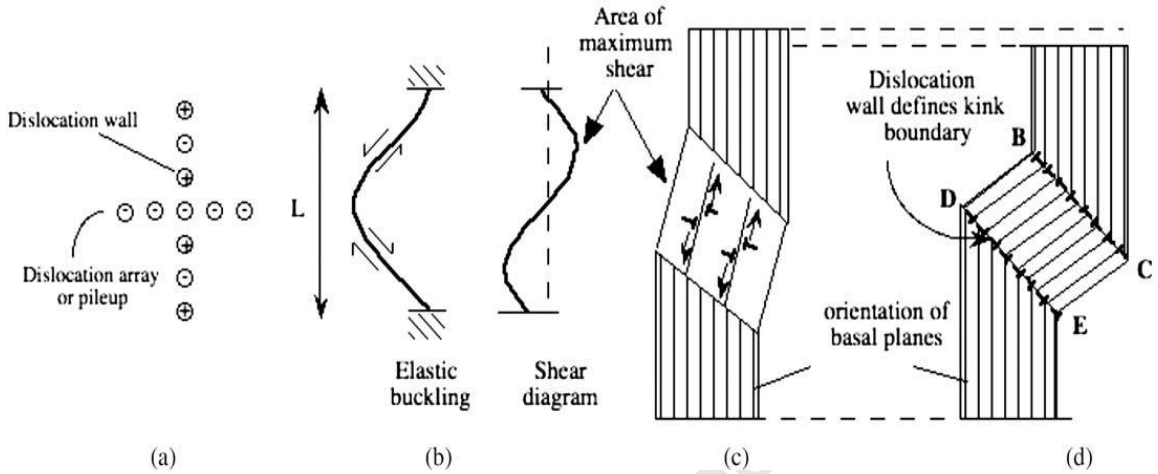

Figure 2. 4: Schematic view of (a) dislocation walls (vertical) and pile-ups (horizontal) in the MAX phases, (b) elastic buckling and corresponding shear diagram, (c) initiation of pairs of dislocations in areas of maximum shear, (d) KB and kink boundaries comprised of edge dislocations of one sign giving rise to a stove-pipe shape. (After Barsoum and Radovic [9]).

Farber *et al*. [12] and Barsoum and Radovic [15] observed stacking faults in addition to dislocations in the MAX phase ceramics. The stacking faults are typically growth defects, where locally an Si plane is missing and the stacking twin symmetry is broken so that thin lamella with an $M_{n+1}X_n$ chemistry remain with identical stacking to [111] in the rock salt structure [15,16,18]. All stacking faults and their bounding dislocations also lie in basal planes with their displacement vectors parallel to [0001] [12,15,18]. Grain boundaries are another planar defect present in polycrystalline samples, but their structure is still largely an open question [15].

2.1.3 Mechanical properties of MAX phases

Mechanically, the MAX phases are relatively soft (hardness of 1–5 GPa) and are readily machinable, thermal shock resistant, and damage tolerant. Moreover, some MAX phases are resistant to fatigue, creep, and oxidation. At certain higher temperatures, MAX phases go through a ductile-to-brittle transition. At room temperature, they can be compressed to stresses

as high as 1 GPa and fully recover upon removal of the load, while dissipating 25% of mechanical energy [9,16].

Delaminations in layered solids—from fibre composites to geologic strata—can lead to catastrophic failure in critical situations. Therefore, the role which kink boundaries (KBs) play in suppressing delaminations in the MAX phases is significant. This comes about because delaminations in layered structures with kink boundaries present can only advance if the entire wall or kink boundary also moves. This is energetically very costly and becomes more so as the angle of delamination becomes steeper [13,15,19,20].

The damage tolerance of the MAX phases discussed arises from their deformation mechanism at the atomic level. In the next section, reference will be made mostly to two different microstructures, fine-grained (3–5 μm) and coarse-grained (plate-like grains, 50–200 μm in diameter and 5–20 μm thick) [15].

2.1.3.1 Room Temperature Response of MAX phases to stress

2.1.3.1.1 Compression Behaviour of Quasi-single Crystals and Polycrystals

When highly oriented, quasi-single crystal macro-grained samples of Ti_3SiC_2 (≈2 mm in diameter) are tested in compression the response is reported to be anisotropic [19]. When the basal planes are oriented in a way that allows for slip (x-direction in inset in figure 2.5) the samples yield at ≈200 MPa and deformation occurs by the formation of shear bands (not shown) [15].

By contrast, when the slip planes are parallel to the applied load (z-direction in inset in Figure 2.5), and deformation by ordinary dislocation glide is impossible, the stress–strain curves show clear maxima at stresses between 230 MPa and 290 MPa, followed by a region of strain softening and finally recovery [15]. In this case, the deformation occurs by a combination of KB formation at the corners of the tested cubes, delaminations within individual grains, and ultimately, shear band formation as shown in figure 2.6. Note that the KB visible on the bottom left-hand side of the cube figure 2.6 did not result in the total delamination of the outermost grain in which it was initiated. This observation was taken to be the first micro-structural evidence that KBs in MAX phases are potent suppressors of delamination [15,19].

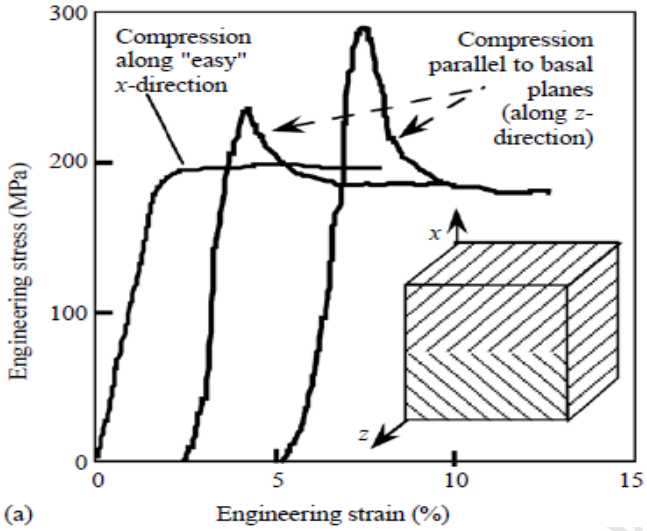

Figure 2. 5: Engineering stress–strain curves of 2 mm cubes of highly oriented samples of Ti_3SiC_2. Inset shows schematic of cube and basal plane orientations. (After Barsoum and Radovic [15]).

Polycrystalline samples of Ti_3SiC_2 subjected to compressive loads and temperatures up to ≈900°C fail in a quasi-brittle manner by shearing at roughly 45° to the loading axis [15]. Not all MAX phases fail suddenly; most exhibit gradual failure characteristics in that the stress–strain curves exhibit an inverted shallow V, rather than a sharp drop at a maximum stress [15,21,22]. The failure mode remains shear failure across a plane; Barsoum speculates that enough ligaments reach across the plane to result in a less sudden loss in load bearing capability. This tendency increases with increasing grain size and reduced loading rates [15].

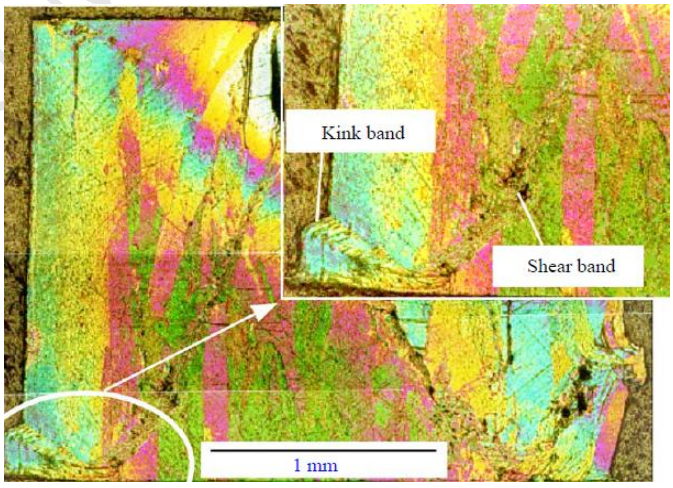

Figure 2. 6: Light micrograph of polished and etched sample after deformation parallel to the basal planes. Note kinking at corners. (After Barsoum and Randovic [15]).

2.1.3.1.2 Hardness and Damage Tolerance

The hardness values of polycrystalline MAX phases fall in the relatively narrow range of 1–5 GPa. They are thus softer than most structural ceramics, but harder than most metals [15,23]. The low hardness persists—at least in Ti_3SiC_2—even at temperatures as low as -196°C [15,24]. Working with CVD single crystals, Nickl *et al*. [8] were the first to note that the hardness of Ti_3SiC_2 was anisotropic and higher when loaded along the *c*-direction. This was later confirmed by Goto and Hirai [25], who also were the first to show that the hardness was a function of indentation load. Both observations are characteristic of the MAX phases [15,23]. With decreasing load, the hardness increases (figure 2.7, top curve) and below a certain load it is not measurable, since no trace of the indentations is found[15].

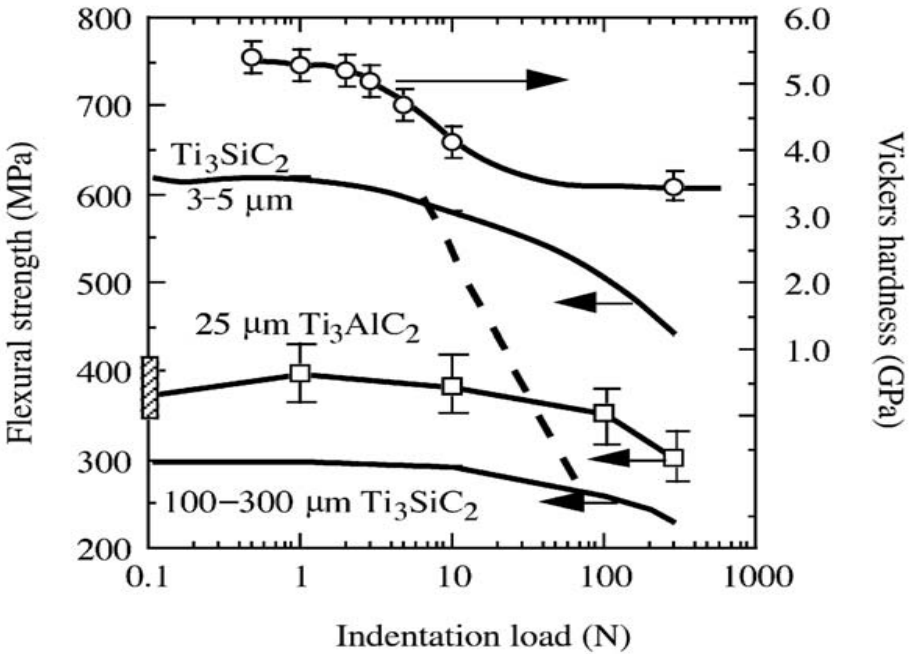

Figure 2. 7: Vickers hardness versus indentation load (top curve) of CVD single crystal of Ti_3SiC_2: four-point flexural strength vs. indentation loads for fine- and coarse-grained Ti_3SiC_2 and Ti_3AlC_2 with α ≈25 μm grain size. The inclined dashed line is expected behaviour for brittle solids. (After Tzenov and Barsoum [21]).

Given their plastic anisotropy, the response of MAX phases to nano-indentations is anisotropic: when the basal planes are parallel to the surface, the extent of plastic deformation is higher than if the basal planes are loaded edge-on [15]. In the former case, it is easier to form KBs because

the top surface is unconstrained [15,16,26]. The damage tolerance values of Ti_3SiC_2 [27,28] and Ti_3AlC_2 [21] are illustrated in figure 2.7 (bottom 3 curves) where the dependencies of post-indentation bend strengths are plotted versus Vickers indentation loads. The post-indentation flexural strengths of these ternaries are considerably less dependent on the indentation loads than typical brittle ceramics (dashed line in figure 2.7). Similar to ceramics, however, the damage tolerance of coarse-grained microstructures is superior to finer-grained samples [15].

Typically, Vickers indentations in brittle solids result in sharp cracks extending from the corners of the indents, resulting in a sharp reduction in strength. As first reported by Pampuch *et al*. [9] it is difficult to induce cracks from the corners of Vickers indentations in Ti_3SiC_2. Instead of the formation of cracks, what is observed is delaminations, kinking of individual grains and grain pull-outs in the area around the indentations [21,27,29]. In short, the main reason for damage tolerance is the ability of the MAX phases to contain and confine the extent of damage to a small area around the indentations. The atomistic reasons for this state of affairs were discussed in section 2.1.3.1.2 [15].

The high damage tolerance means that the MAX phases are tolerant to processing and service flaws that are typically detrimental to the mechanical properties of brittle solids. This, in turn, also is expected to greatly increase manufacturing yields, since the need for full density is relaxed [15].

2.1.3.1.3 Thermal Shock Resistance

Barsoum and El-Raghy [30] reported that a characteristic feature of the MAX phases is excellent thermal shock resistance. The response of Ti_3SiC_2 to thermal shock depends on grain size [28]. The post-quench flexural strengths of coarse grained samples are not dependent on quench temperature and actually get slightly stronger when quenched from 1400°C (figure 2.8). The response of fine-grained Ti_3SiC_2 samples, in contrast, is for post-quenching strengths to decrease gradually over a 500°C range (figure 2.8), instead of exhibiting a critical quenching temperature above which the strength is greatly reduced as typical for ceramics [15].

Solid solutions of $Ti_3(Si_xGe_{1-x})C_2$ are similarly not susceptible to thermal shock [15,31]. The post-quench flexural strengths of a coarse grained $Ti_3(Si_{0.5}\ Ge_{0.5})C_2$ sample were reported to be ≈20% higher than the corresponding as-sintered samples (not shown). The reasons for this

quench hardening are not entirely clear; at this time, but Barsoum and co-workers speculate that it is most probably related to the formation of smaller grains as a result of thermal residual stresses [15].

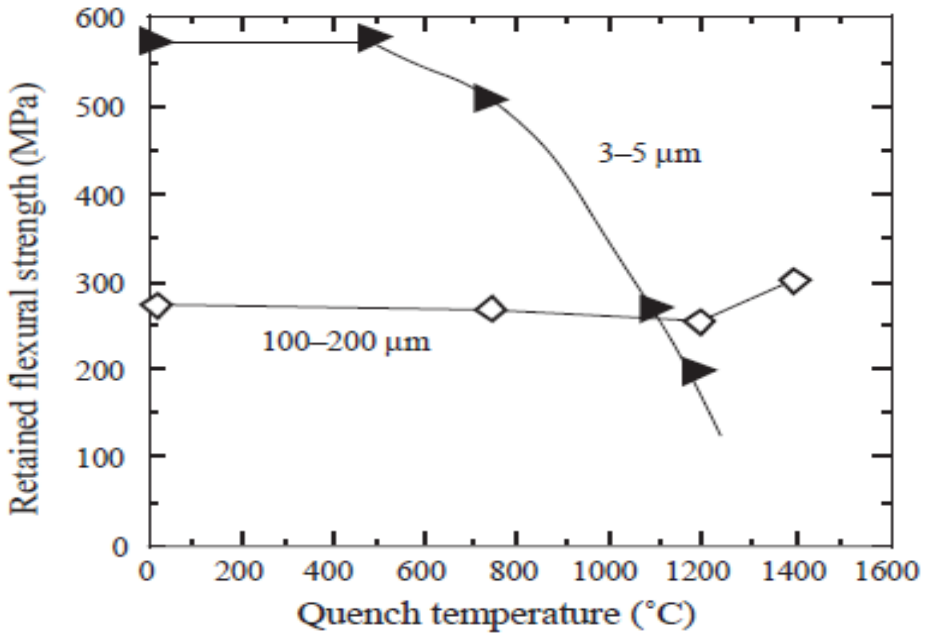

Figure 2. 8: Thermal shock response of Ti_3SiC_2 samples with two different grain sizes. (After Barsoum and Randovic [15]).

2.1.4 Elastic properties

The MAX phases are elastically quite stiff, as shown in Table 2.2. This is particularly true for the 312 and 413 group phases. Given that the densities of some of these solids are relatively low, ~4.5 g/cm^3, their specific stiffness values are considerable. For example, the specific stiffness of Ti_3SiC_2 is comparable to Si_3N_4 and roughly three times that of Ti, a metal sought after for that property. Poisson's ratios for all compounds are around 0.2, which is lower than that of Ti (0.3), and more in line with stoichiometric TiC (~0.19) [4,32].

Given the larger fraction of M-X bonds in the 312 (such as Ti_3AlC_2) and 413 (such as Ti_4AlC_3) group phases compared to the 211(such as Ti_2AlC) group phases, its not surprising that the latter are less stiff. For example, at 161 GPa, the bulk modulus of Ti_2AlN is significantly lower than the 216 GPa of Ti_4AlN_3. Increasing the atomic number of the A-group element also results in lattice-softening. For example, at 178GPa, 216GPa, and 237GPa the Young's moduli of

Zr_2SnC, Nb_2SnC, and Hf_2SnC, respectively, are all lower than any of the Al-containing ternaries (Table 2.2) [4,32].

Table 2. 2: Young's, E, shear, G, and bulk, B, moduli of selected MAX phases and near-stoichiometric TiC. Also listed are the theoretical densities and the Poisson ratio. (After Barsoum [4]).

Solid	Theo. density ($g\,cm^{-3}$)	G (GPa)	E (GPa)	ν	B^a (GPa)	B^b (GPa)
Ti_2AlC	4.1	118	277	0.19	144	186[c]
V_2AlC	4.81	116	235	0.20	152	201[c]
Cr_2AlC	5.24	102	245	0.20	138	166[c]
Nb_2AlC	6.34	117	286	0.21	165	208[c]
Ti_3SiC_2	4.52	139	339	0.2	190	206
Ti_3GeC_2	5.02	142	340	0.19	169	179
Ti_3AlC_2	4.2	124	297	0.2	165	226
Ti_4AlN_3	4.7	127	310	0.22	185	216
$TiC_{0.96}$	4.93	205	≈500	0.19	272	

In contrast to other layered solids such as graphite, boron nitride and mica, and despite their huge plastic anisotropies, the anisotropies in the elastic properties of MAX phases are quite mild. For example, c_{33} and c_{11} are almost equal for Ti_3SiC_2 and some M_2AlC phases [4,32]. Similarly, the compressibilities along the a and c-directions are comparable for most MAX phases measured to date. The Al-containing MAX phases and Ti_3SiC_2 have another useful attribute: their stiffness is not a strong function of temperature. For example, at 1000°C the shear modulus of Ti_3AlC_2 is ≈88% of its room temperature value. In that respect, their resemblance to the MX binaries is notable [4,32].

2.1.5 Thermal properties

2.1.5.1 Thermal conductivity

The thermal conductivity, κ_{th}, is given as

$$\kappa_{th} = \kappa_e + \kappa_{ph} \qquad \text{Equation 2. 1[4]}$$

where κ_e and κ_{ph} are, respectively, the electronic and phonon contributions to κ_{th}. The electron contribution to κ_{th}, κ_e, can be estimated from the Wiedemann-Franz law, that is,

$$\kappa_e = \frac{L_0 T}{\rho} \qquad \text{Equation 2. 2[4]}$$

where L_0 is the Lorenz number, 2.45 x 10^{-8} W Ω K^2. Using the electrical resistivity values (Table 2.3) and their temperature dependence (figure 2.9 (a)), κ_e may be calculated from eqn. 2.2 and, κ_{ph} from eqn. 2.1. The room temperature results for κ are listed in Table 2.4, together with the corresponding parameters for near-stoichiometric TiC_x, TiN_x, and NbC_x for comparison [32,4].

Table 2. 3: Summary of room temperature resistivity results, mobilities of electronic carriers, and their densities. (After Barsoum [4]).

		300 K mobilities ($m^2 V^{-1} s^{-1}$)		Carrier density ($10^{27} m^{-3}$)	
Compound	ρ (μΩm)	μ_n	μ_p	n	p
Ti_3SiC_2	0.22	0.005	0.006	2.5	2.5
$Ti_3Si_{0.5}Ge_{0.5}C_2$	0.27	≈0.005	≈0.005	2	2
Ti_3GeC_2	0.26	0.009	0.008	1.5	1.5
Ti_3AlC_2	0.39	0.0046–0.0042	0.0054–0.003	1.5–1.6	1.5–2
Ti_4AlN_3	2.61		0.00034		7
Ti_2AlC	0.36	0.0090	0.0082	1.0	1.0
V_2AlC	0.26	0.0046	0.0039	2.7	2.7
Cr_2AlC	0.74	0.0034	0.0036	1.2	1.2
Nb_2AlC	0.39	0.0038	0.0031	2.7	2.7
$TiC_{0.95}$	1–1.6	0.0012–0.0017		0.24–0.4	

Table 2. 4: Summary of room temperature thermal conductivity (WmK^{-1}) results for a number of ternary carbides, and near stoichiometric TiC_x and NbC_x.(After Barsoum [4]).

Compound	κ_{th}	κ_e	κ_{ph}
Ti_3SiC_2	34	33 (97%)	≈1 (3%)
	40		
Ti_3GeC_2	38	38 (100%)	
Ti_3AlC_2	40	21 (52%)	19 (42%)
$Ti_4AlN_{2.9}$	12	2.8 (23%)	9.2 (77%)
Ti_2AlC	33	20.5 (62%)	12.5 (38%)
	46	20 (43%)	26 (57%)
V_2AlC	48	29 (61%)	19 (39%)
Cr_2AlC	23	9 (39%)	14 (61%)
Nb_2AlC	29	19 (66%)	10 (34%)
	23	23 (100%)	
TiNbAlC	16.6	9.4 (56%)	7.2 (43%)
Nb_2SnC	17.5	17.5 (100%)	
Ti_2InC	≈26.5	26.5 (100%)	
TiHfInC	≈20	20 (100%)	
Hf_2InC	≈26.5	26.5 (100%)	
TiC_x	33.5	12 (36%)	21.5 (64%)
$TiC_{0.96}$	14.4	7.35 (50%)	7.05 (50%)
NbC_x	14[c]	21[a]	

[a] $L_0 < 2.45 \times 10^{-8}$ W Ω K^2.

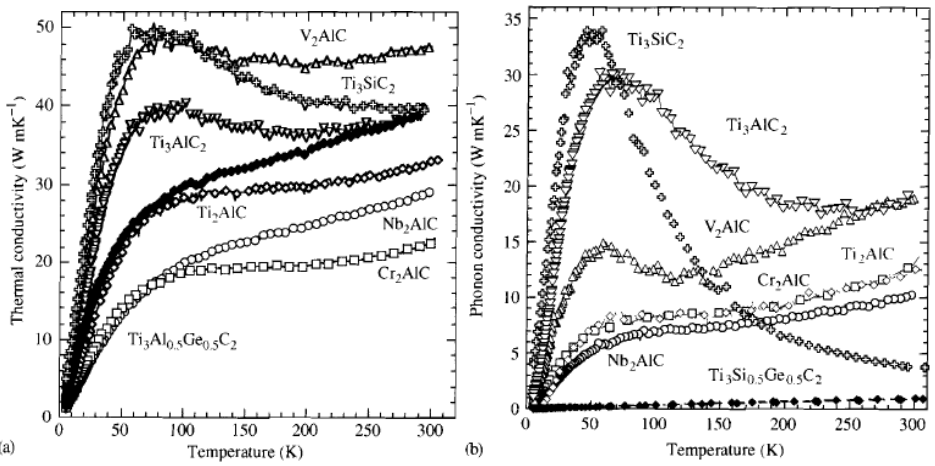

Figure 2. 9: Temperature dependence of thermal conductivities of select MAX phases: (a) total thermal conductivity and (b) phonon contribution to total thermal conductivities (After Barsoum [4]).

From these results, Barsoum *et al.* [4] concluded:

1. All MAX phases are essentially good thermal conductors because they are good electrical conductors (figure 2.9(a)).
2. For the non Al-containing MAX phases, $\kappa_{ph} \ll \kappa_e$ (Table 2.4).
3. The Al-containing MAX phases are reasonable phonon conductors (figure 2.9 (b)). The best phonon conductors at room temperature are Ti_3AlC_2 and V_2AlC; the worst is Nb_2AlC.
4. MAX-phase solid solutions totally suppress κ_{ph}. This is true of substitutions on the A-sites (figure 2.9 (b)). Along the same lines, at all temperatures, and similar to their M-X counterparts, the more κ_{ph} is suppressed, the more defective the samples. For example, in the M_2AlC phases, a correlation exists between the quality of the crystal, as measured by RRR, and κ_{ph}.
5. Most of the room temperature resistivities of the MAX phases fall in the relatively narrow range of 0.2-0.7$\mu\Omega$m (Table 2.3), except Ti_4AlN_3 which is somewhat unique in that its resistivity is more in line with semimetals than metals. The reason for this state of affairs is not clear at this time, but is most probably related to the fact that the sample tested was not stoichiometric, but closer to $Ti_4AlN_{2.9}$.
6. For the most part, $n \approx p$ and $\mu_n \approx \mu_p$ (Table 2.3). The densities of electronic carriers fall in the relatively narrow range of 1 to 3 x 10^{27}m^3. Note n and p are not related to $N(E_F)$ [4].
7. At 4 K(figure 2.10(b)), the less defective samples, as measured by the RRR, have higher mobilities. The 4 K mobilities are also inversely proportional to $N(E_F)$.

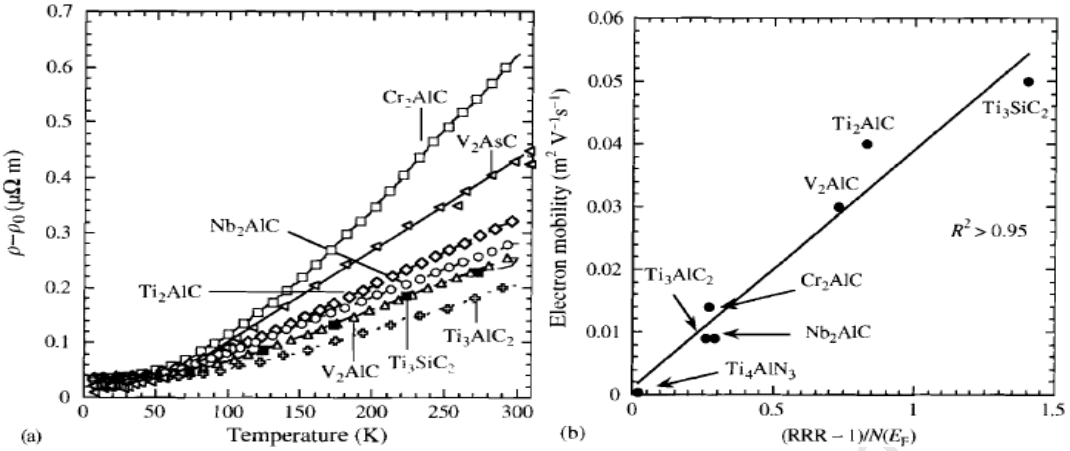

Figure 2. 10: (a) Temperature dependence of ρ - ρ_0 for select MAX phases. (b) functional dependence of electronic charge mobilities at 4 K on residual resistivity ratio (RRR) and the density of states at the Fermi level. $N(E_F)$. (After Barsoum [4]).

Table 2. 5: The Debye temperatures of selected MAX phases and near stoichiometric TiC calculated from the Poisson ratios of the respective phases (column 2) and calculated from low-temperature heat capacity measurement. The density of states at the Fermi level is also listed in the last column. (After Barsoum [4]).

Solid	Θ_D	Θ_D^T	$N(E_F)$ (1/eV unit cell)
Ti_2AlC	732	672[d]	4.9[d]
V_2AlC	696	625[d]	7.5[d]
Cr_2AlC	644	589[d]	14.5[d]
Nb_2AlC	577	NA	5.1[e]
Ti_3SiC_2	715–780	715[h]	5
Ti_3GeC_2	725	670	5.4[f]
Ti_3AlC_2	758	764[e]	3.8[f]
Ti_4AlN_3	762	779[h]	6.9[g]
$TiC_{0.96}$	940[g]	845[h]	0.1–0.5[g]

Stiff, lightweight solids with high Debye temperatures are typically good phonon conductors. Given the high stiffness of some of MAX phases, for example, Ti_3SiC_2, the fact that phonon conductivity is suppressed is somewhat surprising. As discussed in more detail by Barsoum [23], this result can be attributed to the scattering efficiency of the A-group atoms that tend to play the role of a "rattler" in these structures. Rattlers are atoms that vibrate about their equilibrium position more than other atoms [33,34]. Analysis of high-temperature (up to 1200°C) neutron diffraction spectra has shown that Si is indeed a rattler in Ti_3SiC_2 [4,23,35].

The situation for Al is more ambiguous. The results for Ti_4AlN_3, over the same temperature range, have shown that while the vibrational amplitudes of the Al atoms are greater than those of Ti or N [4,36], the differences are not as large as in the case of Si. It thus appears that Al is better bound, and thus less of a rattler, in the $M_{n+1}AlC_n$, ternaries, which partially explains why κ_{ph} is not negligible in these compounds. Probably the most convincing evidence for this hypothesis is to compare κ_{ph} for the isostructural compounds, Ti_3SiC_2 and Ti_3AlC_2 [4].

Based on RRR values that are higher for Ti_3SiC_2 than Ti_3AlC (figure 2.10(b)), Barsoum *et al.* concluded that the Ti_3SiC_2 sample tested had fewer defects than Ti_3AlC_2. At room temperature, κ_{ph} for the former is ≈5 times smaller than for the latter. Barsoum *et al.* [4] report that given the similarities of their elastic properties, and almost identical molecular weights and Debye temperatures(Table 2.5), it appears that that Si is a much more potent phonon scatterer than Al. In general, beyond Al, increasing the atomic number of the A-group element results in significant phonon scattering (e.g., compare Ti_2InC with Ti_2AlC in Table 2.4) [4].

2.1.5.2 Thermal expansion

The thermal expansion coefficients (shown as TCE in Table 2.6) of the MAX phases fall in the narrow range of 8 to 10 $x10^{-6}$ K^{-1}. A correlation has been noted between the TCEs of the ternaries and the corresponding MX binaries [4,23,37]. For example, the TCEs of the Hf-containing MAX phases are lower than those containing Ti, which in turn are lower than Cr_2AlC. For comparison, the TCEs of HfC. TiC, and Cr_3C_2 are 6.6 $x10^{-6}$ K^{-1}, 7.4 $x10^{-6}$ K^{-1}, and 10.5 $x10^{-6}$ K^{-1}, respectively [4,31]. Given their plastic anisotropy, the anisotropies in their thermal expansions [4,23] and compressibilities [4,32,38,39] are relatively mild.

Table 2. 6: Summary of dilatometric thermal expansion coefficient (x 10-6 K) values from select MAX phases shown here as TCE. (After Barsoum [4]).

Compound	TCE	Compound	TCE	Compound	TCE
Ti_2AlC	8.8	Ti_3AlN	8.2	$Ti_2AlN_{0.5}C_{0.5}$	8
Ti_3SiC_2	9.1	Ti_3AlC_2	9.0	$Ti_4AlN_{2.9}$	9.7
$Ti_3Al(C,N)_2$	7.0	$Ti_3(Si_{0.5},Ge_{0.5})C_2$	9.3	Cr_2AlC	12.0
Ti_2SnC	10	Zr_2SnC	8.3	Nb_2SnC	7.8
Hf_2SnC	8.1	Zr_2PbC	8.2	Hf_2PbC	8.3
Nb_2AlC	7.5	$(Nb_{0.5},Ti_{0.5})_2AlC$	8.5		
Ti_2InC	9.5	$(Ti_{0.5},Hf_{0.5})_2InC$	8.6	Hf_2InC	7.6

The uncertainity for most values is ±0.2.

2.1.5.3 Thermal stability

The MAX ternaries do not melt but decompose peritectically according to the following reaction:

$$M_{n+1}AX_n \rightarrow M_{n+1}X_n + A \qquad \textbf{Equation 2. 3[4]}$$

The decomposition temperatures vary over a wide range; from ≈850°C for Cr_2GaN [4,5] to above 2300°C for Ti_3SiC_2 [4,6]. The decomposition temperatures of the Sn containing ternaries range from 1200°C to 1400°C[4,37]. The decomposition temperature is a function of many variables, the most important of which is oxygen contamination and/or other impurities, which may be the reason for Oo *et al.* [40] reported decomposition temperature of 1100°C for Ti_3SiC_2 [4,41]. The decomposition temperatures and mechanisms for Ti_3SiC_2, Ti_3AlC_2 and Ti_2AlC are given more in detail in section 2.2.

2.1.5.4 Chemical Reactivity and Oxidation Resistance

The individual $M_{n+1}X_n$ layers are chemically quite stable. By comparison, the A-group layers are relatively weakly bound and are thus the most reactive species. For example, heating Ti_3SiC_2 in a C-rich atmosphere results in the loss of Si and the formation of TiC [4,42]. When the same compound is placed in molten cryolite [4,43] or molten Al [4,44] essentially the same reaction occurs: the Si escapes and TiC_x forms. In some cases, for example, Ti_2InC, vacuum at elevated temperatures is sufficient to result in the loss of the A-group element and the formation of TiC [4,45].

Given their high-temperature mechanical properties [4,15], some of the MAX phases are being considered as candidates for high-temperature applications, both structural and non-structural. Since air is to be used, however, their oxidation resistance is important. Barsoum *et al.* [46] reporting on Ti_3SiC_2, suggested that it was oxidation-resistant to temperatures as high as 1400°C. In later work however, [47] the same workers stated that that the highest temperature at which Ti_3SiC_2 can be used continuously in air is ≈900°C.

The most promising MAX phase to date, with exceptional oxidation resistance, is Ti_2AlC [4,48] . After 10 000 cycles from 1350°C to room temperature in air, a thin, adherent protective 15μm Al_2O_3 layer was found. The formation of Al_2O_3 is the key to high-temperature oxidation

protection. It is worth noting that the formation of Al_2O_3 is another example of the reactivity of the A-group layers in the $M_{n+1}X_n$ blocks. Note that Al_2O_3 forms in preference to Ti oxides, despite the fact that the Al concentration is half that of Ti, another reactive metal. Also noted is the formation of alumina layers in Ti_3AlC_2, where the Al concentration is one third that of Ti [4].

In general, the oxidation of the MAX phases occurs according to the following reaction:

$$M_{n+1}AX_n + bO_2 = (n + 1)MO_{x/n+1} + AO_y + nXO_{2b-x-y} \quad \textbf{Equation 2. 4: [4]}$$

For example, the oxidation of Ti_3SiC_2 results in the formation of an outer pure rutile (TiO_2) layer and an inner layer consisting of rutile and SiO_2 [4,53]. Even in the case of $Ti_{n+1}AlC_n$, the formation of a continuous alumina layer is a function of the purity of the samples. Impure samples or those with high contents of TiC tend to form Al_2O_3 and rutile, rather than a pure layer of Al_2O_3 [4,51,52], Ti_2InC forms TiO_2 and In_2O_3, the Sn-containing ternaries, SnO_2, etc. [4,49].

2.2 The 211 Group phases

2.2.1 Ti_2AlC

According to Qin *et al.* [52] the theoretical density of Ti_2AlC is 4.11 g/cm^3, which is lower than other ternary intermetallics such as Ti_3SiC_2, Ti_2AlN and Ti_2GeC. Due to the unique properties mentioned in section 2.1.5.4, it is expected to be useful in fields such as structural materials at high temperature, to potentially substitute for machinable ceramics, as kiln furniture, heat exchangers and so on. Qin *et al* [52] also reported that Ti_2AlC remains stable up to 55 GPa pressure at room temperature. It has also been found that the Ti_2AlC phase remains stable up to temperatures of 1300°C at ambient pressure [52].

2.2.1.1 Reaction mechanism

Zhu *et al.* [53] demonstrated the synthesis of a fully dense and single-phase Ti_2AlC bulk ceramic by hot-pressing at 1300°C. Ti (99.5 wt.%, 53μm), Al (99.5 wt.%, 74μm) and active C (98 wt.%, 74μm) powders were used as precursor for synthesizing the Ti_2AlC ceramic. The powders were weighted with wt. % of Ti : Al : C as 67.56 : 28.00 : 4.44

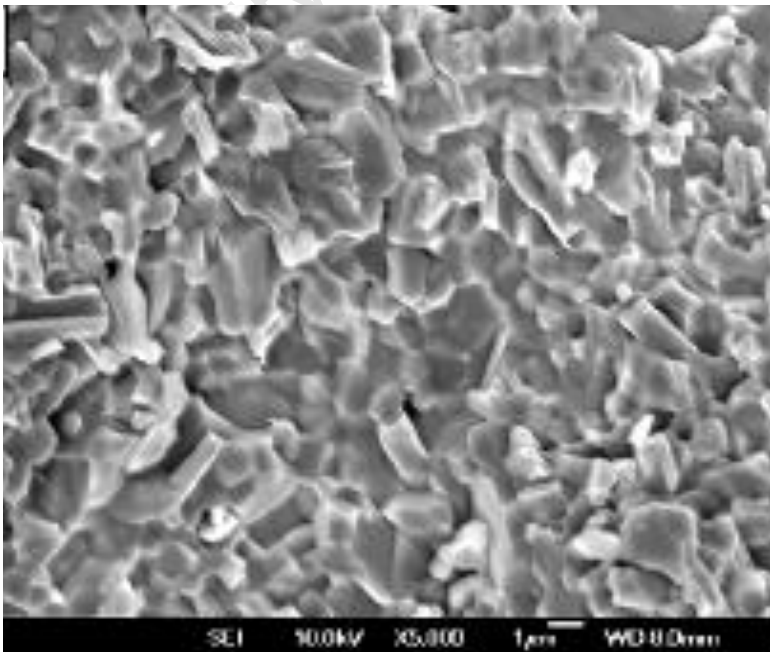

Figure 2. 11: SEM micrograph of a fracture surface of a polycrystalline Ti_2AlC. (After Zhu *et al*. [59]).

Zhu *et al.* [53] indicated that $TiAl_3$ intermetallics and TiC were formed by Ti, C and Al during high-energy milling, using a planetary ball mill at 1000rpm, at room temperature with argon as a protective gas. Hot pressing of the milled powder resulted in the transformation of the $TiAl_3$ into TiAl phase at low temperature (800°C), and formation of Ti_2AlC by reaction between the TiAl intermetallics and the TiC at high temperature (from 1200°C). Single-phase Ti_2AlC ceramics were obtained at 1300°C and further increasing the temperature to 1350°C resulted in the formation of some Ti_3AlC_2.

The synthesis of pure Ti_2AlC from powders with slightly higher Al content, as compared to the ratios in the final MAX phase, can be attributed to the volatilization of Al at the high temperatures. Due to the mechanical alloying effect, this method displayed advantages of short processing time, low applied load, high purity and fine microstructure of the Ti_2AlC ceramics (figure 2.11) [53].

2.2.1.2 Decomposition temperature studies

In order to confirm the phase segregation and check the effect of pressure on the decomposition of the Ti_2AlC phase, Qin *et al* [52] performed differential thermal analysis (DTA) measurements at *P* = 4GPa and 5GPa. They estimated the decomposition temperature at the crossing point of the linear extrapolation of the baseline and of the endothermic peak dip (figure 2.12). The decomposition temperatures detected for Ti_2AlC were 890±10°C at *P* = 5GPa and 1030±10 °C at *P* = 4GPa. Figure 2.13 shows the XRD patterns of the same samples treated at 4GPa and 5GPa. For comparison, Qin *et al* [52] inserted the XRD pattern of the starting material into the bottom of figure 2.13.

Based on the previous complete decomposition at 5 GPa and 1400°C, the breakdown reaction, under high pressure and high temperature, is: [57]

$$Ti_2AlC \rightarrow AlTi + TiC \qquad \textbf{Equation 2. 11}$$

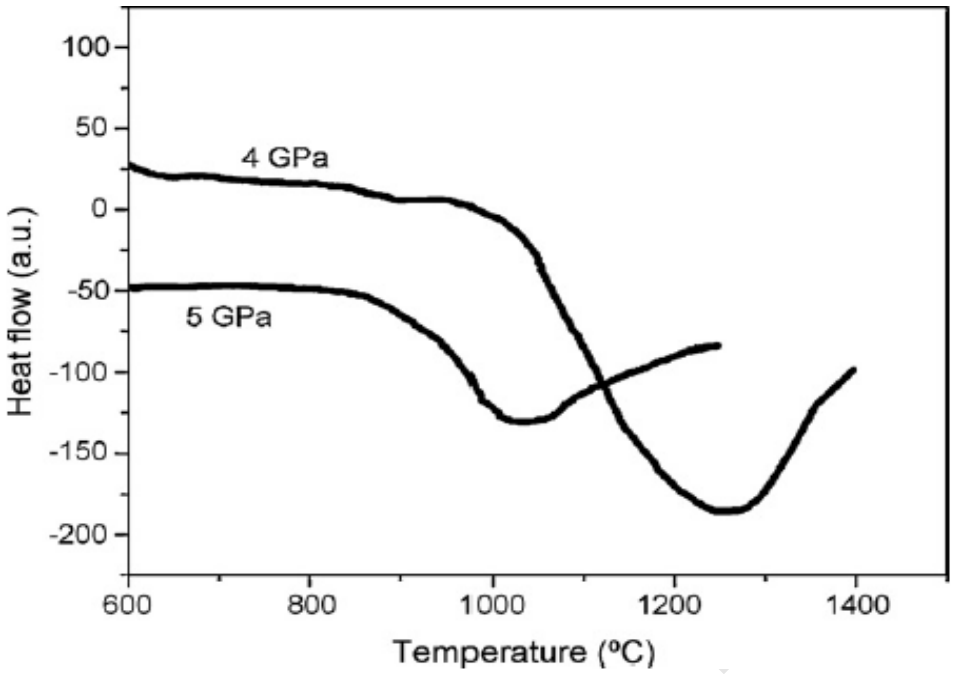

Figure 2. 12: DTA signal in the vicinity of phase segregation of Ti_2AlC at different pressures. (After Qin *et al*. [52]).

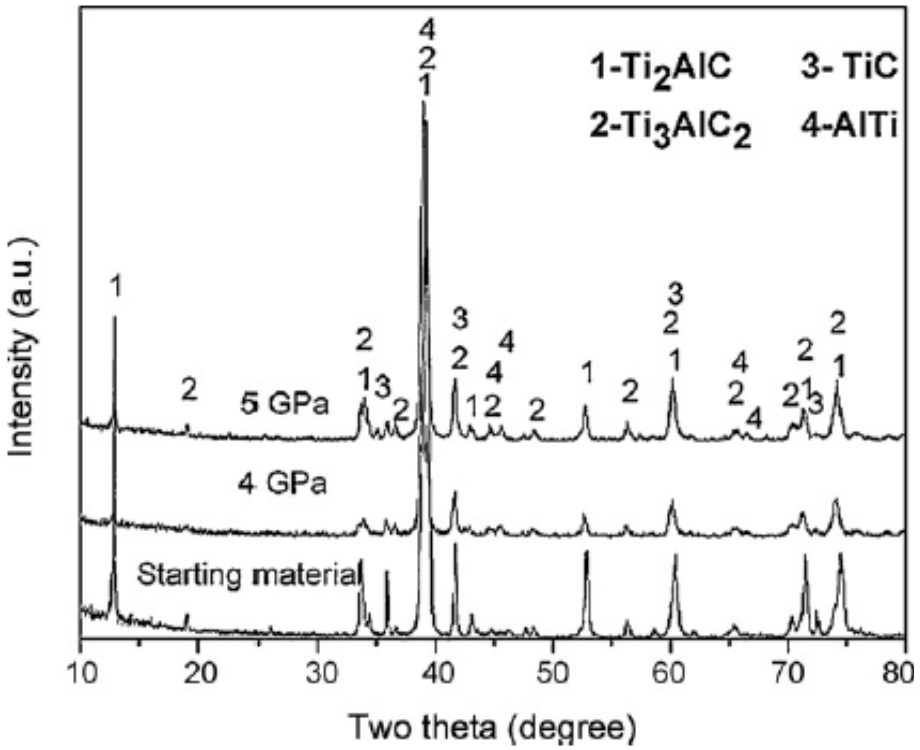

Figure 2. 13: XRD patterns of Ti_2AlC powder (starting material) before and after heating to 1400°C, at different pressures (4GPa and 5GPa) and cooled down to room temperature. (After Qin *et al.* [52]).

Qin *et al*. [52] report that the XRD patterns show the AlTi compound to have formed in the sample after heating. The high pressure–temperature (*P*–*T*) conditions were not kept long enough to decompose the sample completely in the DTA experiments, so Ti_2AlC has not decomposed completely at high pressure and high temperature. Therefore, Qin *et al*. [52] concluded that the endothermic peak appeared on the DTA curve at both pressures is the decomposition of Ti_2AlC ($Ti_2AlC \rightarrow AlTi + TiC$) under high pressure and high temperature. The decomposition temperatures determined by DTA are in good agreement with the decomposition temperature range determined by the *ex situ* XRD experiment [52].

For these samples investigated here, it seems that the decomposition temperatures for Ti_2AlC strongly depend on pressure, and the decomposition temperature of Ti_2AlC decreases against pressure. Based on these *in situ* HP-DTA results, the decomposition temperature measured at 5GPa is 140±14°C higher than at 4GPa [52]. Qin *et al* [52] thus made the following approximation $dT_d/dP = -140 \pm 14$ K/GPa.

Manoun *et al* [54] reported that Ti_2AlC could remain stable up to 55 GPa at room temperature, based on synchrotron X-ray diffraction measurements. Randovic *et al* [55] also found that the Ti_2AlC phase could remain stable up to 1300°C at ambient pressure.

2.3 The 312 group phases

2.3.1 Ti_3AlC_2

The hexagonal compound titanium aluminium carbide (Ti_3AlC_2), similar to Ti_3SiC_2, possesses an unusual combination of properties. It is relatively soft, easy to machine with conventional tools and has an excellent thermal and electrical conductivity. In addition, it has low density, good high temperature oxidation resistance and high strength at high temperatures [56].

2.3.1.1 Reaction mechanism

Peng [56] demonstrated the synthesis of a fully dense and nearly pure Ti_3AlC_2 bulk ceramic, with minor TiC as an impurity, by a solid–liquid synthesis reaction with simultaneous *in-situ* hot-pressing at 1400°C for 2 hours. Ti (99% pure, -325 mesh), Al (99% pure, -325 mesh) and graphite (99% pure, 10μm) powders were used as precursor for synthesizing the Ti_3AlC_2 ceramic. The powders were weighted with an off-stoichiometric molar composition of Ti : Al : C as 3 : 1.2 : 2. Figure 2.14 shows the fracture surface of this ceramic.

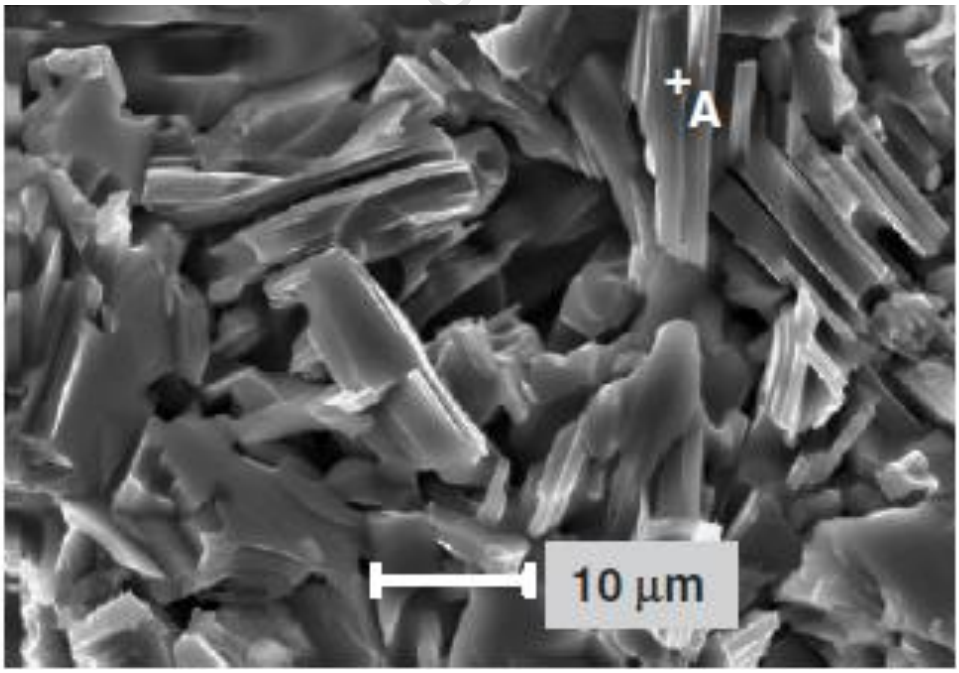

Figure 2. 14: SEM image of fracture surface of Ti_3AlC_2 sample after being sintered from the Ti-Al-C powder system. (After Peng [56]).

Peng [56] notes that hot pressing of the milled mixture of Ti, Al, and C resulted in these two reactions: C + Ti = TiC (micro-crystal) and 2TiC + Al + TiC = Ti_3AlC_2. The synthesis of nearly pure Ti_3AlC_2 from powders with slightly higher content of the Al, as compared to the ratios in the actual MAX phase, is due to the loss of part of the Al through evaporation at elevated temperature [56].

2.3.2 Ti_3SiC_2

Ti_3SiC_2 is a notable material, possessing a combination of unique properties. Its electrical and thermal conductivities are higher than those of pure Ti metal. The Ti_3SiC_2 material has good oxidation resistance and is also not susceptible to thermal shock. There are many ways to synthesize bulk Ti_3SiC_2, such as CVD [25], HIP, HP [27], etc [15,57].

2.3.2.1 Reaction mechanism

Ti_3SiC_2 has been fabricated by a hot-pressing procedure, which starts with Ti, SiC and graphite powders, at 1500°C for 2 hours [57]. A fractograph of this ceramic is shown in figure 2.15.

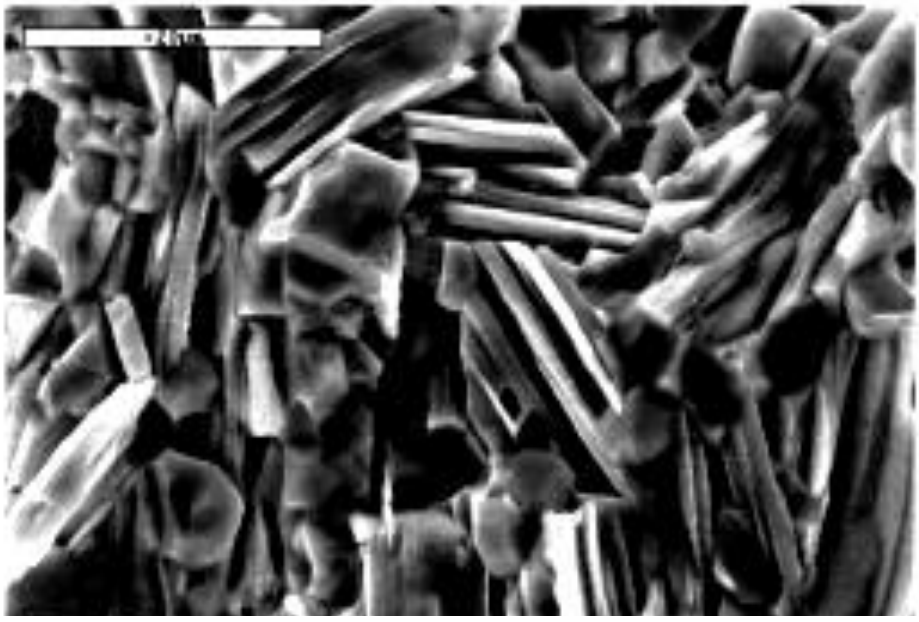

Figure 2.15: Fractograph of a Ti_3SiC_2 sample. (After Tang *et al*. [57]).

Tang *et al. [57]* describe the process as follows. When the temperature is lower than 1400°C, five principle reactions can take place: $Ti + C \rightarrow TiC$,

$5Ti + 3SiC + (x-3)C \rightarrow Ti_5Si_3C_x$,

$Ti + SiC \rightarrow TiSi + C$,

$Ti + 2SiC \rightarrow TiSi_2 + 2C$, and

$Ti + SiC \rightarrow TiC + Si$. Before the temperature reaches 1480 °C, there is no liquid phase, and only some 'secondary reaction' (i.e. not the reaction to form Ti_3SiC_2) can take place. Beyond 1480°C, because of the appearance of liquid phase, liquid-phase sintering will take place ($L + Ti_5Si_3C_x \rightarrow Ti_3SiC_2 + TiSi_2$). Ti_3SiC_2 will nucleate from the matrix $Ti_5Si_3C_x$ phase, and grow slowly to form ideal grain morphology. Because of the pressure applied to the Ti_3SiC_2 grains, their basal planes align parallel to the pressing surface and form a {0001} planar texture during hot-pressing. Because of the particular morphology of Ti_3SiC_2 grains, several Ti_3SiC_2 grains prefer to form a relative larger 'cluster' with the basal face of the hexagonal prisms parallel to each other at the grain boundaries [57].

2.3.2.2 Decomposition temperature studies

Figure 2.16 shows the temperature dependence of the relative phase abundances during the dissociation of Ti_3SiC_2 in argon using neutron diffraction[40]. From room temperature to 1000°C, the phase concentrations of Ti_3SiC_2 and TiC remain quite stable and constant. At 1100°C, Ti_3SiC_2 commences to dissociate to form TiC. Below 1200°C, the thermal-dissociation process is slow but the process becomes quite rapid from 1250°C to 1400°C. In addition, a small amount of Ti_5Si_3C is observed as a temporary phase from 20°C to 1400°C. This phase is believed to form during the initial decomposition stage of Ti_3SiC_2 and converts to the stable TiC at elevated temperature. Rutile (TiO_2) is also observed to have formed at an initial content of ~3.4 wt% at 1000°C due to partial oxidation. Its concentration increases to ~10.1 wt% at 1300°C but decreases again to 3.7 wt% at 1400°C. From this study, the sintered Ti_3SiC_2 appeared to be thermally unstable in argon from 1100°C and above [40].

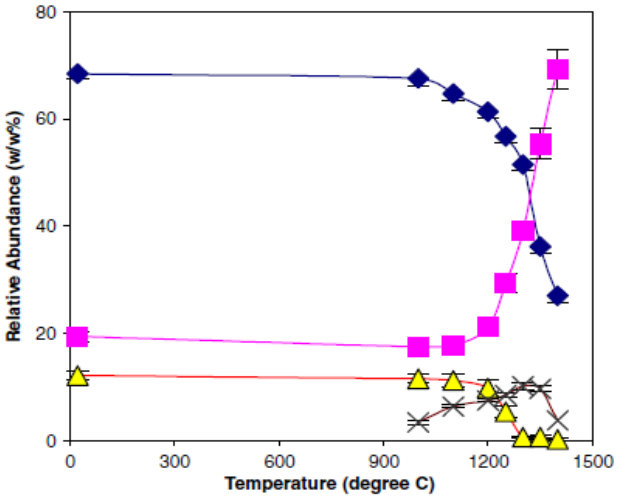

Figure 2. 16: Relative phase abundance of TiC(■), Ti_5Si_3C(▲), Ti_3SiC_2(◆) and TiO_2(×) present during the heat treatment of Ti_3SiC_2 in argon from room temperature to 1400°C. Error bars indicate two estimated standard deviations ±2σ. (After Oo *et al*. [40]).

Figure 2.17 shows the temperature dependence of the relative phase abundances during the oxidation of Ti_3SiC_2, using neutron diffraction. The intermediate phase Ti_5Si_3C slowly disappeared at around 1400°C but significant amounts of Ti_3SiC_2 and TiC remained. In the presence of a very low oxygen partial pressure, it can be suggested that the surface of Ti_3SiC_2 might undergo a high-temperature thermal dissociation process to form TiC ($Ti_3SiC_2+O_2$ + 2TiC + TiO + SiO) [40].

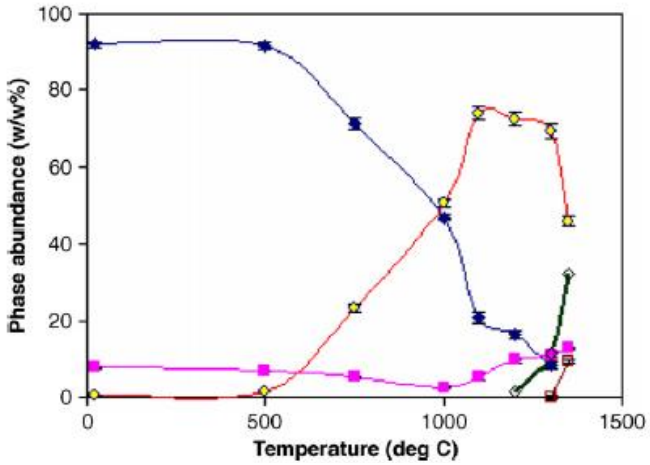

Figure 2. 17: Relative phase abundance of TIC(■), TIO_2(✧), Ti_3SiC_2(◆), SiO(□) and TiO(✧) during the oxidation of Ti_3SiC_2 in air from room temperature to 1350°C. Error bars indicate two estimated standard deviations ±2σ. (After Oo *et al*. [40]).

However, the above chemical reaction is inconsistent with the experimental observations and it does not explain the existence of Ti_5Si_3C. According to Wu *et al*. [59] the growth of Ti_3SiC_2 upon crystallites of Ti_5SiC occurs during the synthesis of Ti_3SiC_2. It follows that the reverse reaction will occur during the thermal dissociation of Ti_3SiC_2. The dissociation of Ti_3SiC_2 to Ti_5Si_3C is deemed more favourable than to TiC because silicon has a low diffusion rate in TiC-related systems. Thus the Ti_5Si_3C phase is more likely to nucleate on Ti_3SiC_2 because this mechanism would not contain any long-range diffusion of Si atoms. In view of this, Oo proposed that the pathways for the topotactic thermal dissociation of Ti_3SiC_2, in the presence of low oxygen partial pressure together with the release of reducing gas CO, to form TiC and Ti_5Si_3C are
$3Ti_3SiC_2 + 0{:}5O_2 \rightarrow 4TiC + Ti_5Si_3C + CO$ and
$Ti_5Si_3C_2 + 4CO \rightarrow 5TiC + 3SiO + 0{:}5O_2$ [40]:

The proposed volatility of CO, SiO and O_2 released is consistent with the observed results of reduced Ti_3SiC_2 mass following the heat treatment in vacuum or argon. The release of O_2 may also contribute to the partial oxidation of Ti_3SiC_2 observed in figure 2.16. Figure 2.17 shows the phase evolution of Ti_3SiC_2 during oxidation and relative abundance of oxidized phases formed at various temperatures as revealed by *in situ* neutron diffraction. Before oxidation, the phases present in sample were mainly Ti_3SiC_2 with TiC as a minor phase [40].

Oo [64] reported that at ~750°C, a portion of Ti_3SiC_2 commenced to oxidize to form rutile (TiO_2) which reached a maximum content of ~75 wt% at 1100°C before it became unstable and decomposed to form TiO. It is interesting to note that the increase in content of TiO from 1100°C to 1350°C is commensurate with a decrease in the content of TiO_2. This suggests that a zone of low oxygen partial pressure existed within the sample during oxidation which facilitated the reduction process: $2TiO_2 \rightarrow 2TiO + O_2$: [64]:

Since the process of oxidation is diffusion controlled by the entry of oxygen, a zone deficient in oxygen can exist within the bulk of sample during oxidation. As previously mentioned, the reduction reaction of TiO_2 to form TiO is highly possible when an atmosphere of low oxygen partial pressure exists. This hypothesis is further corroborated by the observation of an increasing TiC content at the same temperature range when TiO is formed (see figure 2.17) [40].

2.4 Cubic boron nitride

Cubic Boron Nitride or c-BN is one form of a synthetic material developed in the early 19th century. As boron and nitrogen are elements that are close neighbours to carbon in the periodic table, boron nitride and carbon exhibit similarities in their crystal structure. In the same way that carbon exists as graphite and diamond, boron nitride can be synthesised in hexagonal and cubic forms [58].

Cubic boron nitride is the second hardest known material, the first is diamond, and possesses many excellent physical and chemical properties (thermal stability up to 1200°C). It possesses a high resistance to chemical attack and good mechanical properties (high *H* and *E* value near diamond materials) [61]. Cubic boron nitride has a zinc blende structure with a tetrahedral symmetry (space group T_d^2) i.e. a cubic structure without an inversion center. In this diamond-like cubic structure, B-N bonds are strongly covalent, boron and nitrogen being tetrahedrally coordinated (sp^3). It consists of cubical closest-packed layers of boron and nitrogen, see figure 2.18 [2].

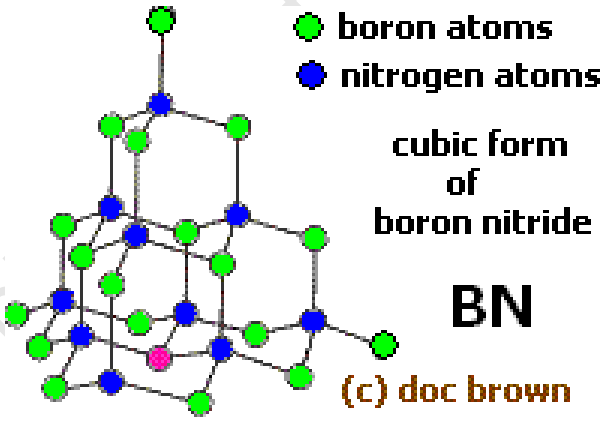

Figure 2. 18: Crystal structure of cubic boron nitride. (After Brown [59]).

2.4.1 Applications of c-BN

Super hard materials such as diamond and c-BN are widely used for grinding and tooling and as abrasives. The low chemical reactivity of c-BN with the iron group metals and its high thermal stability, particularly in oxidizing conditions, make it a better candidate for engineering materials than diamond. It is used as a powder for abrasive processes (i.e. with a wheel set-up) and as a

sintered ceramic for sawing, cutting or crushing applications. The c-BN reinforced ceramic or metal composites produced under high pressure and temperature, and the tools made from them, are inserted into high speed machining equipment for machining of hardened steels, chilled cast iron, carbides and nickel or cobalt based super-alloys [2].

2.4.1.1 Mechanical applications

Cubic boron nitride is much harder than the conventional abrasive materials such as Al_2O_3, SiC and boron carbide. Thus the grinding performance of c-BN wheels is considerably increased over the conventional SiC or Al_20_3 wheels in grinding chilled cast irons, hardened and high speed steels. Diamond tools cannot generally be used in such cases because of its chemical reactivity with ferrous metals, whereas c-BN is resistant to chemical attack in the presence of ferrous metals up to 1227-1327°C [2].

In most cases, compacted c-BN powder is cemented on tungsten carbide or ceramic substrates. The machining speed is augmented and the tool life is increased by a factor of 7-50 (in comparison with tungsten carbide tools). The high quality of the surface finish dispenses with further grinding and polishing actions in many cases [2].

2.4.1.2 Electronics

Cubic boron nitride is a III-V semiconductor compound with a wide band gap which makes it a very good insulator. Furthermore, it has an exceptionally high thermal conductivity, which allows it to be used as a heat sink for semiconductor lasers, microwave devices etc. In these applications, the surface of c-BN ceramics is coated with a group VIII metal or aluminium (or aluminium alloy) by chemical vapour deposition. It can be metallized with nickel by chemical vapour deposition or with gold or aluminium by sputtering [2].

Cubic boron nitride can be doped with Si and Be in order to get n-type or p-type semiconductors respectively. Injection luminescence in the UV was observed from a c-BN p-n junction made at a high pressure [2]. Vel [2] reports that this light emission occurs near the junction region only in certain conditions. Several methods of manufacturing p-n junctions from c-BN semiconductors prepared through a high pressure, high temperature process have been patented [2].

2.4.2 Reaction mechanism

Cubic boron nitride is synthesised in special reactors by high-pressure and high-temperature treatment. Metals of the groups IV, V, VI of the periodic table or their compounds are added as a binder phase in the sintering process. The chemical reactions between them and the boron nitride result in the formation of some new phases. In order to select the appropriate binding phase, prediction of the final products of sintering is crucial. [2].

The zinc blende lattice of BN cannot be obtained from the hexagonal cubic boron nitride (hBN) form using only compression. Because of the change of the B-N three-dimensional order, it requires both breakage and a change in the nature of the chemical bonds. This can be achieved directly using either very high pressures and temperatures or a flux precursor in order to decrease the high activation energy through a dissolution-reprecipitation process [2].

2.4.2.1 Synthesis methods

The sintering of c-BN must be performed in the thermodynamic stability region of c-BN (figure 2.19) in order to prevent reconversion into h-BN at high temperatures during the sintering process. Just like diamond, c-BN is a typically hard-to-sinter material, owing to its strong covalent bonding and its stability at high temperatures and pressures. Two processes are possible: the simultaneous sintering of c-BN during the conversion of h-BN or two-step sintering. In the latter case, the first step is the conversion from h-BN to c-BN (using a conventional high temperature, high pressure flux conversion method) followed by the separation and purification of c-BN powder and the second step involves sintering under static or dynamic high pressure conditions [2].

2.4.2.1.1 Conversion of hexagonal BN to cubic BN using the catalysed process

The following are the precursors used for the h-BN to c-BN transformation processes

1. Alkaline and alkaline earth metals, group a1 in Table 2.7
2. Alkaline and alkaline earth nitrides, group a2 in Table 2.7
3. Alkaline or alkaline earth fluoro-nitrides, group a4 in Table 2.7
4. Ammonium borate precursors, group b1 in Table 2.7

5. Inorganic fluorides, group c in Table 2.7
6. Other flux precursors, group d1 in Table 2.7

Table 2. 7: Different groups of flux precursors for the h-BN → c-BN conversion at 1747°C and a pressure of 6GPa (After Vel [2]).

Group	Material
a1	Li, Mg, Ca
a2	Li_3N, Mg_3N_2, Ca_3N_2
a3	Li_3BN_2, $Mg_3B_2N_4$, $Ca_3B_2N_4$, $Sr_3B_2N_4$, $Ba_3B_2N_4$
a4	Mg_2NF, Mg_3NF_3, Ca_2NF, $Ca_3B_2N_4 + x$LiF, $Mg_3B_2N_4 + x$LiF
b1	H_2O
b2	$(NH_2)_2CO$, NH_4NO_3, H_3BO_3, $NH_4B_5O_8$
c	NaF, $LiBF_4$, MgF_2, NH_4F, Na_2SiF_6, $(NH_4)SiF_6$
d1	Si, Si_4N_3, Si alloys
d2	AlN
d2	Sn, Sn, Pb, various alloys

2.4.2.1.2 Crystal growth under a static high pressure

This process, called the temperature difference method, involves the transport of BN with the help of a solvent from a hot zone containing h-BN to a cold region where one or more c-BN seeds are placed. The time required for crystal growth is much longer than that used for the synthesis described previously and can reach several days. The flux precursors used are generally those of group a in Table 2.7 [2].

2.4.2.1.3 Dynamic high pressure process

This technique is mainly used for compacting c-BN powders. By single shock compression, only the transformation to wurtzite boron nitride(w-BN) is observed with a large decrease in the particle size (by a factor of 10) compared with the starting material. A double-shock compression leads to an amorphous material and a small quantity of c-BN (several per cent). These c-BN particles are two-dimensional seeds. The synthesis of c-BN requires multiple-shock

compressions. If w-BN is submitted to a shock compression at a pressure above 10 GPa, c-BN can be obtained [2].

2.4.2.1.4 Gas phase deposition of cubic boron nitride

New processes of deposition of polycrystalline c-BN thin layers from the gas phase using physical methods or high temperature reactions, without a high pressure, appeared recently in the literature. The methods used consist, generally, in decompositioning by hot filament, plasma or laser a BN precursor. The reactive chemical species are deposited on a substrate. This deposit can be produced by an electrically negative bias imposed on the substrate. The nucleation is hence initiated [2].

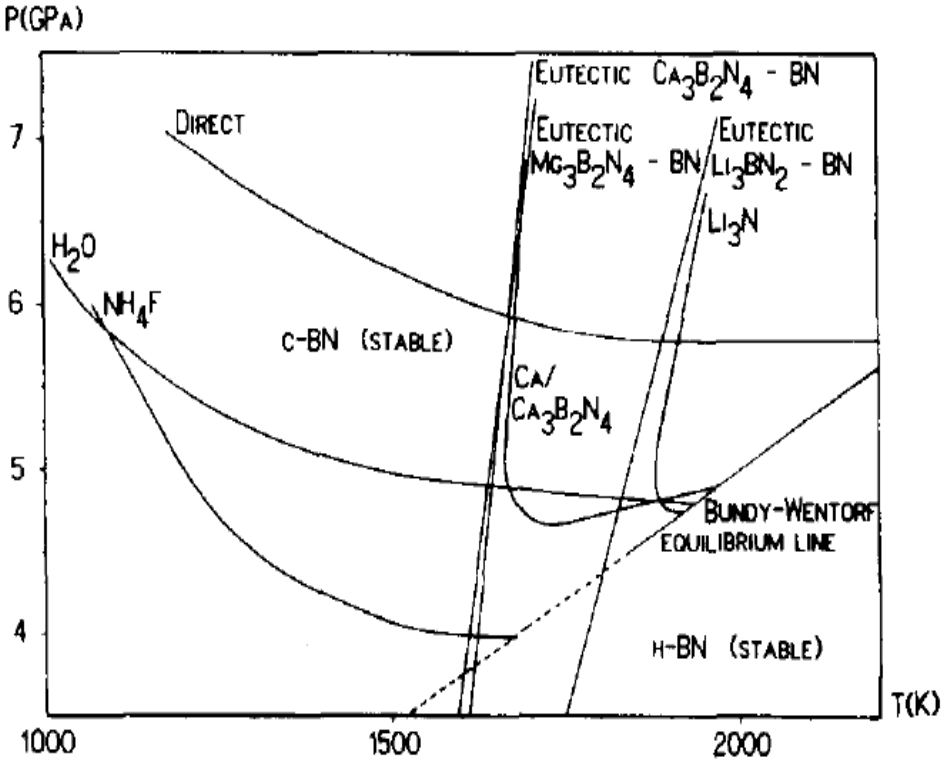

Figure 2. 19: The formation regions of c-BN using catalysed or non-catalysed processes. (After Vel [2])

2.4.3 Decomposition studies

In air, c-BN is oxygen stable to 1297-1397°C, as a B_2O_3 layer produced by slight oxidation protects against further oxidation. Vel [2] reported that there is no evidence of a conversion to h-

BN at 1397°C, however there is some conversion in nitrogen at 1525°C, 12 h and under vacuum (10^{-7} Torr) between 1547°C and 1597°C. The cubic to hexagonal transformation conditions can be calculated by equation below [2]:

P (kbar) = 0.030 T(K) - 10.3, (1 kbar=0.1 GPa) **Equation 2. 4[2]**

2.4.4 Composites of c-BN

When c-BN-Ti_3SiC_2 composites with different c-BN volume fraction (0.5 and 0.25) were sintered by hot pressing with 7GPa pressure at 1750°C the following was observed. From the microscopic observation the samples exhibit a porous, not fully dense structure. Phases such as TiB_2, SiB_4, TiC and SiC, with vacancies in TiB_2, are formed in the c-BN–Ti_3SiC_2 interface. The c-BN samples sintered with the addition of Ti_3SiC_2 exhibited Young's modulus in the range of 400–650GPa depending on the Ti_3SiC_2 contents. The highest values obtained are for samples with low content of the Ti_3SiC_2 phase. These materials exhibit hardness from 40 to 52GPa. From these measurements it was found that the composites sintered with higher Ti_3SiC_2 content show the highest hardness. The results of the hardness measurements of the samples of c-BN sintered with different amounts of Ti_3SiC_2 are presented in figure 2.20 [60].

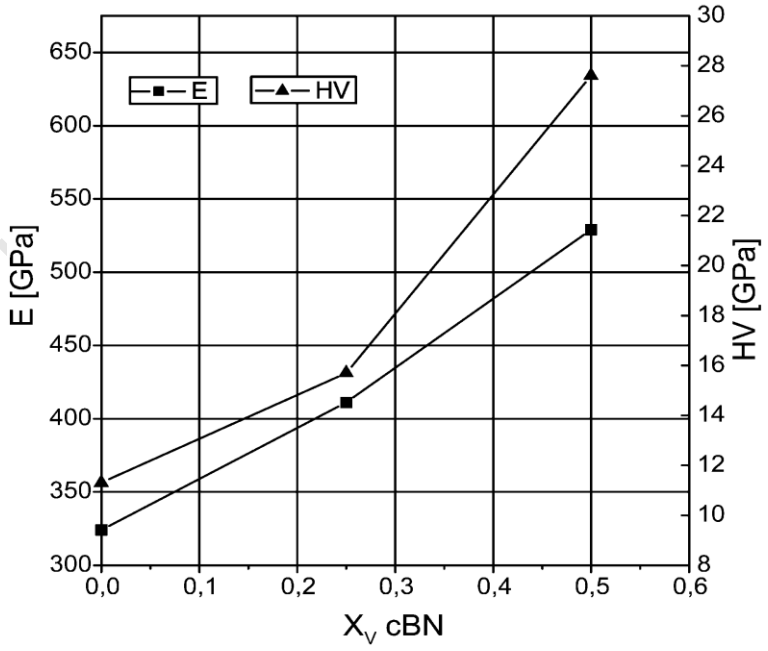

Figure 2. 20: Hardness and Young's modulus of c-BN-Ti_3SiC_2 composites with different c-BN contents (After Benko *et. al* [60]).

Rong *et al* [61] found that microhardness increased with increasing c-BN content of the specimens sintered at both 1200°C and 1400°C, and the highest microhardness of 30.7GPa was achieved for the 75 vol.% c-BN–13 vol.% TiN–12 vol.% Al composition specimen. Most of the samples sintered at 1200°C had higher microhardness than the same composition specimen sintered at 1400°C. During high-pressure sintering, reactions occurred between c-BN, TiN and Al, and new compounds, TiB_2 and AlN, were formed. TEM analysis indicated that all c-BN and TiN grains were surrounded with an AlN layer of different thickness, and small TiB_2 and AlN grains co-existed to form clusters [61].

CHAPTER THREE:
EXPERIMENTAL METHODS

3.1 Powder preparation

The powders that were used in this project were titanium, aluminium, activated carbon, titanium carbide, and silicon carbide. The properties and suppliers of these powders are shown in Table 3.1 below.

Table 3. 1: Powders used in the experiments.

Powder	Purity %	Impurities present	Supplier	Size
Ti	99	Metals basis	Alfa Aesar	-325 mesh
Al	99.97	Metals basis	Alfa Aesar	-325 mesh
C	99		ABCR	-325 mesh
SiC	99	Metals basis	Alfa Aesar	-325 mesh

3.1.1 Milling

The powders were first weighed to obtain the relevant molar ratios for the respective MAX phases, as shown in the Table below.

Table 3. 2: Mass of powders used for MAX phase synthesis.

	Ti_2AlC	Ti_3AlC_2	Ti_3SiC_2
Ti	9.576g	14.364g	14.364g
Al	2.698g	2.698g	0
C	1.200g	2.400g	1.200g
SiC	0	0	4.009g

The measured powders were then poured into zirconia milling pot already containing alumina milling balls (2mm diameter) and hexane. The closed milling pot was then placed in a planetary

ball mill which was set to mill for six hours at 300 revolutions per minute, with a ball to powder ratio of 2:1.

3.1.2 Compacting

After the milling run was complete, the milling pot was placed in a glove bag with a stainless steel spatula, a beaker containing 300ml hexane, a sample bottle, a graphite crucible, a sieve and a sieve pan. The glove bag was then sealed and air removed using a vacuum pump. The bag was filled with argon and again evacuated; this was repeated several times to eliminate as much air as possible. The contents of the milling pot were sieved to separate the milling balls from the hexane and powder so that the balls remain on the sieve and the powder and hexane go into the sieve pan.

The pot and balls on the sieve were washed into the pan using hexane, and after the powder settled in the pan then the excess hexane was poured back into the beaker to leave a paste of hexane and powders to dry. The glove bag was evacuated and backfilled with argon hourly to eliminate the hexane rich atmosphere and allow the powders in the sieve pan to dry while in the bag.

After drying, approximately 4g of powder was compacted into a graphite pot with an inner diameter of 19.50mm for hot-pressing; approximately 0.5g of powder was taken to cold mount for SEM (see section 3.2.3.3) and the remaining powder was poured into a sample bottle and stored in a vacuum desiccator for future use.

3.2 MAX phase synthesis and characterization

3.2.1 Hot pressing

The powder compacted in the graphite crucible was placed in a hot press machine (figure 3.1) for sintering. The profiles used to sinter these powders are shown in Table 3.3. After the hot-press run the crucible and sample were removed from the hot-press, then the sample removed from the crucible for further preparation.

Table 3.3: Sintering profiles for MAX phase synthesis.

	Time, min, at dwell temperature	Max temperature, °C	Pressure, MPa, at dwell temperature
Profile 1	60	1300	30
Profile 2	120	1300	30
Profile 3	60	1400	30
Profile 4	120	1400	30

For all profiles shown in Table 3.3, temperature was increased at 30 degrees per minute to the maximum temperature, and then pressure applied at that temperature for the time specified.

Figure 3.1: The hot-press used to sinter powders for MAX phase synthesis.

3.2.2 MAX phase preparation

The sintered samples were removed relatively easily from the graphite crucible before preparation as follows.

3.2.2.1 Grinding

Grinding was done by hand using a rotary grinding/polishing machine at 250rpm with water as a lubricant. The grinding discs used were diamond (200 and 800 grit) to remove the layer formed at the MAX-graphite interface, and then SiC paper (600, 800, 1200 grit), which left a much smoother finish than diamond grit. The exposed MAX phase was then polished.

3.2.2.2 Polishing

Polishing was carried out by hand at 125rpm, using 6μm, then 3μm, then 1μm diamond paste. An oxide particle suspension was used for final polishing.

3.2.3 MAX phase characterisation

3.2.3.1 Density measurements (Archimedes method)

The dry mass (m_D) for all samples was taken five times, then they were boiled in water for three hours, then the wet boiled sample was weighed again five times to get the wet mass (m_W), then finally the sample is put into the water of the density machine to measure the suspended mass (m_S) five times. The three masses were then used to calculate the absolute density of the samples, and the open porosity. The equations used are shown below:

Density of sample = $$\frac{m_d \times \rho_{H_2O}}{m_W - m_S}$$

Open porosity = $$\frac{m_W - m_D}{m_W - m_S}$$

3.2.3.2 X-ray diffraction (XRD)

Each sample was fractured into two pieces by a three-point bend jig, after notching the sample in the middle; one half of the sample was taken for SEM fracture surface analysis and the other half was used for XRD. The sample for XRD was ground flat on the cross-section fracture surface and polished using the apparatus and procedures specified above. The cross-section was then analysed using a Bruker AXS D2 PHASER desktop powder diffractometer using Cu(Kα) radiation produced at 40KV and 20mA. Diffractograms were collected over a range of 2θ between 10 to 90° using a 7 min, no spin profile.

3.2.3.3 Scanning electron microscopy (SEM)

The half of the fractured sample set aside for SEM was first ultrasonically cleaned to remove any dust particles or micro-particles which might have attached to the fracture surface. Using the Philips XL 30 ESEM-FEG (scanning electron microscope) the fracture surfaces were imaged using an accelerating voltage of 15KV. The samples were also analysed by energy dispersive spectroscopy (EDS) to determine the composition of the samples.

3.3 MAX/c-BN reaction couple synthesis and characterisation

3.3.1 Hot-pressing

A sintered MAX phase and c-BN (Amborite 90) containing approximately 90% c-BN, the remaining phases in the material were AlN and AlB_2 were used for the couples, Reaction couples samples were placed in a graphite crucible (with the lid on) then put into a hot press, as in section 3.2.1, for sintering. The profiles used for these reactions are shown in Table 3.4:

For all profiles shown in Table 3.4, temperature was increased at 50 degrees per minute to the maximum temperature, and then pressure applied at that temperature for the time specified.

Table 3. 4: Reaction conditions for reaction couple synthesis.

	Time, min, at dwell temperature	Max temperature, °C	Pressure, MPa, at dwell temperature
Ti_2AlC	30	1500	0
	30	1500	10
Ti_3SiC_2	30	1500	0
	30	1400	10

3.3.2 MAX/c-BN reaction couple preparation

3.3.2.1 Cutting

The samples were cut using a Struers Secotom-10 precision cutting machine with a diamond cutting disc, across the middle of the reaction couple to expose the two samples and their reaction site for analysis. In the case of Ti_3SiC_2/c-BN at 1500°C where there was no reaction, the two were not cut but they were taken for XRD to find out whether there was any transformation and if so, what were the products.

3.3.2.2 Grinding

Grinding was done using the grinding/polishing machine under the conditions specified in section 3.2.2.1, but using only the 800 and 1200 diamond grinding discs. The exposed site was then polished using the equipment and conditions specified in section 3.2.2.2.

3.3.3 MAX/c-BN reaction couple characterisation

Characterisation of the prepared site was done by XRD and SEM, using the conditions described in sections 3.2.3.2 and 3.2.3.3. In addition using EDS a trace of the elements from the surface of the MAX phase across the reaction site to the surface of the c-BN sample was performed to analyse the degree of reactivity between the two samples.

3.4 MAX/c-BN composites synthesis and characterisation

For MAX/c-BN composites synthesis, a sintered MAX phase ceramic (Ti_3SiC_2 or Ti_2AlC) was crushed to less than 20μm powder by milling with 2mm alumina balls in hexane using an Attriter mill at 250 rpm. The MAX powder was then mixed with 8μm c-BN powder in the ratio of 80:20 (vol%) using a tubular mixer at 67rpm for four hours

3.4.1 Spark plasma sintering (SPS)

The MAX/c-BN powder mixture was poured into a graphite pot, then sintered in a spark plasma sintering apparatus (SPS), shown in figure 3.2. Sintering conditions were 1400°C, 20MPa for the Ti_3SiC_2; and 1500°C, 20MPa for the Ti_2AlC.

Figure 3.2: The SPS used to sinter cBN/MAX powders to synthesise the composite material.

3.4.2 MAX phase/c-BN composites preparation and characterisation

The sintered samples were fractured into two pieces by a three-point bend jig, after notching the sample in the middle. The first piece was used for SEM imaging of the fracture surface from the edge of the sample, to the core, to determine c-BN dispersion in the MAX phase. The second sample's exposed surface was ground and polished as described in section 3.3.2.2 above, for SEM and EDS analysis.

CHAPTER FOUR:

RESULTS

4.1 Powder characterisation

After milling mixtures of elemental powders, the powder mixtures were analysed by SEM to characterise the degree of dispersion of the different powders and their morphology. EDS was done on the powders to determine the nature of the particles or phases present after milling.

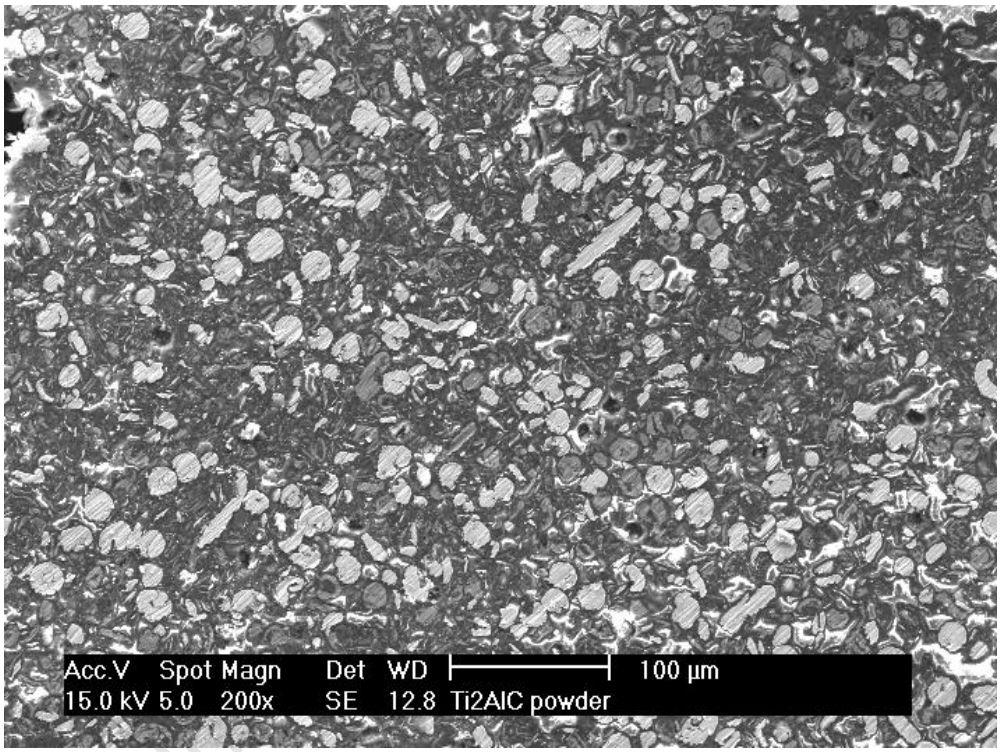

Figure 4. 1: SEM secondary electron (SE) image of mixed Ti, Al and C powders used to synthesise Ti_2AlC.

Figure 4.1 shows an image of the mixed powders used to produce the Ti_2AlC phase. The particles in light contrast (white) are round or elongated; darker gray elongated particles and a black phase are also visible.

Figure 4.2 shows the EDS analysis of the same powder, the darker grey particles are Al and the black particles are C with some oxygen content. The white particles are Ti.

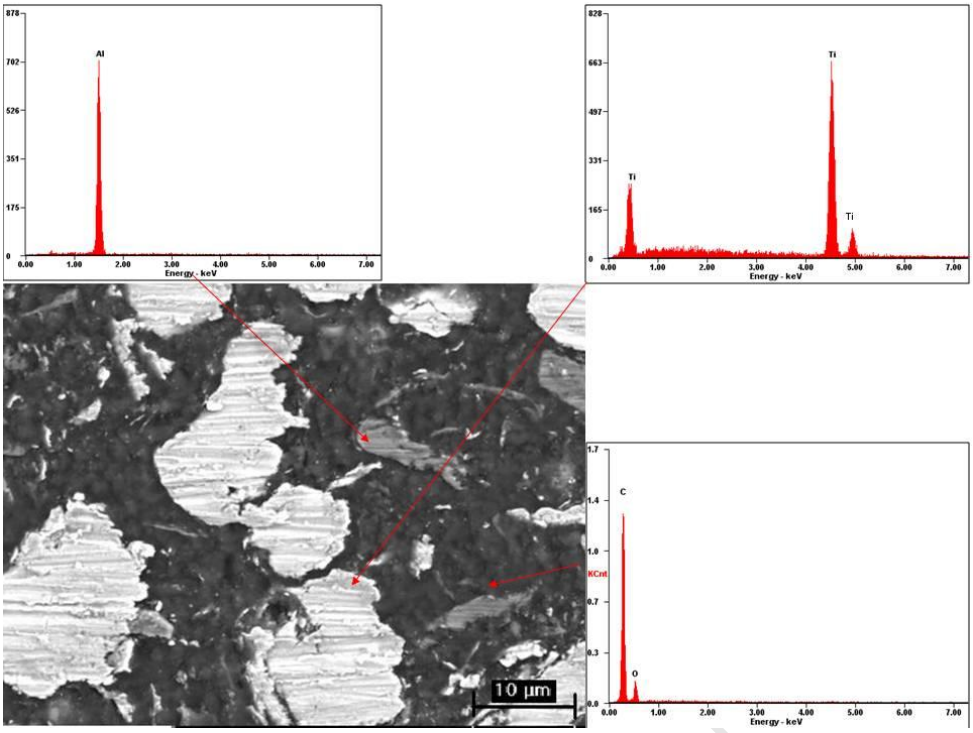

Figure 4. 2: Secondary electron (SE) image of powders in figure 4.1, showing EDS analysis of those particles.

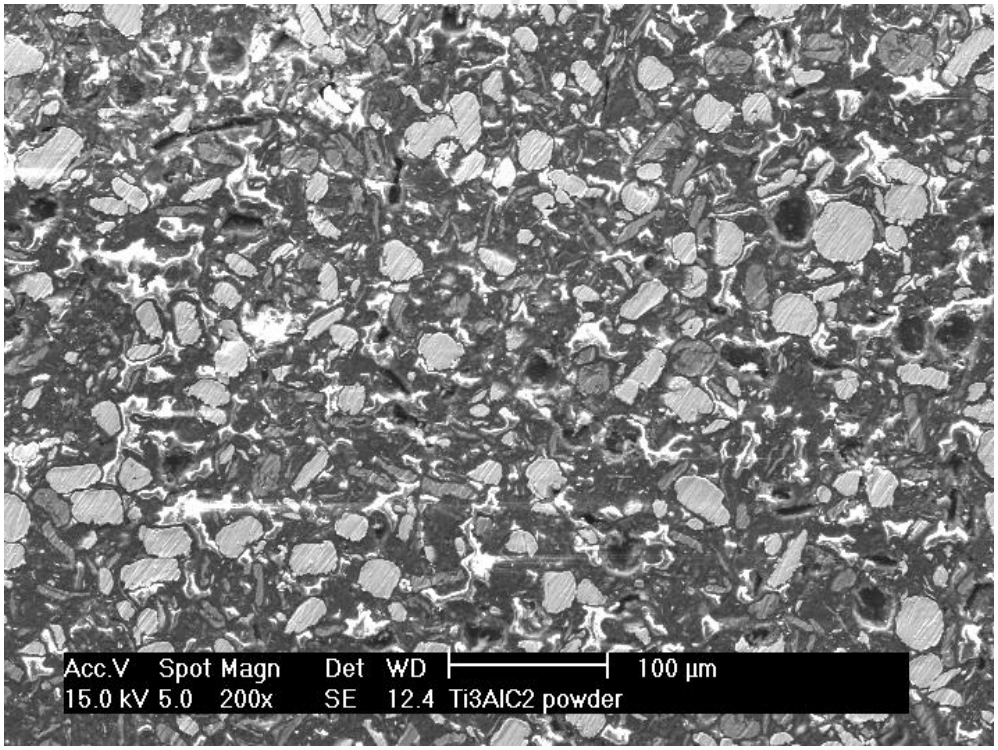

Figure 4. 3: SEM (SE) image of mixed Ti, Al and C powders used to synthesise Ti_3AlC_2.

Figure 4.3 shows an image of the mixed powders Ti, Al and C used to produce the Ti_3AlC_2 phase. As in figure 4.1, round and elongated white particles are observed, together with darker grey elongated particles and a black phase.

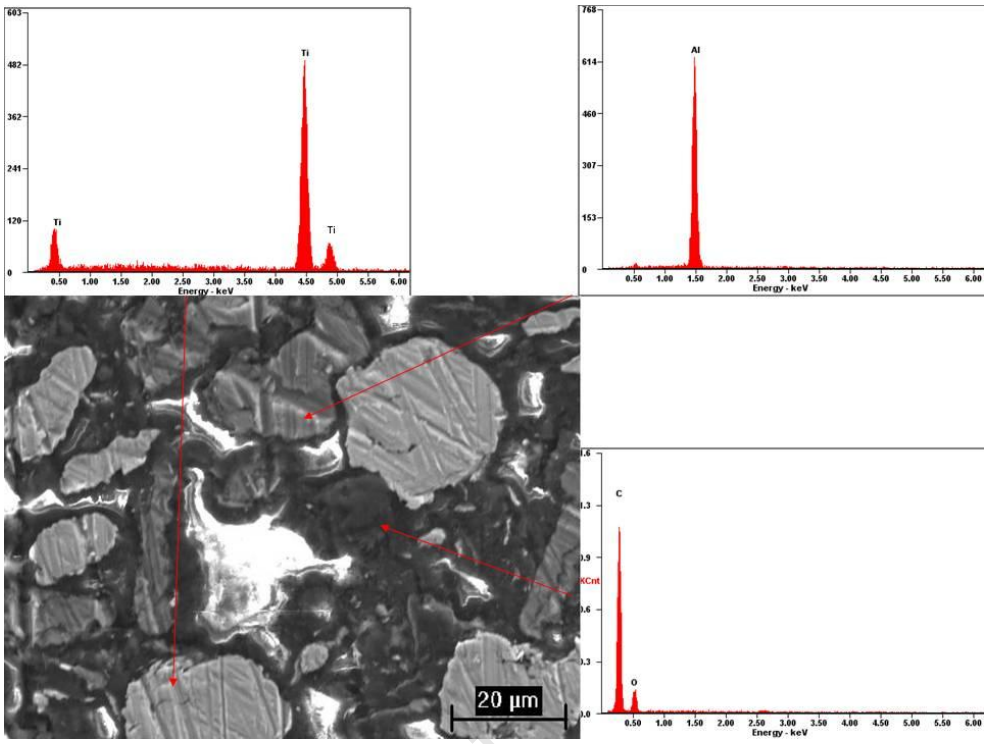

Figure 4. 4: Secondary electron (SE) image of powders in figure 4.3, showing EDS analysis of those particles.

Figure 4.4 shows the EDS analysis of the same powder: The white particles are Ti, the darker grey particles are Al and the black phase is C with some oxygen content.

Figure 4.5 shows an image of the mixed powders used to produce the Ti_3SiC_2 phase. It shows grey round particles, grey elongated particles and a black phase surrounding the other particles.

Figure 4.6 shows the EDS analysis of the same powder: The light grey particles are Ti, with a region of carbon includes in the analysis of the Ti particle the black particles are a mixture of SiC and C; the white region is the result of charging of the resin surrounding the powders.

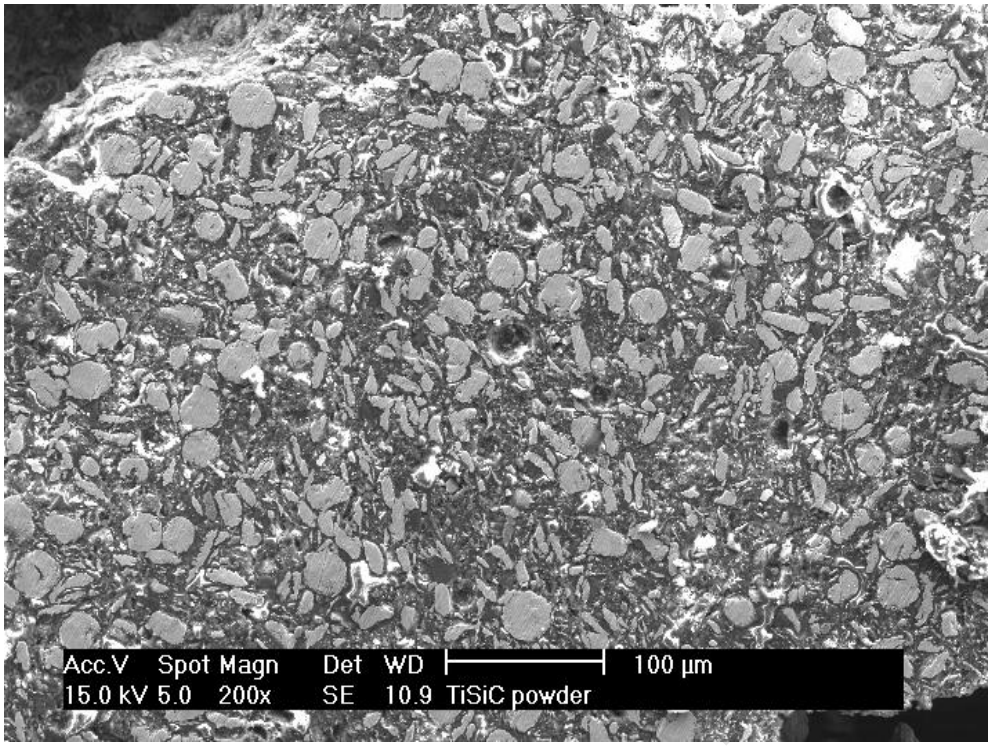

Figure 4. 5: SEM (SE) image of mixed Ti, SiC and C powders used to synthesise Ti_3SiC_2.

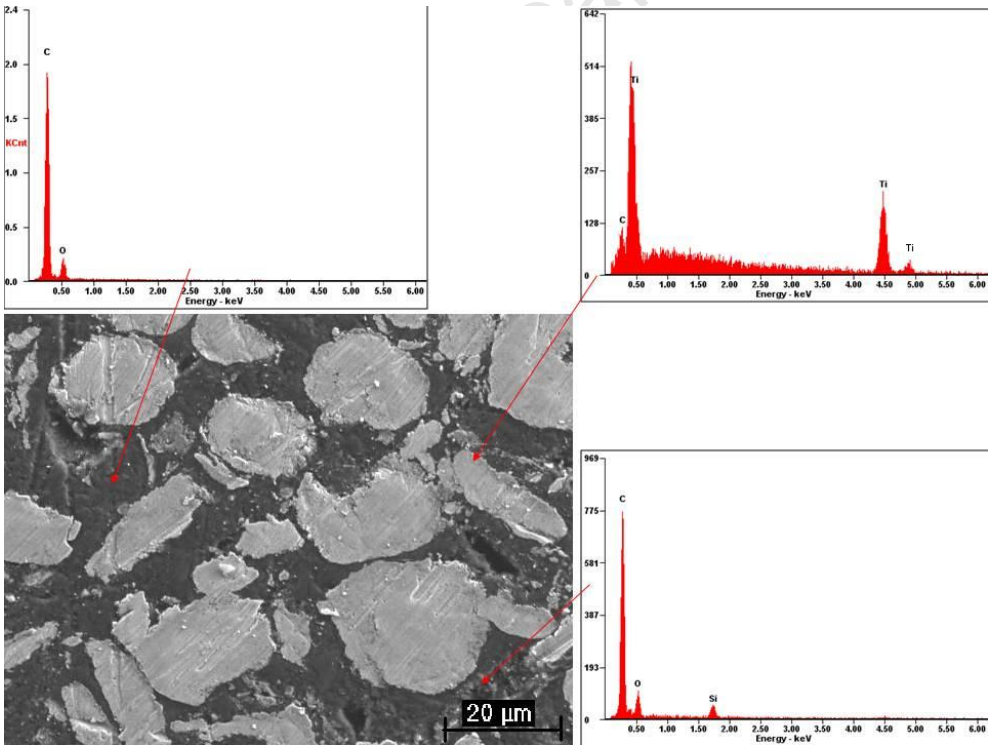

Figure 4. 6: Secondary electron (SE) image of powders in figure 4.5, showing EDS analysis of those particles.

4.2 Characterisation of synthesised MAX phases

The powder mixtures described in section 4.1 were hot-pressed according to section 3.2 to form sintered compacts of MAX phases.

4.2.1 Density

Table 4.1 shows results of density and open porosity measurements for different MAX phases, sintered at different time-temperature profiles. All samples were sintered at 30MPa.

Table 4. 1: Density and open porosity of sintered samples.

Sintering conditions		Ti_2AlC (Th. 4.11 g/cm^3)		Ti_3AlC_2 (Th. 4.50 g/cm^3)		Ti_3SiC_2 (Th. 4.52 g/cm^3)	
Temperature (°C)	**Time in minutes**	**Density (g/cm^3)**	**% Open porosity**	**Density (g/cm^3)**	**% Open porosity**	**Density (g/cm^3)**	**% Open porosity**
1300	**60**	3.96	0.42	3.95	0.18	3.68	2.18
1300	**120**	4.03	0.11	4.00	0.39	3.89	1.64
1400	**60**	4.04	0.67	4.01	0.23	4.42	0.17
1400	**120**	4.08	1.10	4.04	1.09	4.44	0.19

For the Ti_2AlC, the density is above 95% of the theoretical density for all samples; the lowest percentage being 96.36% for the sample synthesised at 1300°C\60 min and the highest being 99.2% for the sample synthesised at 1400°C/120minutes. Open porosity is 1.1% or less for the samples recorded in Table 4.1.

For the Ti_3AlC_2, the density is above 85% of the theoretical density for all samples; the lowest percentage being 87.8% for the sample synthesised at 1300°C\60 min and the highest being 89.8% for the sample synthesised at 1400°C/120minutes. Open porosity is 1.1% or less for the samples recorded in Table 4.1.

For the Ti_3SiC_2 the density is above 80% of the theoretical density for all samples; the lowest percentage being 81.3 % for the sample synthesised at 1300°C\60 min and the highest being 98.2% for the sample synthesised at 1400°C/120minutes. Open porosity is 2.2% or less for the samples recorded in Table 4.1.

There is no statistical significance in the difference of the densities and open porosities of all samples; therefore there is no clear trend to be observed. The theoretical densities are

calculated for one phase materials. As the following section will show, the materials are not completely reacted; therefore the relative densities have to be used with caution.

4.2.2 XRD, SEM and EDS results

The materials prepared by the four temperature/time sintering profiles were evaluated by XRD analysis of samples prepared by those profiles. Identification of the sample containing the largest amount of MAX phase was carried out by XRD analysis. An evaluation of the relative amount of MAX phase was obtained by selecting the peak of each relevant phase, which is not shared with any other phase, taking its count value (y-axis on the Diffractogram) and dividing it by the sum of all the count values of the present phases obtained in the same way. This was done only to evaluate whether there was a decrease or an increase in the desired MAX phase as we increased time and temperature. It is not meant as a quantitative or qualitative evaluation of the present phases. The selected phase peaks are specified in sections 4.2.1.1, 4.2.1.2 and 4.2.1.3. The selected sample was fractured, and SEM of the fracture surfaces was taken to analyse the layered structure.

4.2.1.1 Ti_2AlC

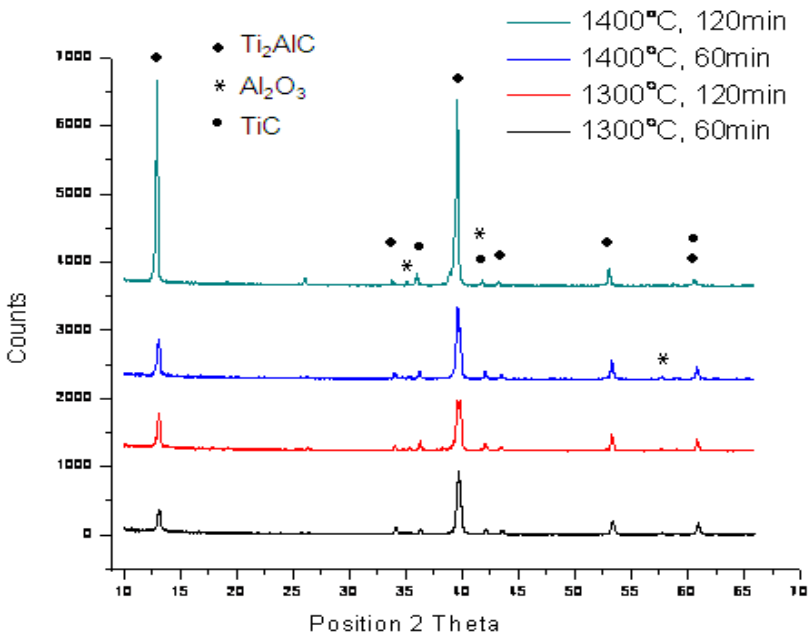

Figure 4. 7: Diffractogram of Ti_2AlC synthesised from Ti, Al and C powders at different time and temperature profiles.

Figure 4.7 shows the XRD results obtained from Ti_2AlC samples synthesised at different temperature and time profiles. In addition to the Ti_2AlC phase, a secondary TiC phase is also present in all samples; some Al_2O_3 contamination is also observed. The peaks selected for the analysis in figure 4.8 below are Ti_2AlC (~13 (2θ)), TiC (~37 (2θ)), and Al_2O_3 (~35 (2θ)) for all spectra.

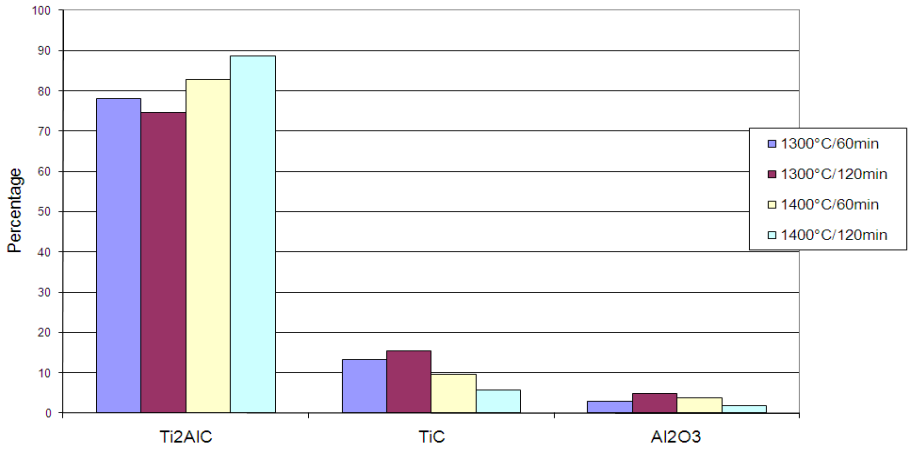

Figure 4. 8: A summary of the products formed at different time and temperature profile.

Figure 4.8 shows that the XRD peak intensity of the Ti_2AlC phase increases with increasing temperature and that of TiC decreases with increasing temperature. The optimum sintering conditions for this sample are therefore 1400°C and 120 minutes.

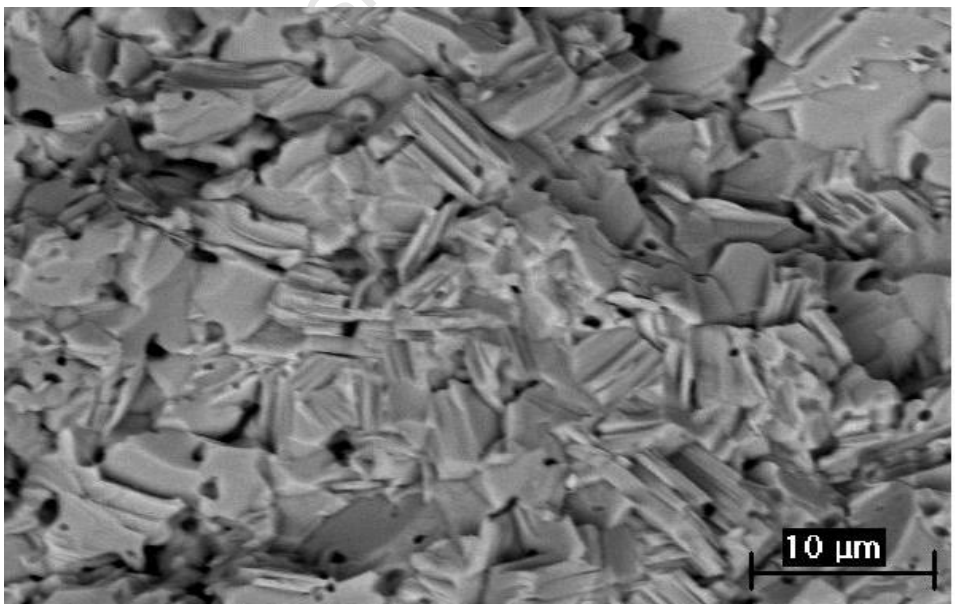

Figure 4. 9: Fracture surface: SEM back scattered electron (BSE) image using cathodoluminescence (CL),. image of Ti_2AlC synthesised at 1400°C, 120 minutes.

Figure 4.9 shows the fracture surface Ti_2AlC sample sintered at 1400°C for 120 minutes under 30MPa pressure giving the highest amount of the MAX phase. The image reveals some platelet structures.

4.2.1.2 Ti_3AlC_2

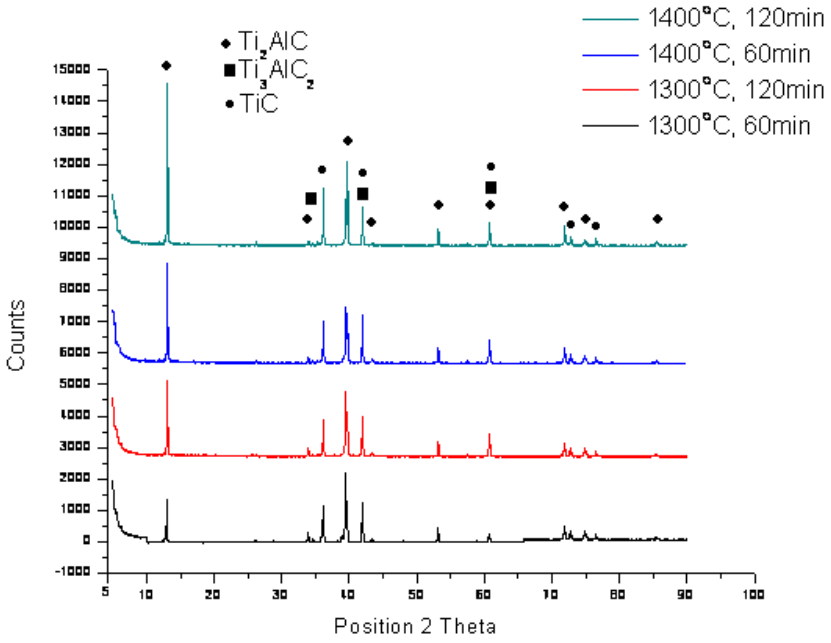

Figure 4. 10: Diffractogram of Ti_3AlC_2 synthesised from Ti, Al and C powders at different time and temperature profiles.

Figure 4.10 shows the XRD results obtained from Ti_3AlC_2 samples synthesised at different temperature and time profiles. In addition to the Ti_3AlC_2 phase, Ti_2AlC is also present in much larger quantities than the desired Ti_3AlC_2 phase. A secondary TiC phase is also present in all samples and some C contamination is observed. The quantitative analysis for this sample cannot be done since the Ti_3AlC_2 peaks are shared with other phases. So for the fracture surface analysis the sample at 1400°C, 120 minutes will be analysed just as the samples before.

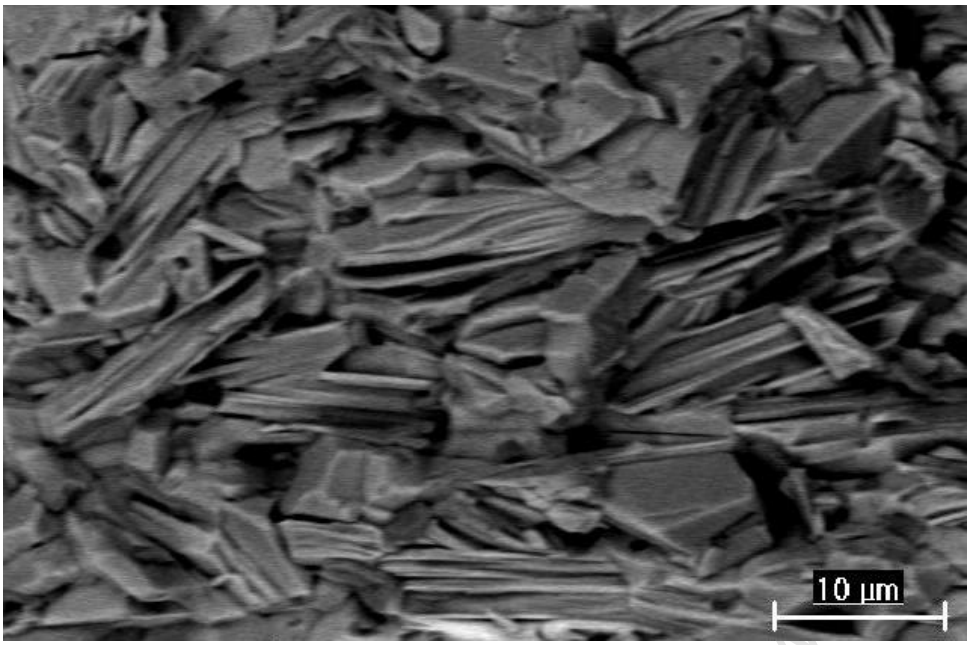

Figure 4. 11: Fracture surface: SEM (BSE) CL image of Ti_3SiC_2 synthesised at 1400°C, 120 minutes.

Figure 4.11 shows the fracture surface of a Ti_3AlC_2 sample, which is mainly Ti_2AlC, sintered at 1400°C for 120 minutes under 30 MPa pressure. The image reveals mainly layered structures, and some pores along the sample.

4.2.3.3 Ti_3SiC_2

Figure 4.12 shows the XRD results obtained from Ti_3SiC_2 samples synthesised at different temperature and time profiles. In addition to the Ti_3SiC_2 phase, secondary TiC and SiC phases are also present in all samples. The samples sintered at 1300°C have an additional Ti_5Si_3 phase, also some SiC was observed. The peaks selected for the analysis in figure 4.8 below are Ti_5Si_3 (~73 (2θ)), TiC (~37 (2θ)), SiC (~25 (2θ)), and Ti_3SiC_2 (~10 (2θ)) for all spectra.

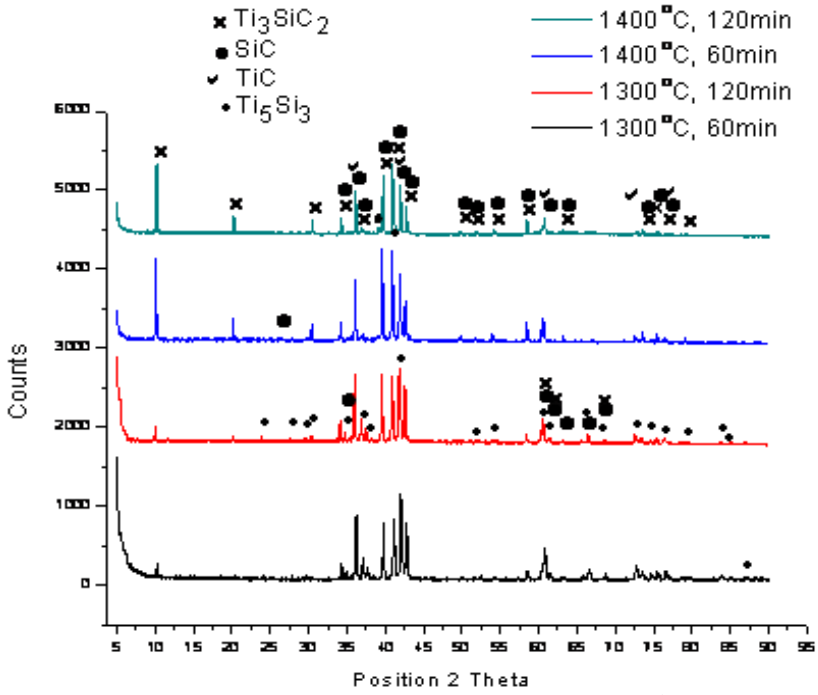

Figure 4. 12: Diffractogram of the Ti_3SiC_2 synthesised from Ti, SiC and C powders at different time and temperature profiles.

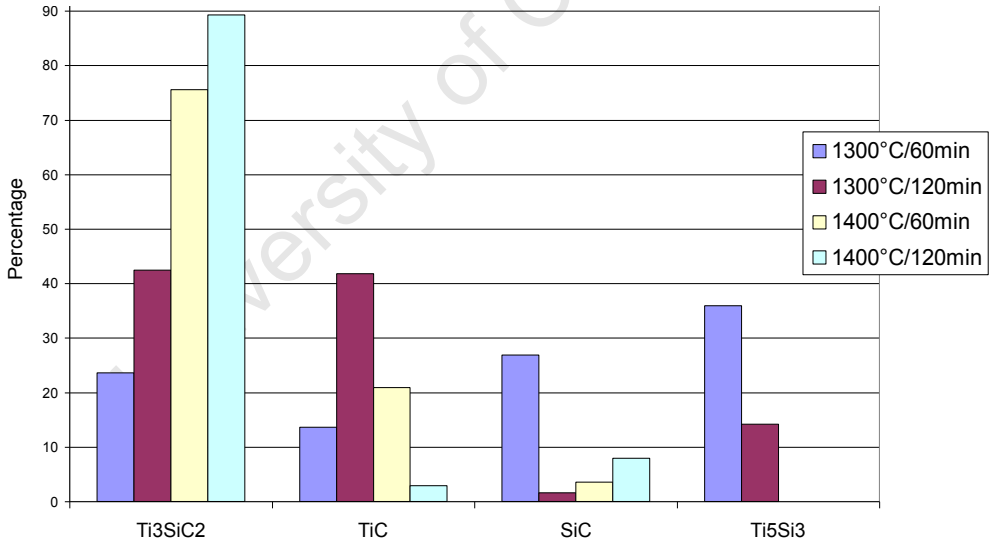

Figure 4. 13: Summary of the products formed during the making of Ti_3SiC_2 at different time and temperature profiles.

Figure 4.13 shows that the Ti_3SiC_2 phase increases with increasing temperature and time, Ti_5Si_3 decreases with increasing time, and completely disappears with an increase in temperature to 1400°C. At 1300°C, 120 minutes the highest TiC content was observed.

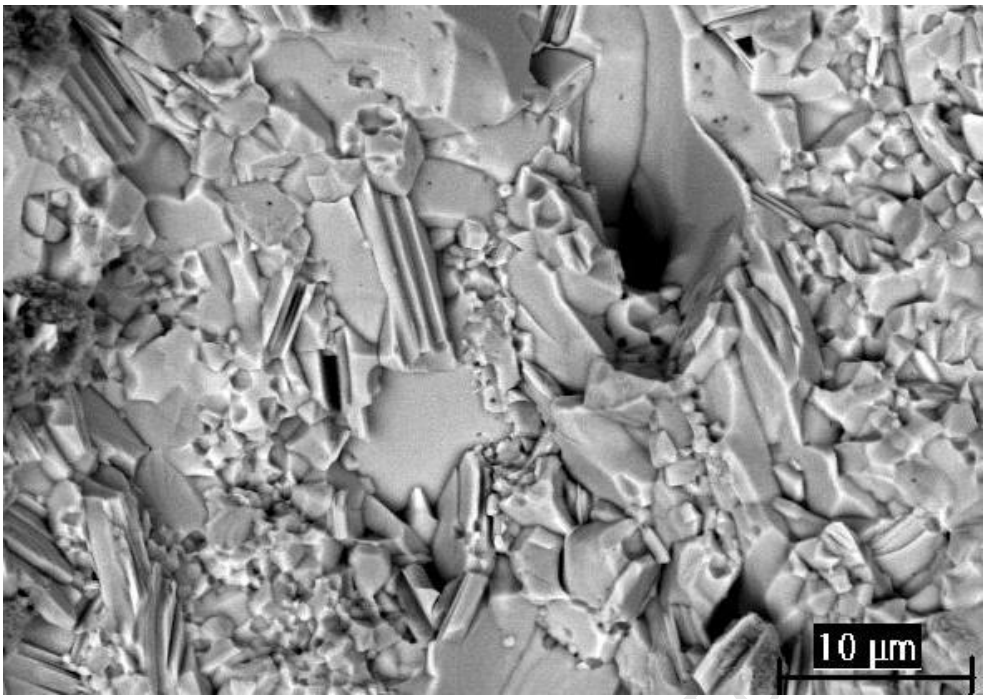

Figure 4. 14: Fracture surface: SEM (BSE) CL image of Ti_3SiC_2 synthesised at 1400°C, 120 minutes.

Figure 4.14 shows the fracture surface of a Ti_3SiC_2 sample sintered at 1400°C for 120 minutes under 30MPa pressure. The image reveals some layered structures, some flat structures and some randomly orientated structures.

4.3 Characterisation of reaction couples

The interfacial region of MAX phase/c-BN couples were characterised after sintering at two different temperatures and pressures. The c-BN sample used for all the below mentioned reactions in this section are amborite-90, which contains some Al. Amborite-90 contains 90% c-BN and Al which is used to densify the c-BN grains by getting among the grains and 'holding' them together.

4.3.1 Ti_2AlC/c-BN reaction couples

4.3.1.1 Reaction with ambient pressure at 1500°C for 30 minutes

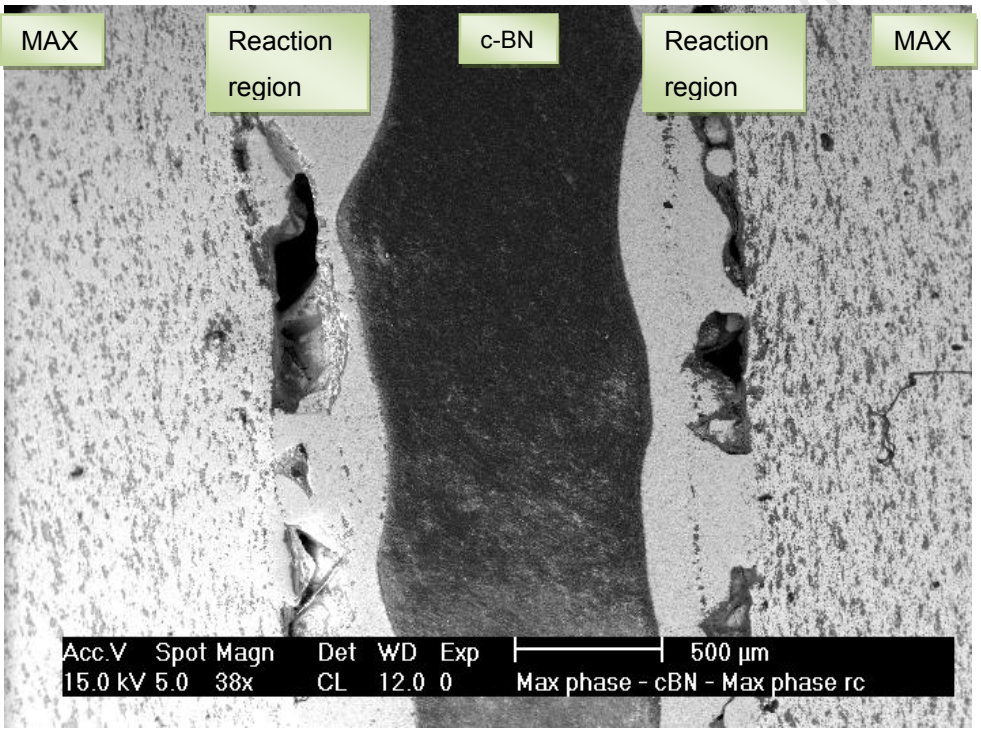

Figure 4. 15: Back scattered (CL) image of the reaction couple Ti_2AlC/c-BN reacted at 1500°C, 30 minutes and ambient pressure.

Figure 4.15 shows an image of the reaction couple reacted at 1500°C for 30 minutes at ambient pressure: the image shows a reaction zone with a thickness of approximately 400µm. Between the MAX phase and the reaction zone there are pores, this is not seen on areas between the c-BN sample and the reaction area. Figure 4.16 showing that the c-BN on the surface interacted with the MAX phase at this temperature.

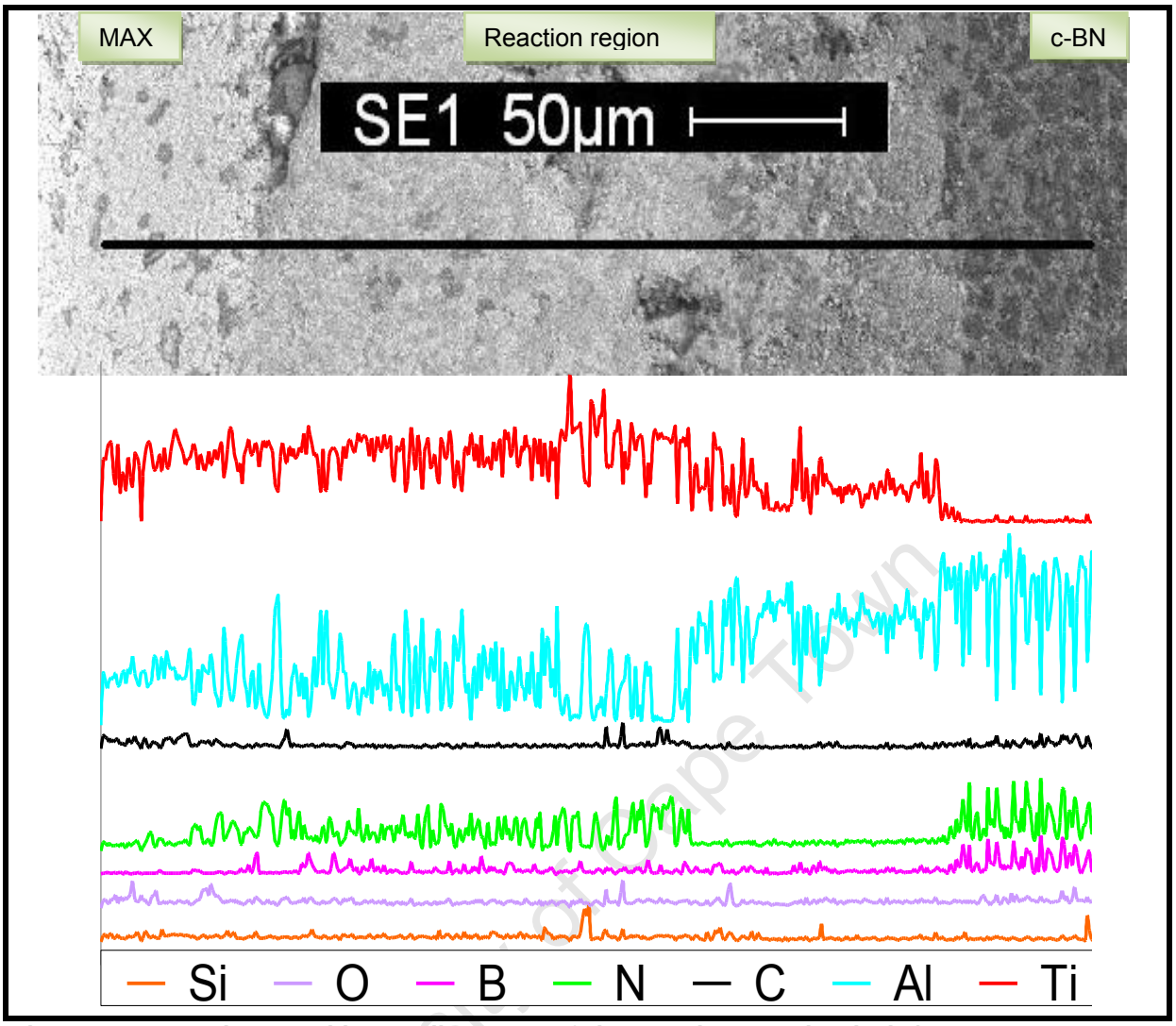

Figure 4. 16: SE image with EDS line scan of the reaction couple Ti_2AlC/c-BN at 1500°C, 30 minute and ambient pressure.

Figure 4.16 shows an EDS line scan of the reaction couple Ti_2AlC/c-BN. Some Si and oxide contaminations are observed across the couple. Boron and nitrogen are seen to be present in all regions, but markedly low across the MAX phase and in the reaction region adjacent to c-BN. Aluminium and carbon concentrations are high across the whole couple, but markedly higher in the c-BN than the other regions. Ti is present across the MAX phase and the reaction region; but minimal across the c-BN.

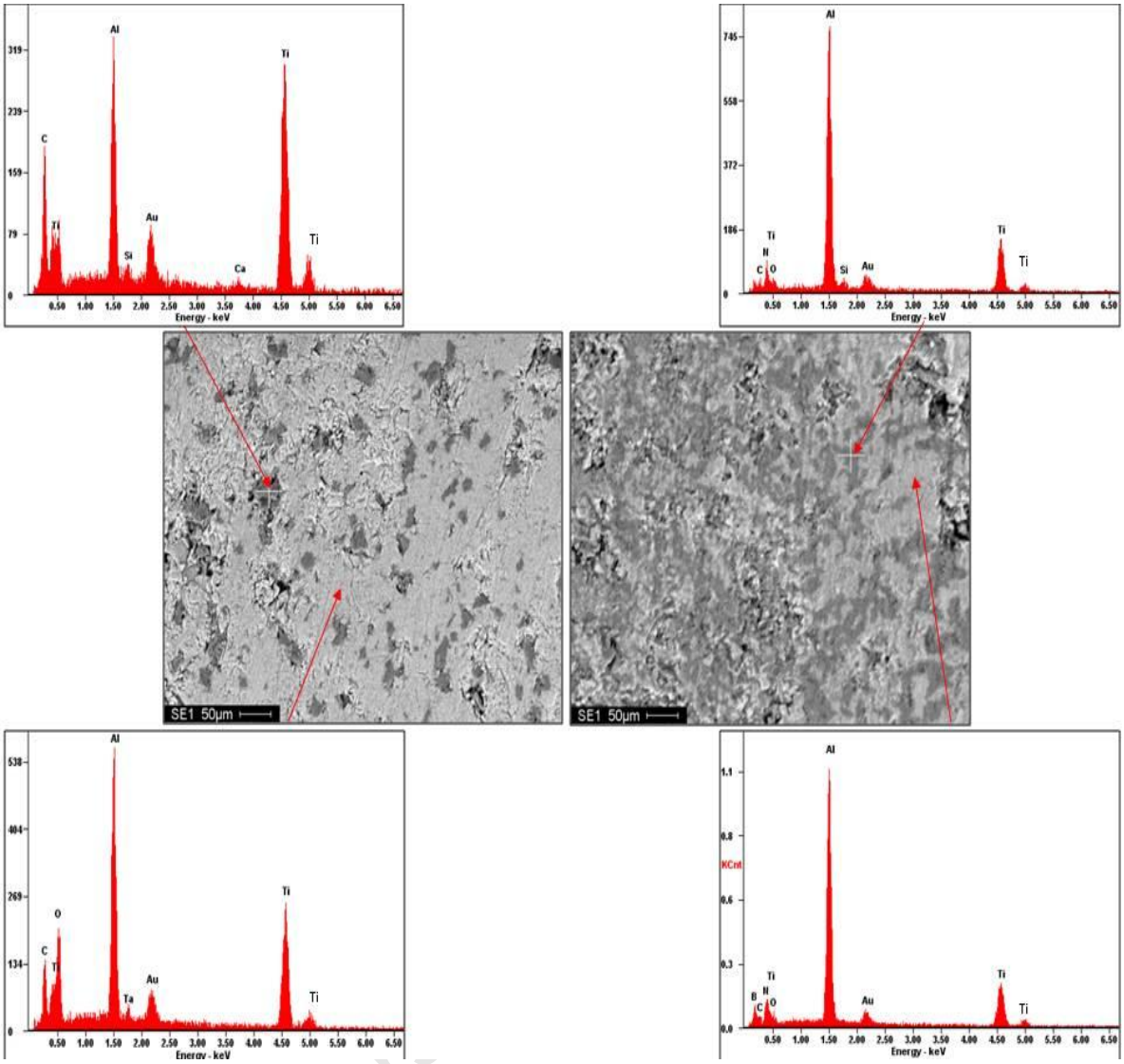

Figure 4. 17: SE image with EDS analysis the MAX phase (left) and the reaction area (right) from the reaction couple Ti_2AlC/c-BN at 1500°C, 30 minute and ambient pressure.

Figure 4.17 is an EDS analysis of the MAX phase and the reaction area of the reaction couple in figure 4.15: on the MAX phase side, the dark grey phases contain Ti, Al, Si, C and some Au and Ca contaminations, (MAX phase, and SiC and other contaminations) and the white phase contains Ti, C, O and Al, (MAX phase, alumina and some Ta, Au contaminations). On the reaction area side, the darker phase contains Ti, Al, C, O and N (alumina, AlN, TiC, TiN and possible SiC contamination) and the lighter phase contains Ti, Al, C, B, O and N (alumina, AlN, TiC and TiB_2).

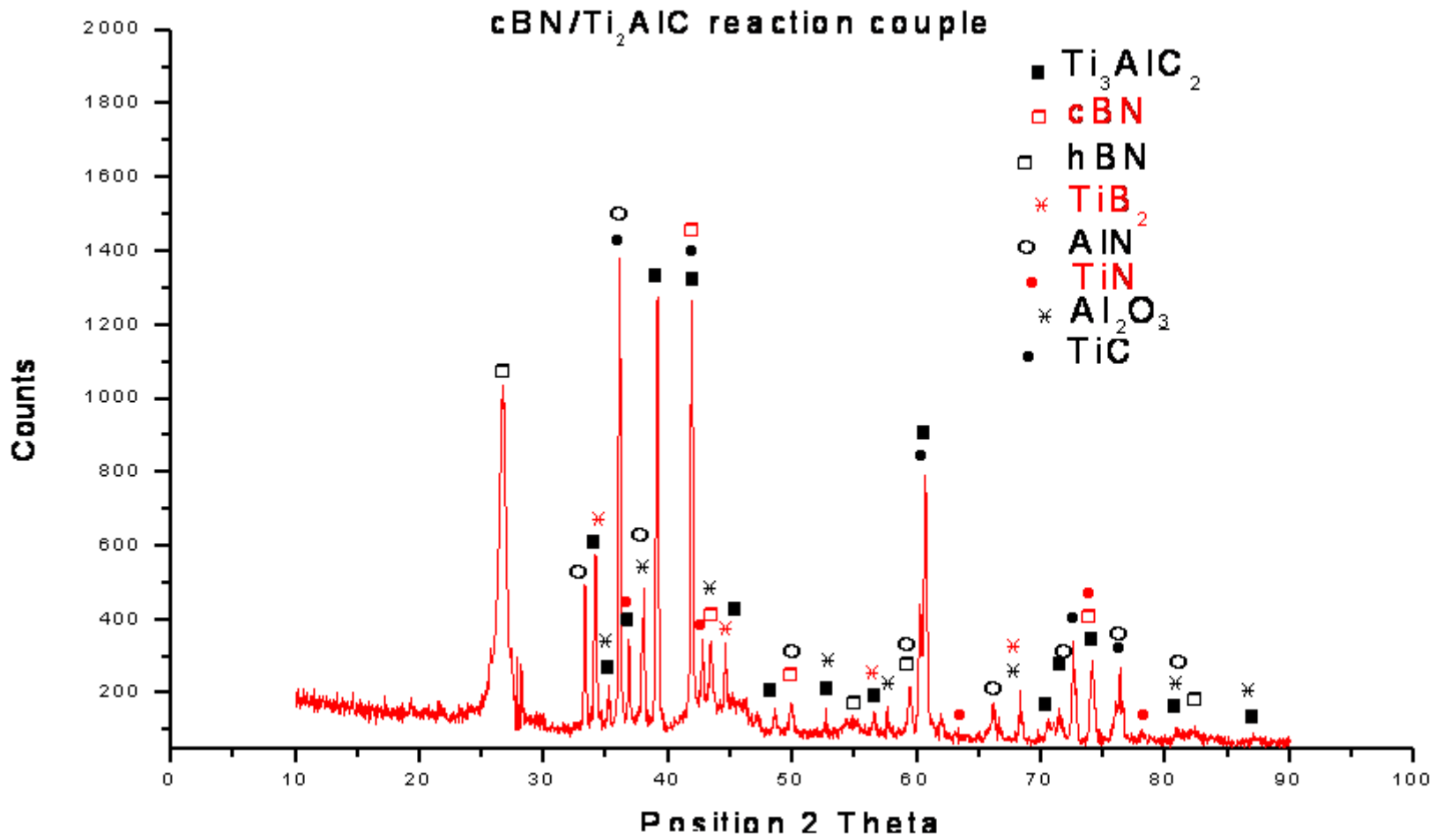

Figure 4. 18: Diffractogram of the reaction couple Ti_2AlC/c-BN sintered at 1500°C, 30 minutes, and ambient pressure.

Figure 4.18 shows the XRD data from the reaction couple shown in figure 4.15 which reveals that there was a transformation of Ti_2AlC to Ti_3AlC_2 and partially of c-BN to h-BN, since h-BN is the main phase. There is also some evidence of TiC, Al_2O_3, AlN, TiN and TiB_2 secondary phases present as seen in figure 4.17

4.3.1.2 Reaction using 10MPa pressure at 1500°C for 30 minutes

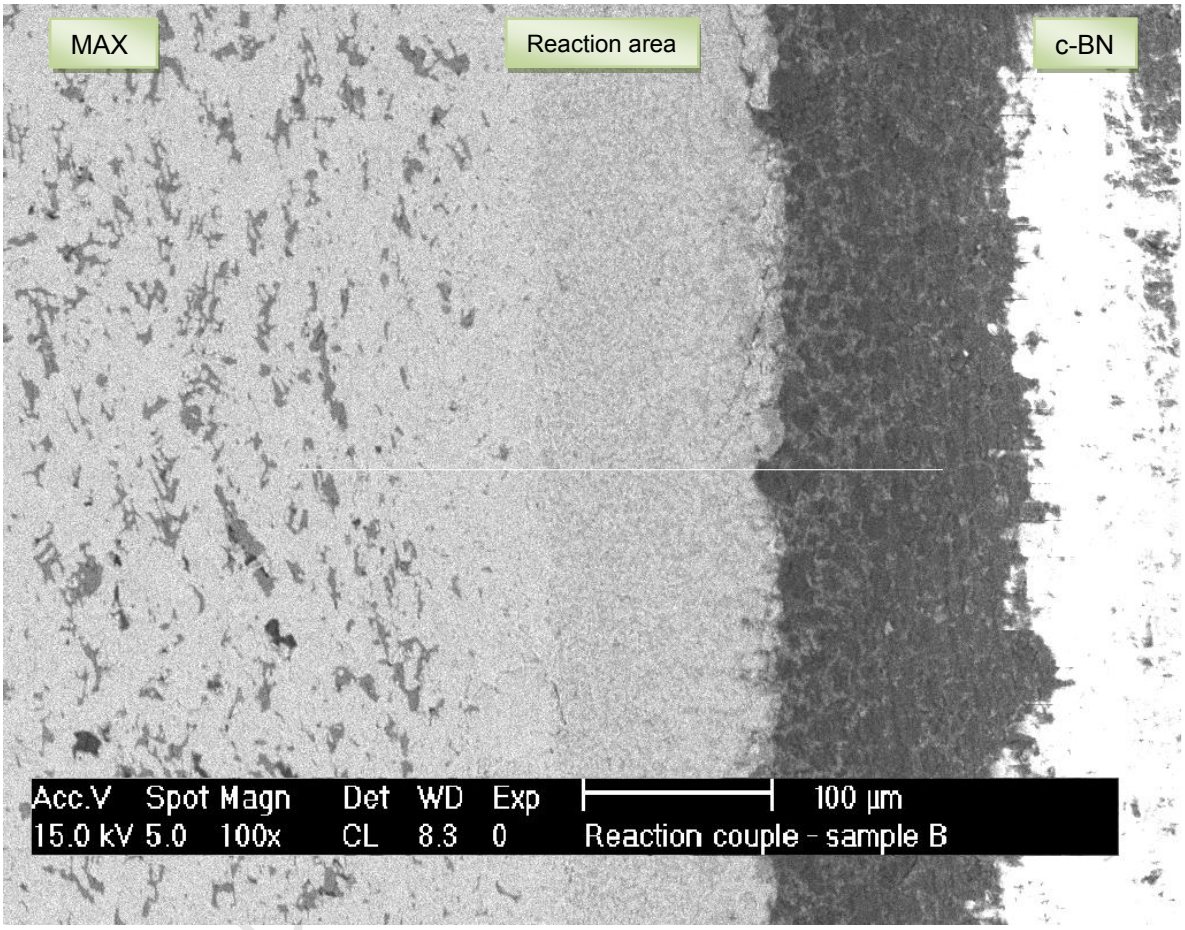

Figure 4. 19: Back scattered (CL) image of the reaction couple Ti_2AlC/c-BN reacted at 1500°C, 30 minute and 10MPa pressure.

Figure 4.19 shows an image of the reaction couple reacted at 1500°C for 30 minutes at 10MPa pressure: from this image we can see no pores between the MAX phase and the reaction zone (~110µm), unlike in figure 4.15. The surface of the c-BN sample which was in contact with the MAX phase was flat before the reaction was performed, and now it is uneven showing that the c-BN on the surface interacted with the MAX phase at this temperature.

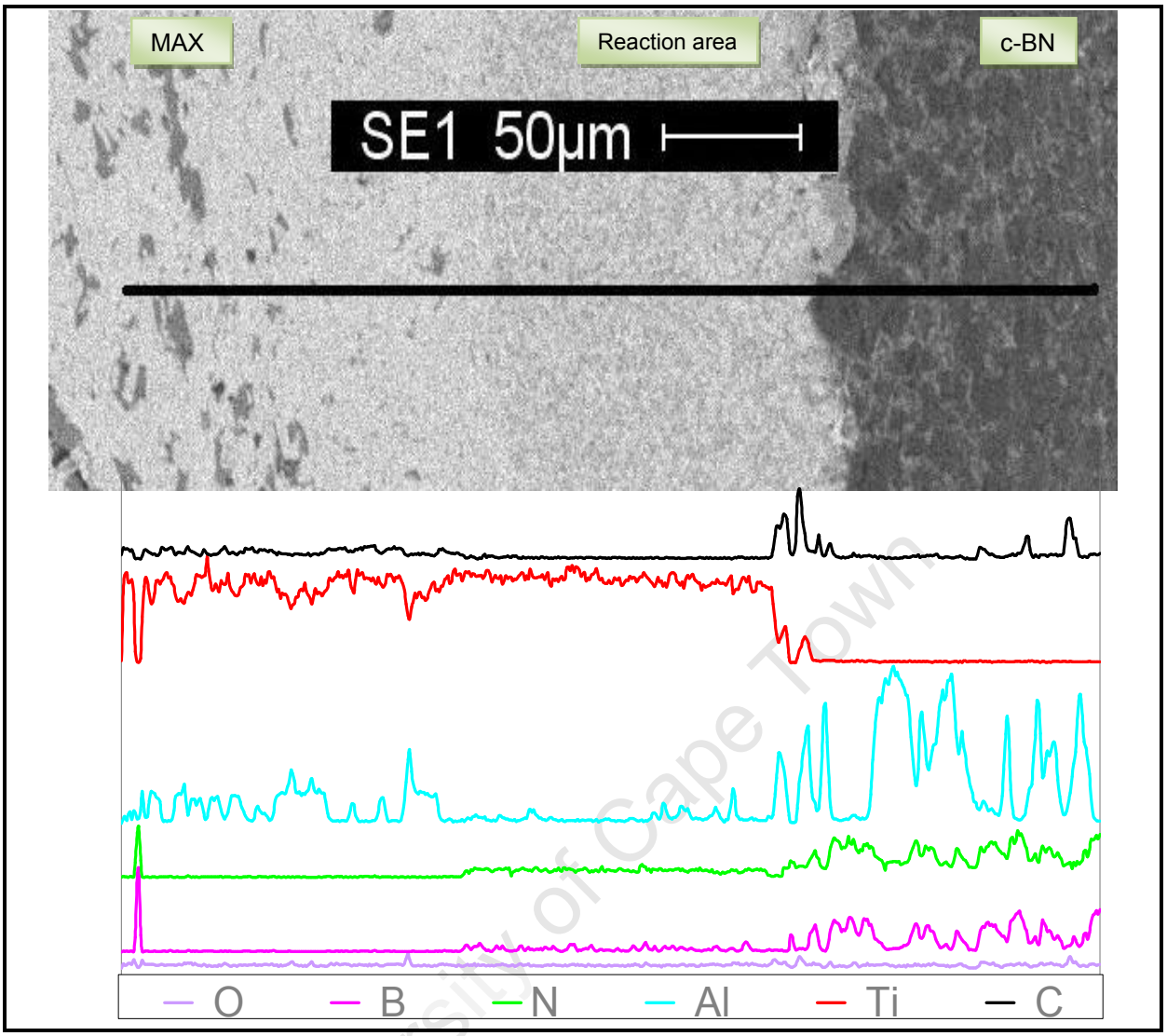

Figure 4. 20: SE image with EDS line scan of the reaction couple Ti_2AlC/c-BN at 1500°C, 30minute and 10MPa pressure.

Figure 4.20 shows an EDS line scan of the reaction couple Ti_2AlC/c-BN. There is some oxide contamination observed across the couple. Boron and nitrogen concentration is high across the c-BN region, with less across the reaction region and levelled off across the MAX phase. Aluminium concentration is markedly high across the c-BN, a bit less across the MAX phase and much less, but present, across the reaction area. Ti concentration is high across the MAX phase, with less across the reaction region and levelled off across the c-BN. Carbon is present in the MAX phase and the reaction area, and there are some peaks observed in the c-BN

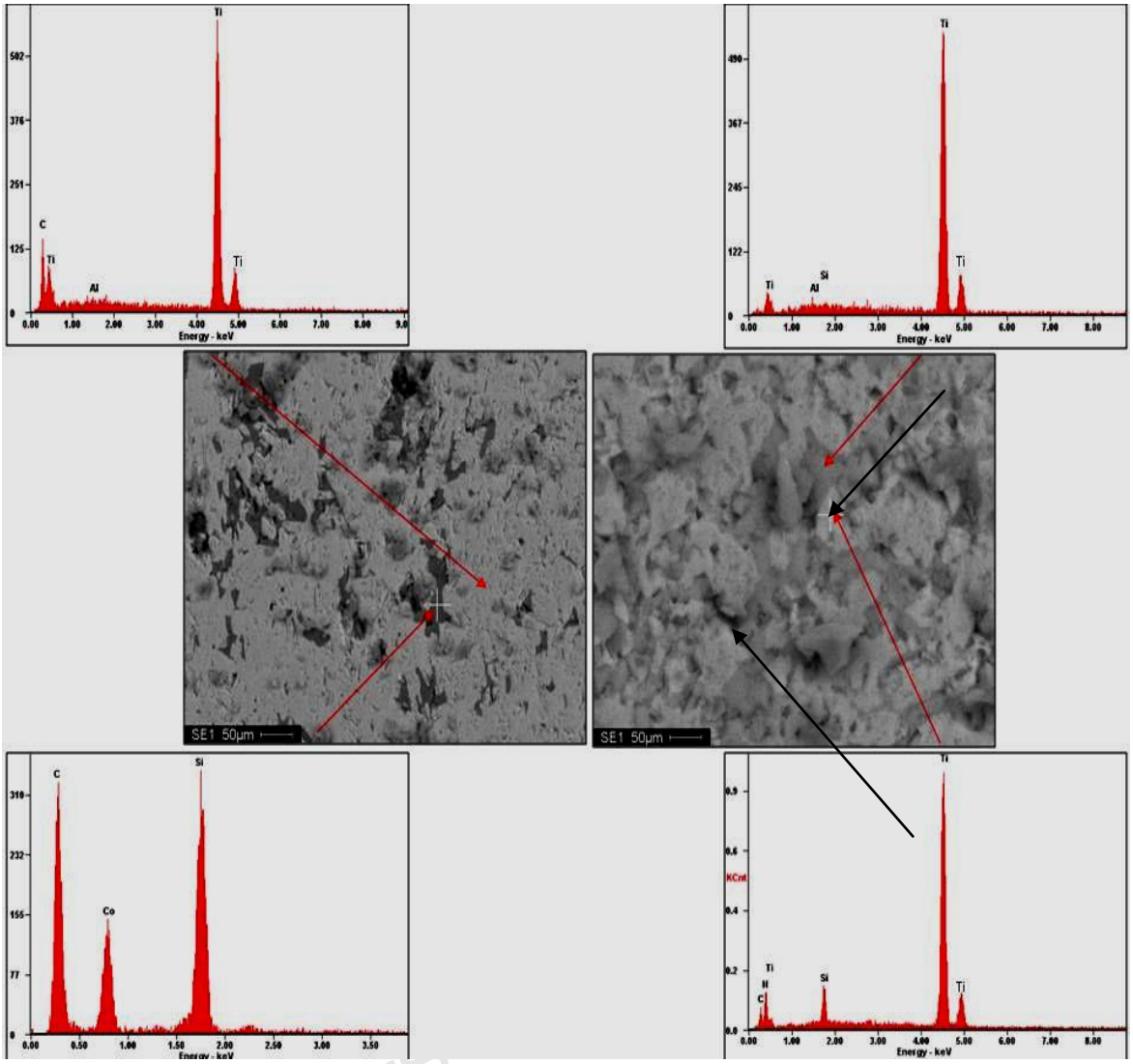

Figure 4. 21: SE image with EDS analysis of the MAX phase (left) and the reaction area (right) from the reaction couple Ti_2AlC/c-BN sintered at 1500°C, 30 minute and 10MPa pressure.

Figure 4.21 is an EDS analysis of the MAX phase and the reaction area of the reaction couple in figure 4.19: on the MAX phase side, the dark grey phases contain Ti, Al, O and C (TiC and alumina); and the white phase contains Ti, Al and C (MAX phase). On the reaction area side: the lighter phase contains Ti, C, Si and N (TiN, TiC and some possible SiC contamination); and the darker phase contains Ti and B, (TiB_2).

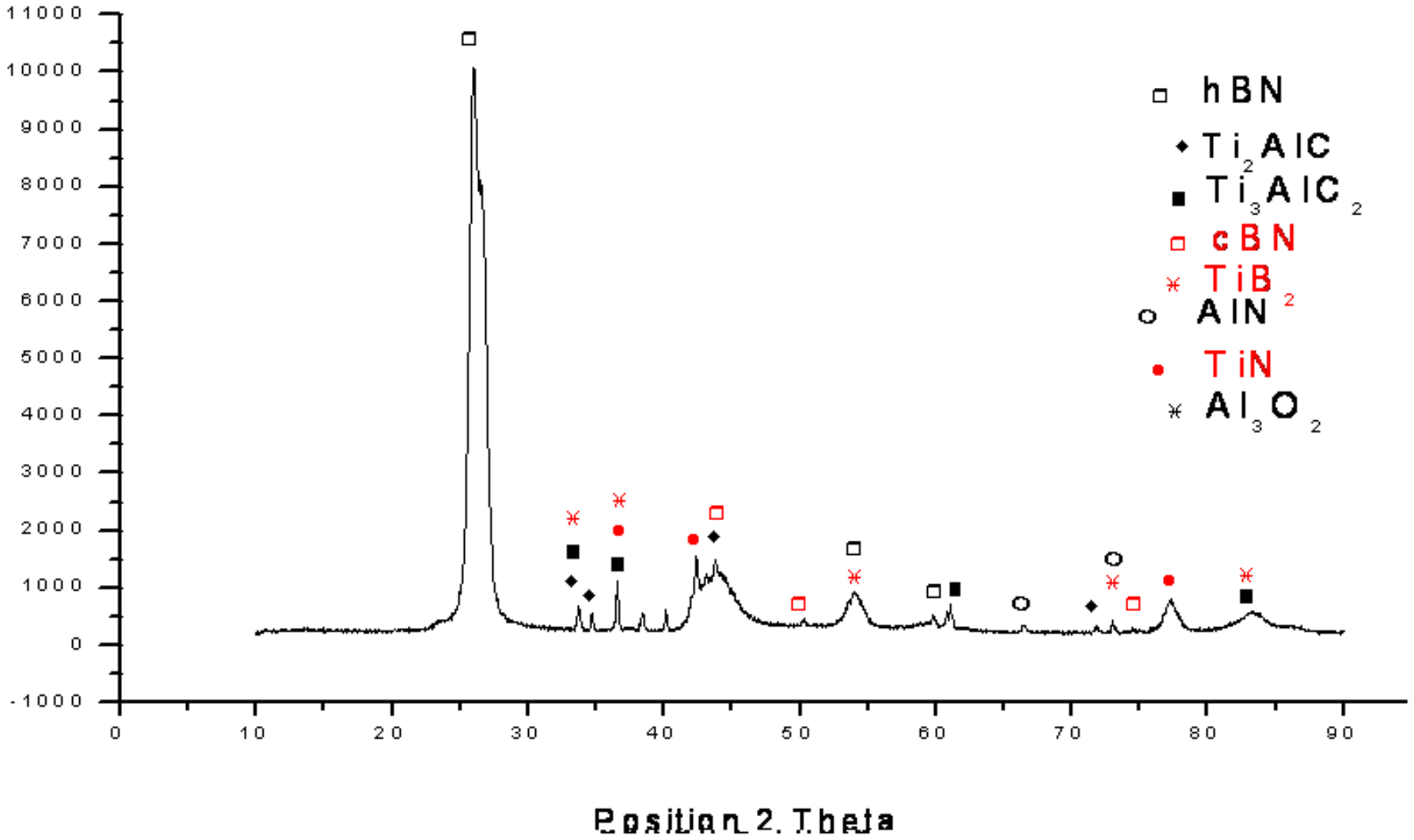

Figure 4. 22: Diffractogram of the reaction couple Ti_2AlC/c-BN at 1500°C, 30 minutes and 10MPa pressure..

Figure 4.22 Diffractogram of the reaction couple shown in figure 4.19 which reveals that there was a partial transformation of Ti_2AlC to Ti_3AlC_2 and of c-BN to h-BN, as h-BN is the main phase. There is also some evidence of TiC, Al_2O_3, AlN, TiN and TiB_2 secondary phases present as seen in figure 4.21

4.3.2 Ti_3SiC_2/c-BN reaction couples

4.3.2.1 Reaction with ambient pressure at 1500°C for 30 minutes

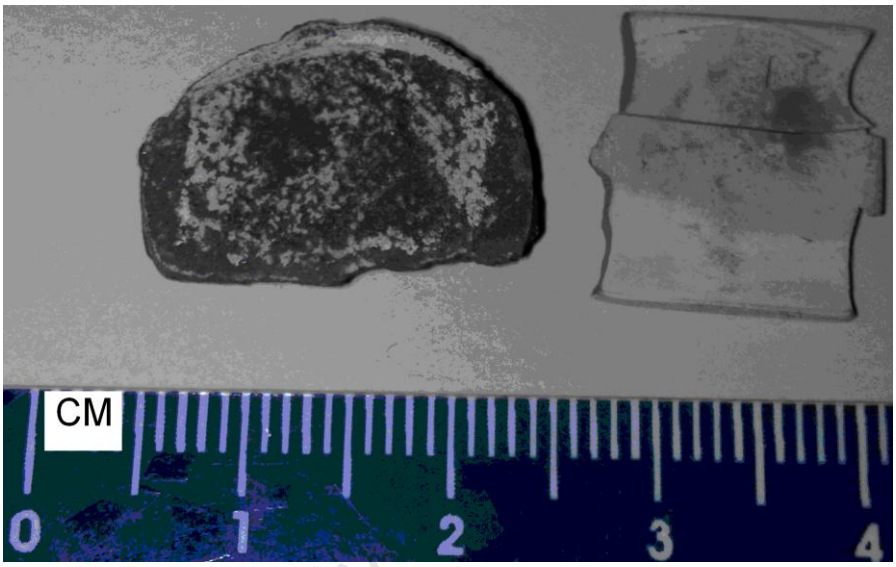

Figure 4. 23: Image of the reaction site of the samples Ti_3SiC_2/c-BN reacted at 1500°C, 30 minutes, ambient pressure.

Figure 4.23 is an image of the c-BN sample (right) and Ti_3SiC_2 sample (left) reacted at 1500°C, 30 minutes and ambient pressure. There was no reaction between the two samples; which separated as soon as they were taken out of the graphite pot. There is some residue of h-BN on the MAX phase sample where there was contact between the two samples. The sample appears to have undergone some decomposition because, unlike a non-reacted MAX phase sample which has a metallic lustre, this sample seems to have carburised or turned black. Figure 4.24 below confirms these observations, with the XRD analysis of a non-reacted Ti_3SiC_2 and the Ti_3SiC_2 sample shown in figure 4.23 (right), revealing a few Ti_3SiC_2 peaks disappearing after heating. There is also an appearance of some TiB_2 and TiN in addition to the Ti_3SiC_2, TiC and SiC phases that are present also in the non-reacted Ti_3SiC_2 sample.

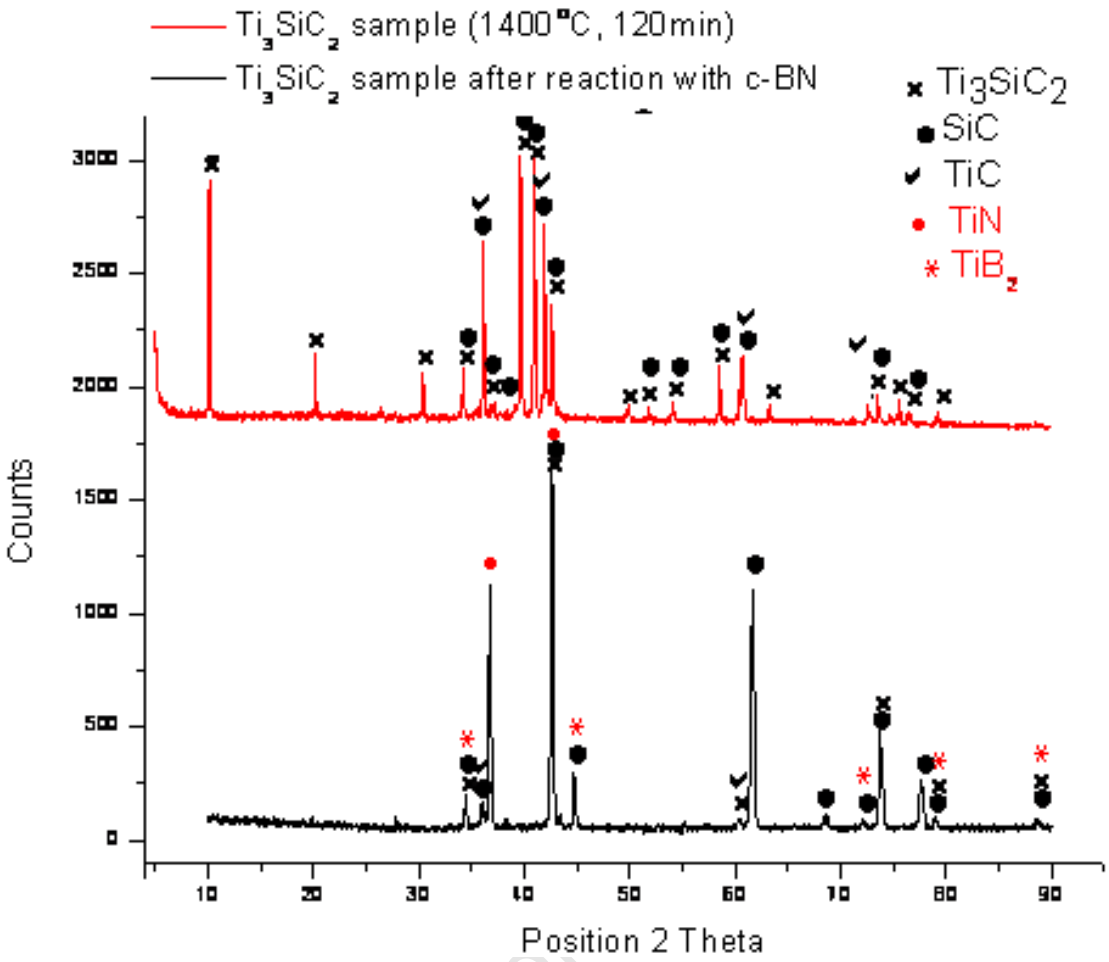

Figure 4. 24: Diffractogram of the reaction site of Ti_3SiC_2 reacted with c-BN at 1500°C, 30 minutes and ambient pressure (shown in figure 4.23 (left)), and a sample of Ti_3SiC_2 (which has not undergone a reaction in a reaction couple).

Figure 4.25 is an image of a non-reacted c-BN sample (left) and a reaction c-BN sample (right) reacted at 1500°C, 30 minutes and ambient pressure. There is an observed change in dimensions and colour. The sample shows some transformation because, unlike the non-reacted c-BN sample which is darker and smaller, this sample has increased in size and became lighter in colour. Figure 4.30 with the XRD analysis of a non-reacted c-BN (figure 4.25 left) and the c-BN sample shown in figure 4.25 (right), reveals that the sample before and after the reaction shows no change at all.

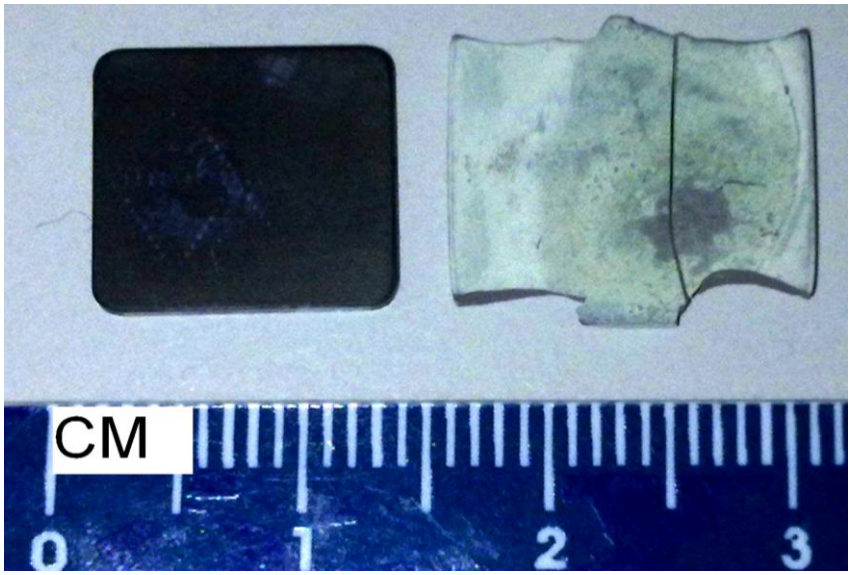

Figure 4. 25: Image showing the colour and dimension change in the c-BN used for the reaction (right) with Ti_3SiC_2 at 1500°C, 30 minutes and ambient pressure.

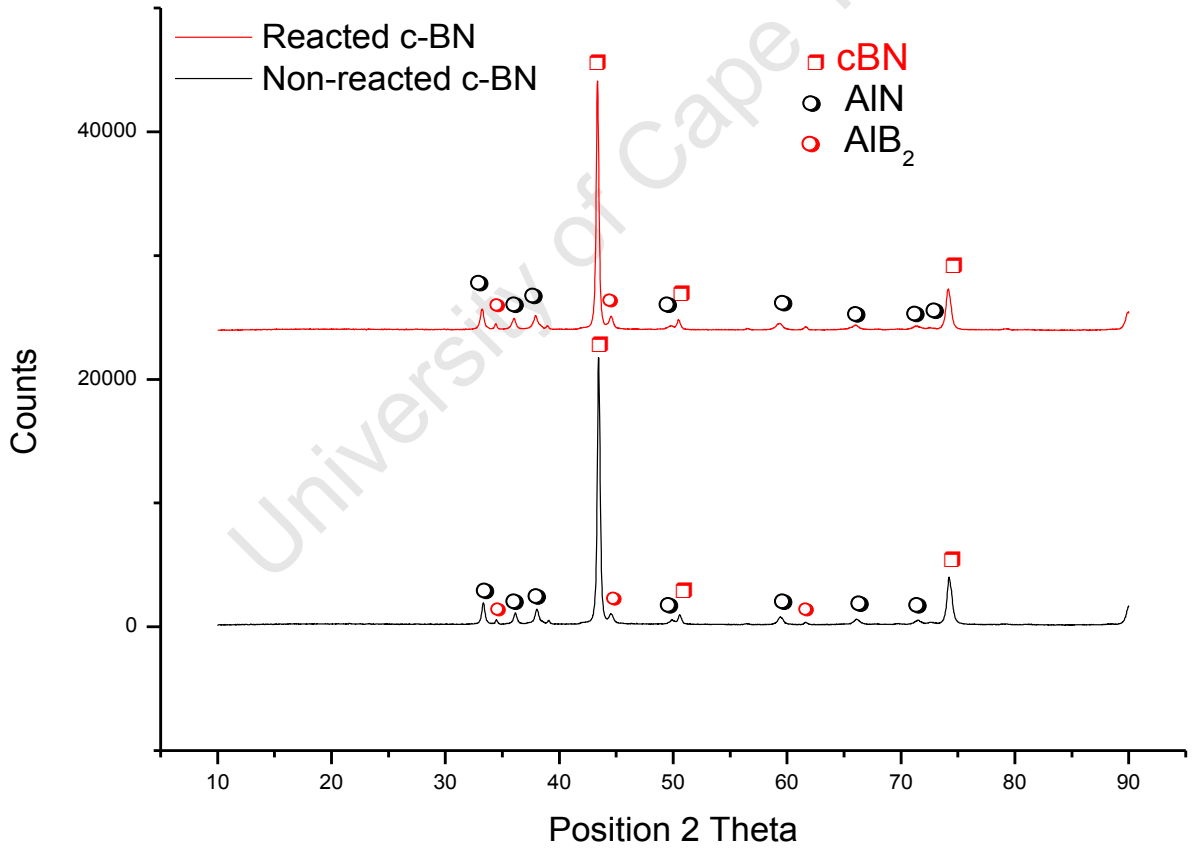

Figure 4. 26: Diffractogram of the reaction site of the reaction c-BN reacted with Ti_3SiC_2 at 1500°C, 30 minutes and ambient pressure (shown in figure 4.21 (right)) and a sample of c-BN not undergone any reaction in a reaction couple.

4.3.2.2 Reaction at 10MPa pressure at 1400°C for 30 minutes

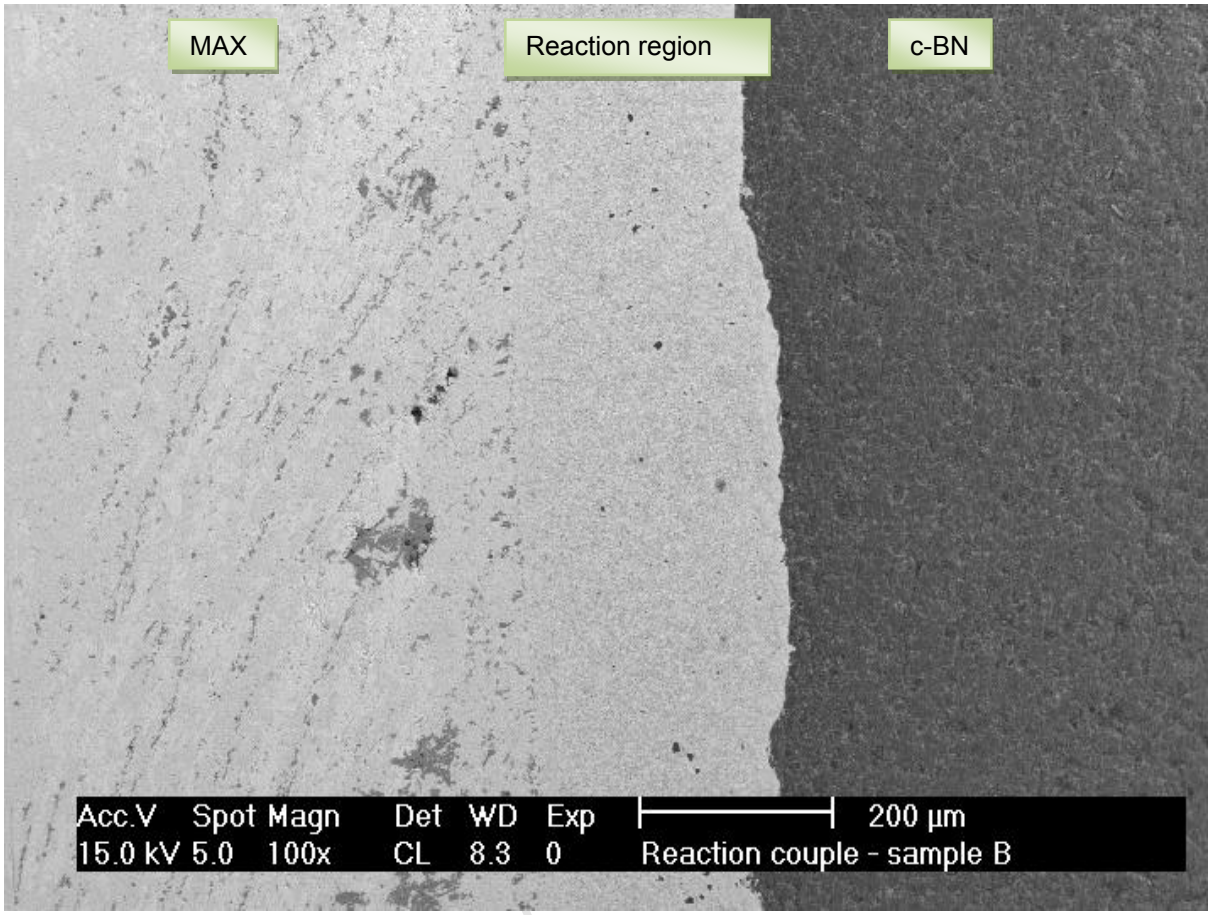

Figure 4. 27: Back scattered (CL) image of the reaction couple Ti_3SiC_2/c-BN reacted at 1400°C, 30 minute and 10MPa pressure.

Figure 4.27 shows an image of the reaction couple reacted at 1400°C for 30 minutes at ambient 10MPa pressure; from this image we can see there are no pores between the MAX phase and the reaction zone unlike in figure 4.15. The site of the c-BN sample which was in contact with the MAX phase was flat before the reaction was performed, and now it looks uneven showing that the c-BN on the surface interacted with the MAX phase at this temperature.

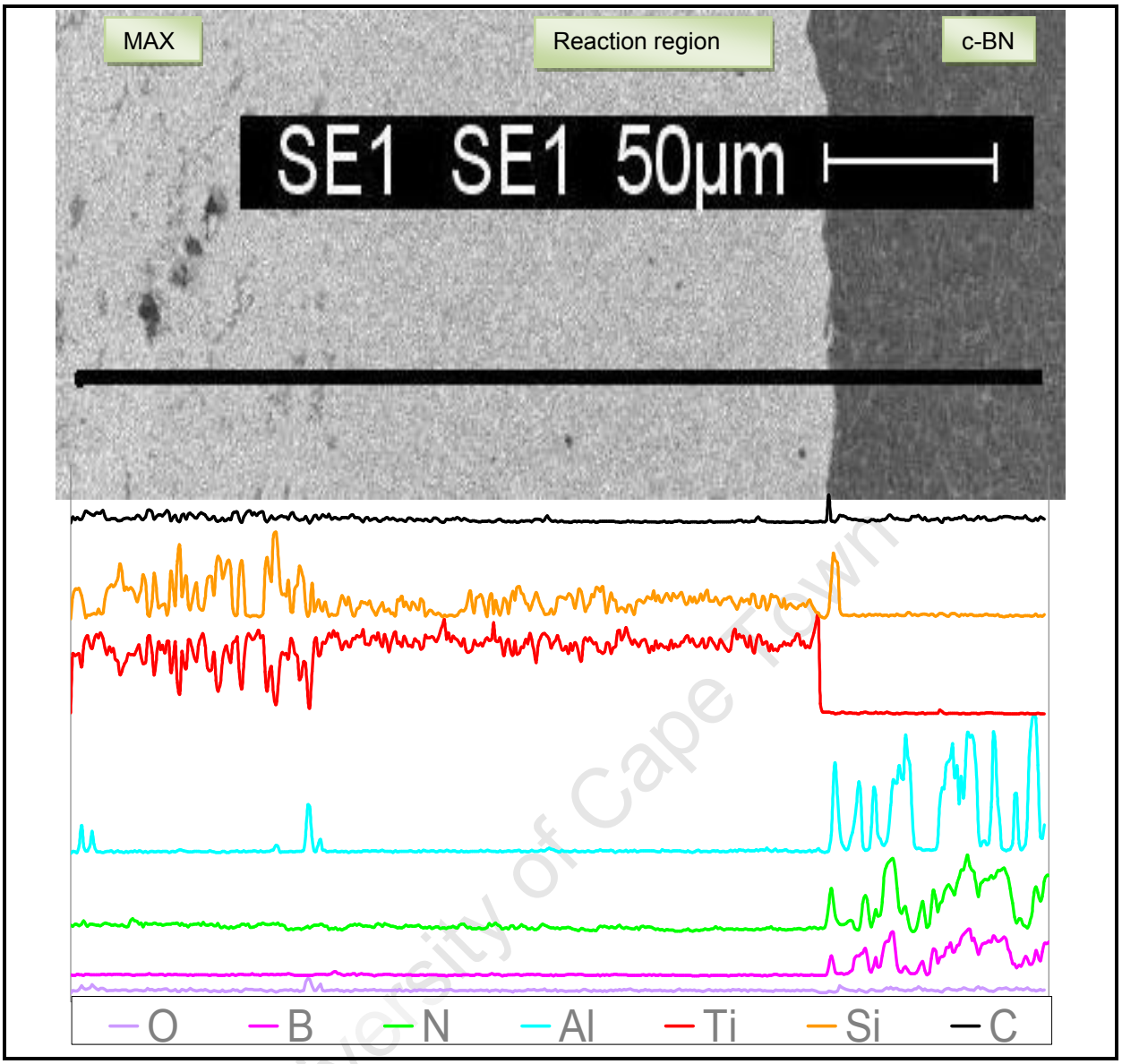

Figure 4. 28: SE image with EDS line scan of the reaction couple Ti_3SiC_2/c-BN at 1400°C, 30 minute and 10MPa pressure.

Figure 4.28 shows the line scan of the reaction couple Ti_3SiC_2/c-BN. There is an oxide contamination observed across the couple. Boron and nitrogen concentration is high across the c-BN region, low across the reaction region and across the MAX phase, but the B seems depleted at the Max phase unlike N. Aluminium concentration is high across the c-BN and also levelled off uniform across the reaction region and the MAX phase; Ti and Si concentration is present across the MAX phase, some across the reaction region and levelled depleted across the c-BN.

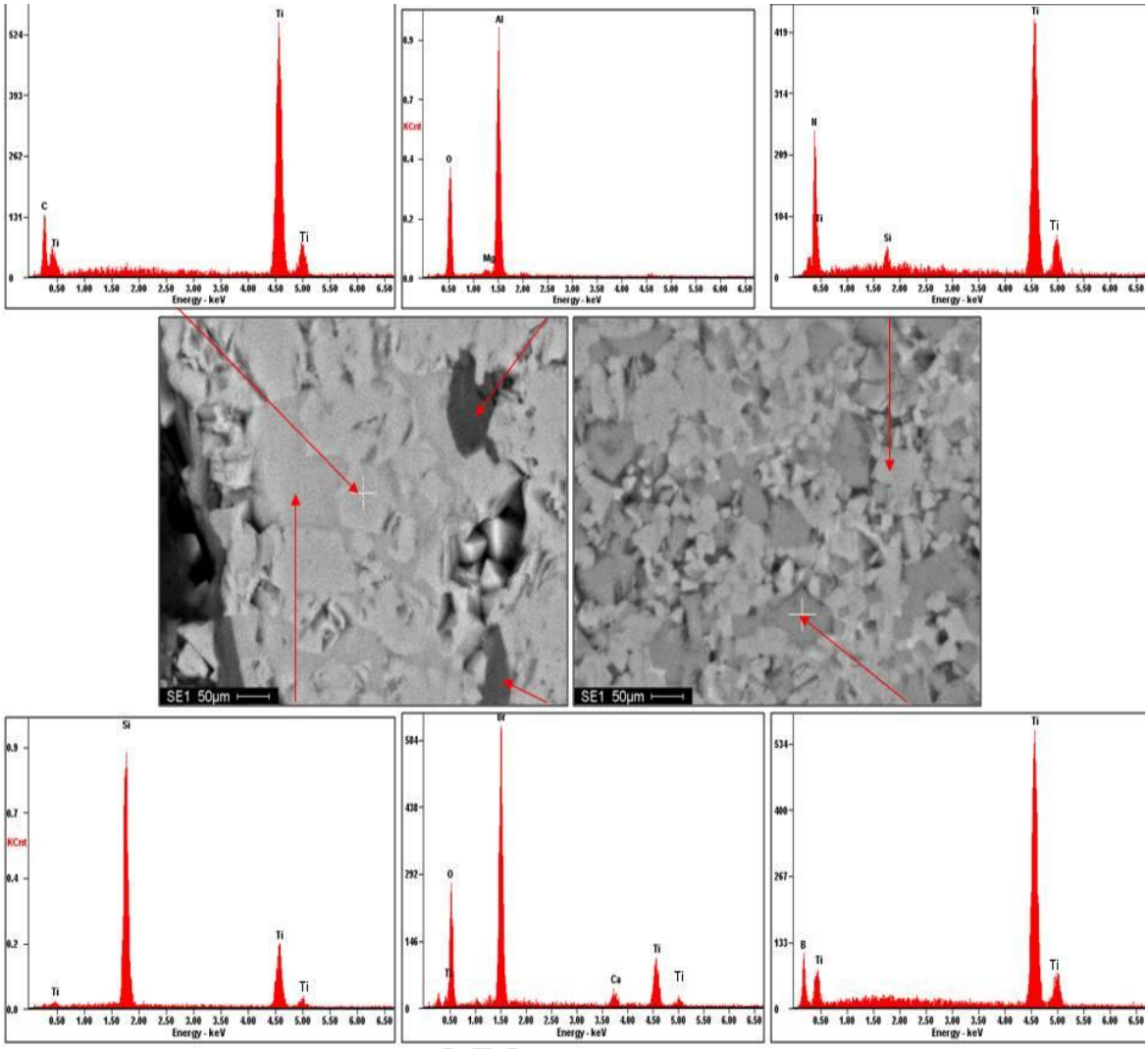

Figure 4. 29: SE image with EDS analysis the MAX phase (left) and the reaction area (right) from the reaction couple Ti_3SiC_2/c-BN at 1400°C, 30 minute and 10MPa pressure.

Figure 4.29 is an EDS analysis of the MAX phase and the reaction area of the reaction couple in figure 4.27: on the MAX phase side, the dark grey phases are alumina (top centre) and SiC (bottom centre), the light grey phase contains Ti and Si ($TiSi_2$) and the white phase contains Ti and C (TiC). On the reaction area side the darker phase contains Ti and B (TiB_2); and the lighter phase contains Ti, Si and N, (TIN and $TiSi_2$).

Figure 4.30 shows the XRD results of the reaction couple shown in figure 4.27. It shows the presence of c-BN and Ti_3SiC_2, but also some TiC, SiC, AlN, TiN and TiB_2 secondary phases present as seen in figure 4.29.

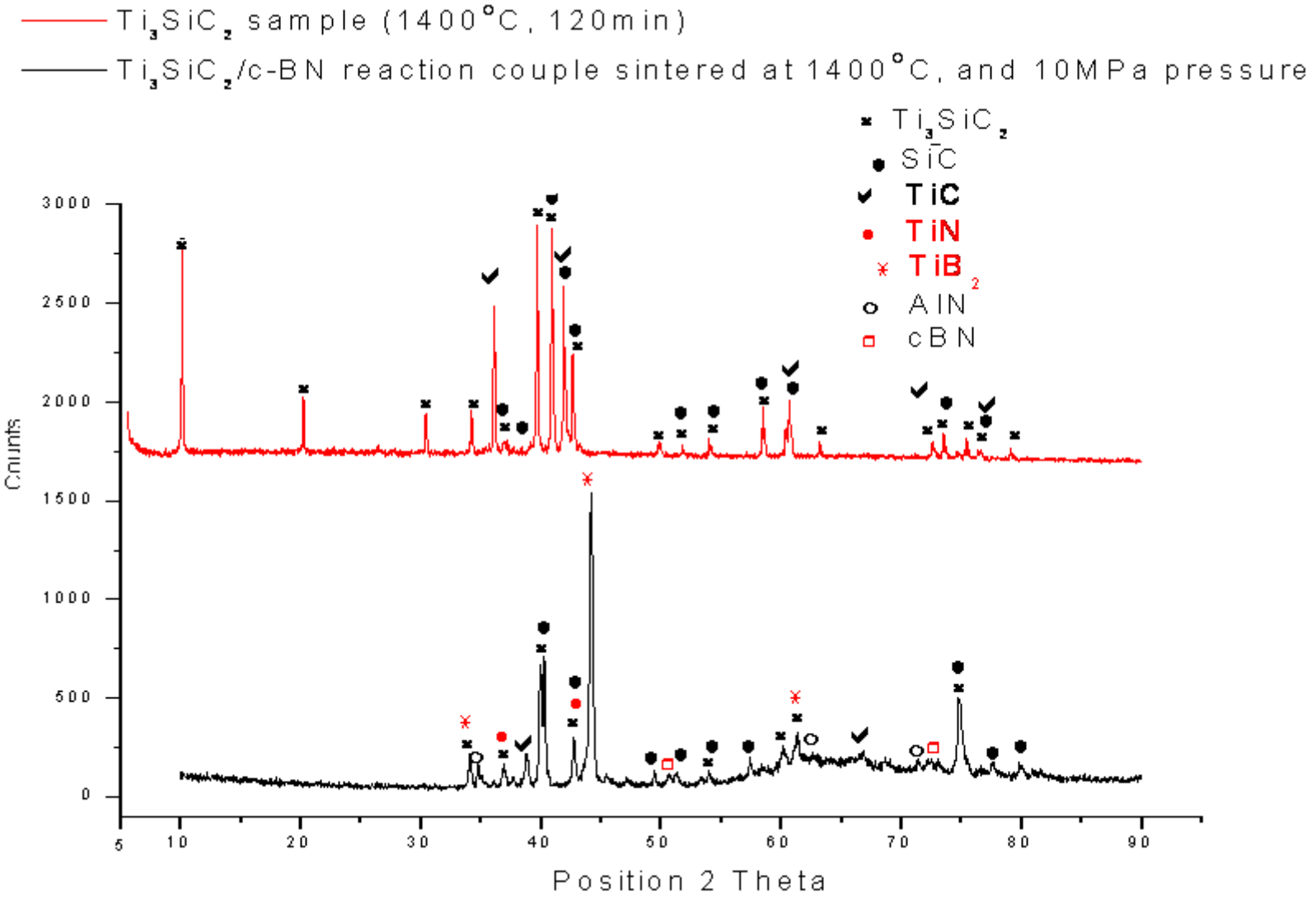

Figure 4. 30: Diffractogram of the reaction couple Ti_3SiC_2/c-BN at 1400°C, 30 minute and 10MPa pressure.

4.4 Composites

Composites of a MAX phase and c-BN were sintered as described in Section 3.4. The resulting composite materials were characterised by compositional analysis of polished sections, and also by examination of fracture surfaces.

4.4.1 Ti_2AlC/c-BN composite

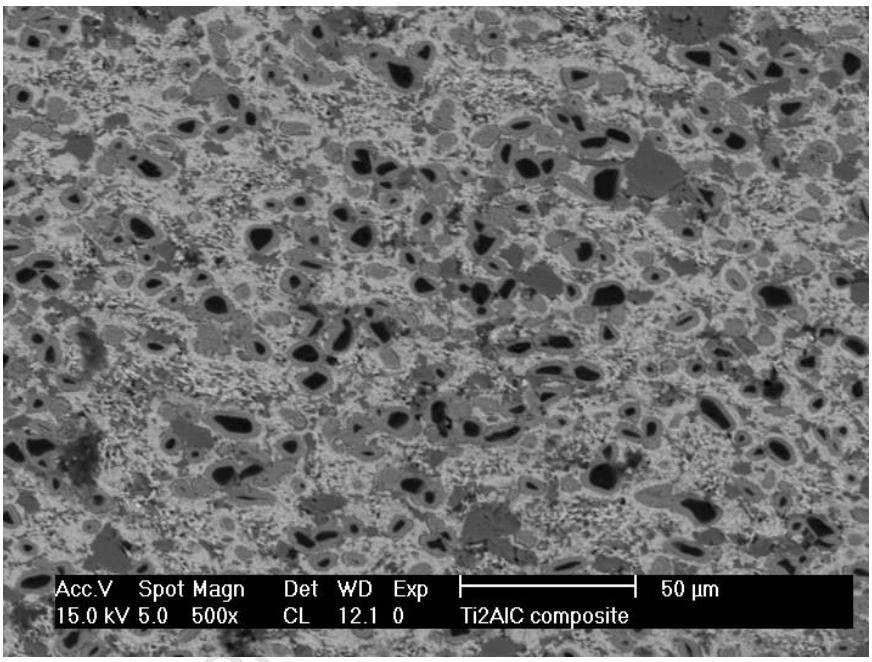

Figure 4. 31: SEM BSE (CL) image of Ti_2AlC/c-BN composite sintered at 10MPa, 1500°C for 30 minutes.

Figure 4.31 shows a SEM image of a polished cross section of a spark plasma sintered Ti_2AlC/c-BN composite. A black phase is seen to be dispersed in a matrix of white and dark grey. The black areas are surrounded by a light grey phase "rim". Figure 4.32 is an EDS analysis of the different phases seen in figure 4.31, and figure 4.33 is a higher magnification EDS analysis of figure 4.32: The black phases are c-BN (fig 4.32) and the light grey rim around them is the reaction area containing Ti, Al, B and nitrogen (fig 4.36 and fig 4.33): this could be TiAl, and TiB_2. The larger dark grey phases are Al_2O_3 (fig 4.32), from the milling balls. The lighter grey phases seen in fig 4.33 contain Ti and B: this could be TiB_2. The white phase contains Ti, Al and C, and could be the MAX phase. The dark grey phase lining the reaction area contains mainly Al

and some Ti, N and oxygen. Overall, the c-BN is seen to be well dispersed in the MAX phase matrix.

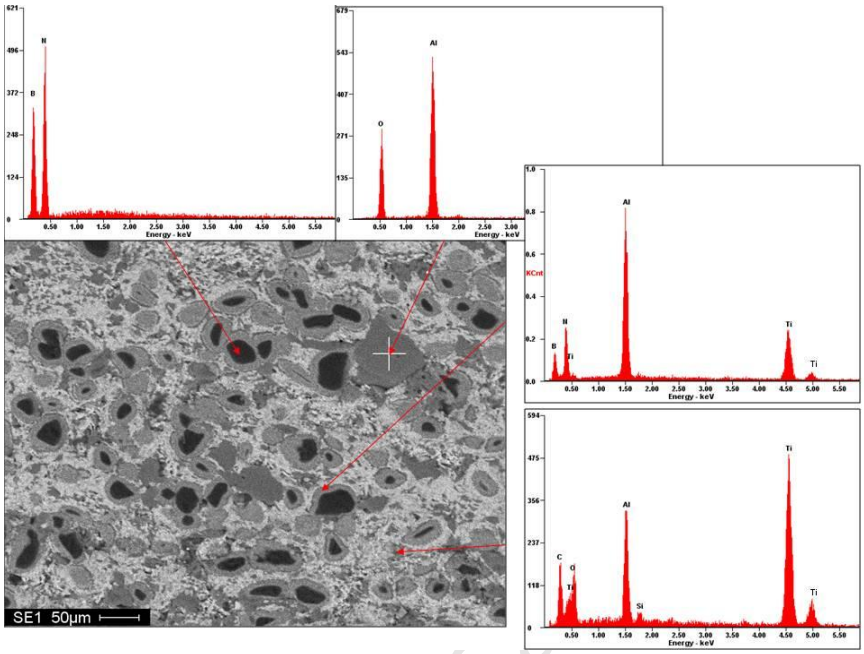

Figure 4. 32:SE image with EDS analysis of Ti_2AlC/c-BN composite.

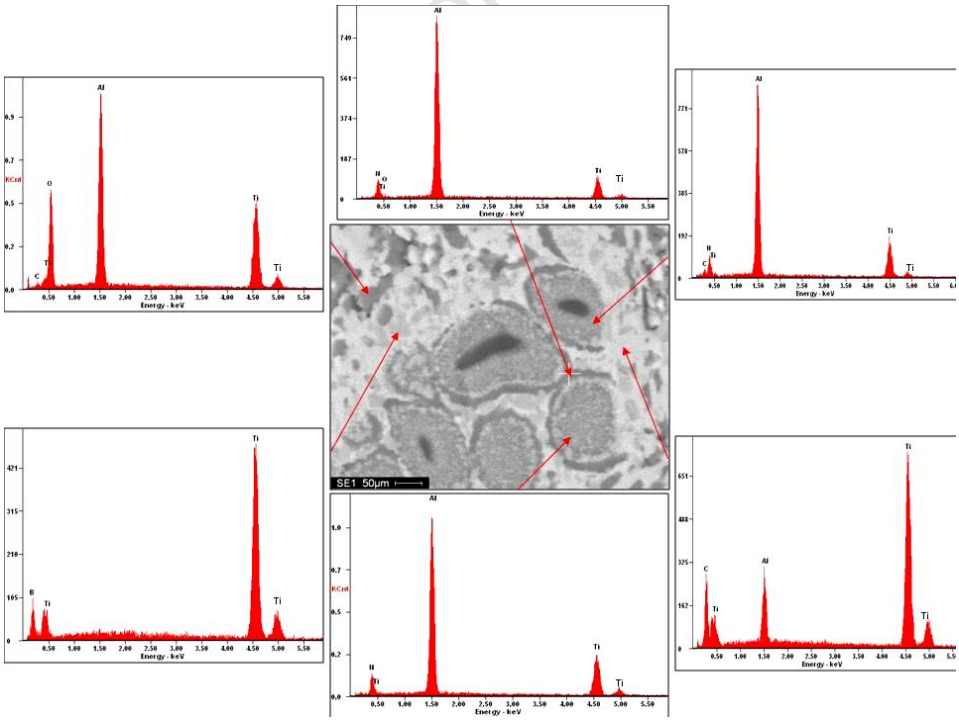

Figure 4. 33: EDS secondary electron (SE) image analysis of Ti_2AlC/c-BN composite at a higher magnification.

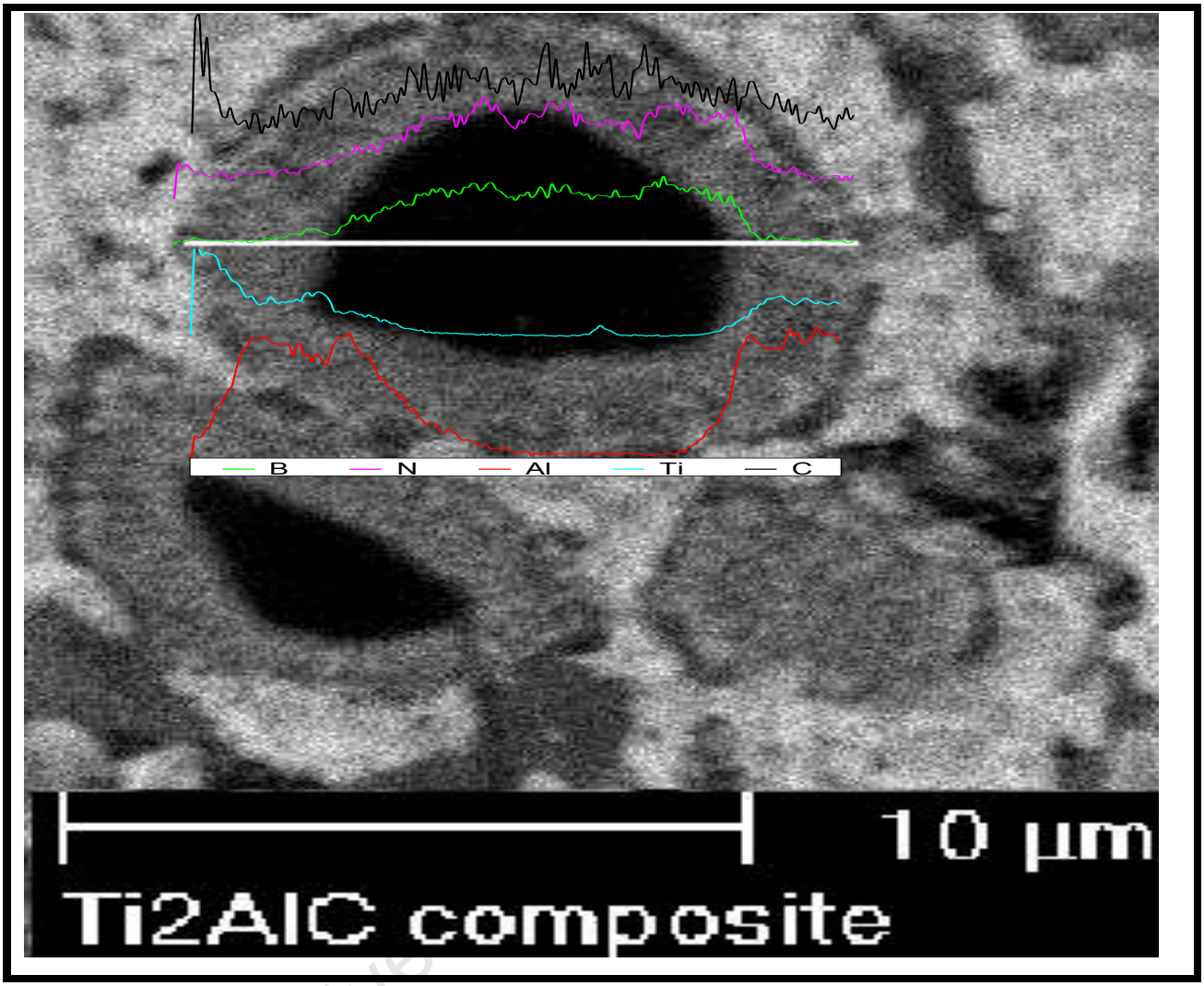

Figure 4. 34: Enlarged SE image with EDS line scan of the Ti_2AlC/c-BN composite sintered at 1500°C, 30 minute and 10MPa pressure.

Figure 4.34 shows an EDS line scan of the Ti_2AlC/c-BN reaction area around a c-BN particle. The scan shows that B and N peak where the line crosses the c-BN phase and decrease but are still present across the reaction area. The Ti and Al reduce across the c-BN phase but gradually increase across the reaction area. The Al decreases at the region nearer to the c-BN but increases in some regions of the reaction area. The presence of Al, Ti, B and N in the reaction region around the c-BN shows that the two materials reacted at these conditions as predicted by the reaction couples in section 4.3.1. The reaction region, however, seems to be thicker than desired.

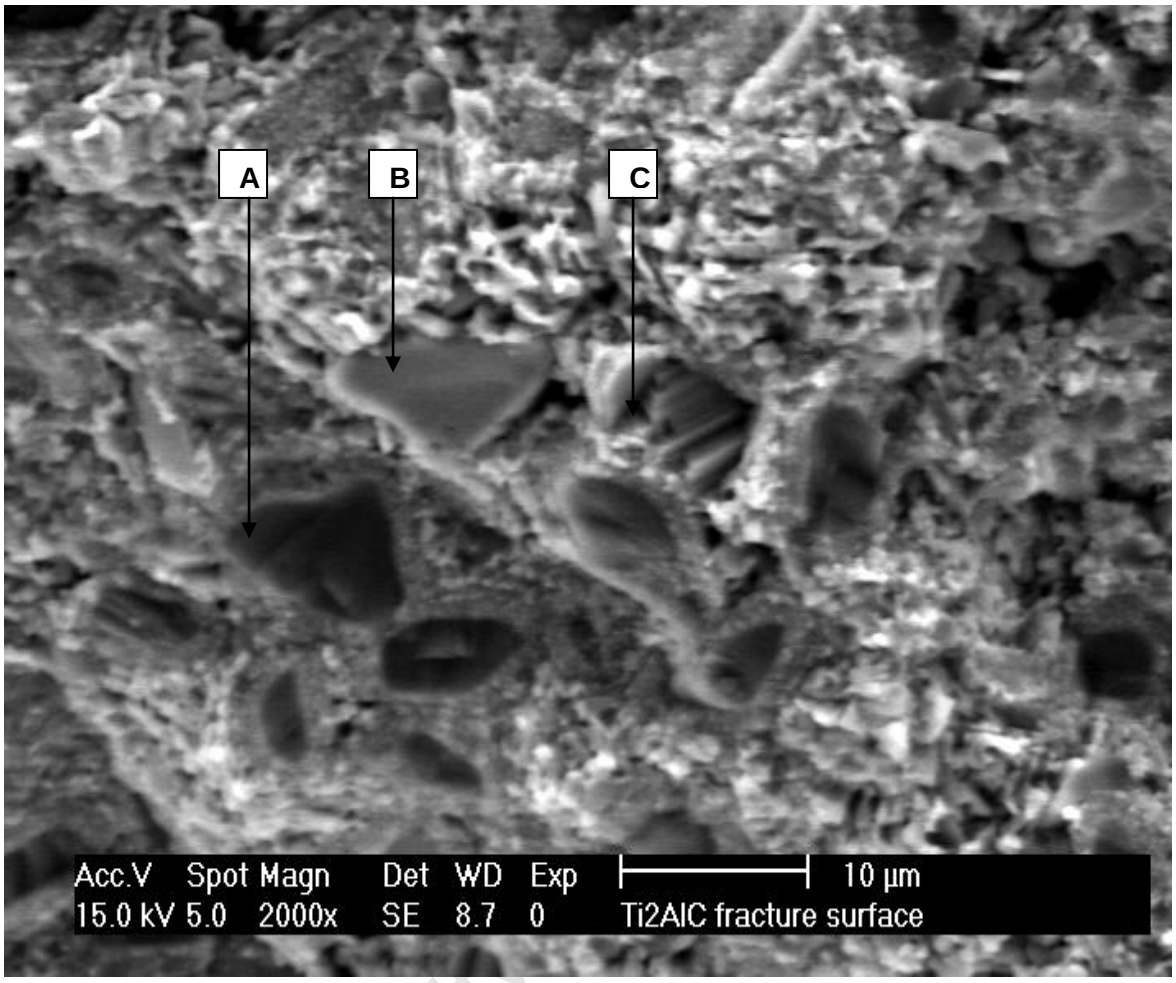

Figure 4. 35: SEM SE image of Ti_2AlC/c-BN composite fracture surface sintered at 10MPa, 1500°C for 30 minutes.

Figure 4.35 shows the fracture surface of a Ti_2AlC/c-BN composite. Three types of micro-structural region may be observed: c-BN without a reaction region on the exposed surface (A); c-BN with a reaction region still around it (B); Ti_2AlC and a surrounding matrix (C). The fracture therefore appears to have stripped some c-BN particles of the reaction region rim (A), and elsewhere to have been deflected around the rim (B). The Ti_2AlC layered structure (C) also shows that the crack was deflected around the some of the MAX phase grains.

4.4.2 Ti_3SiC_2/c-BN composite

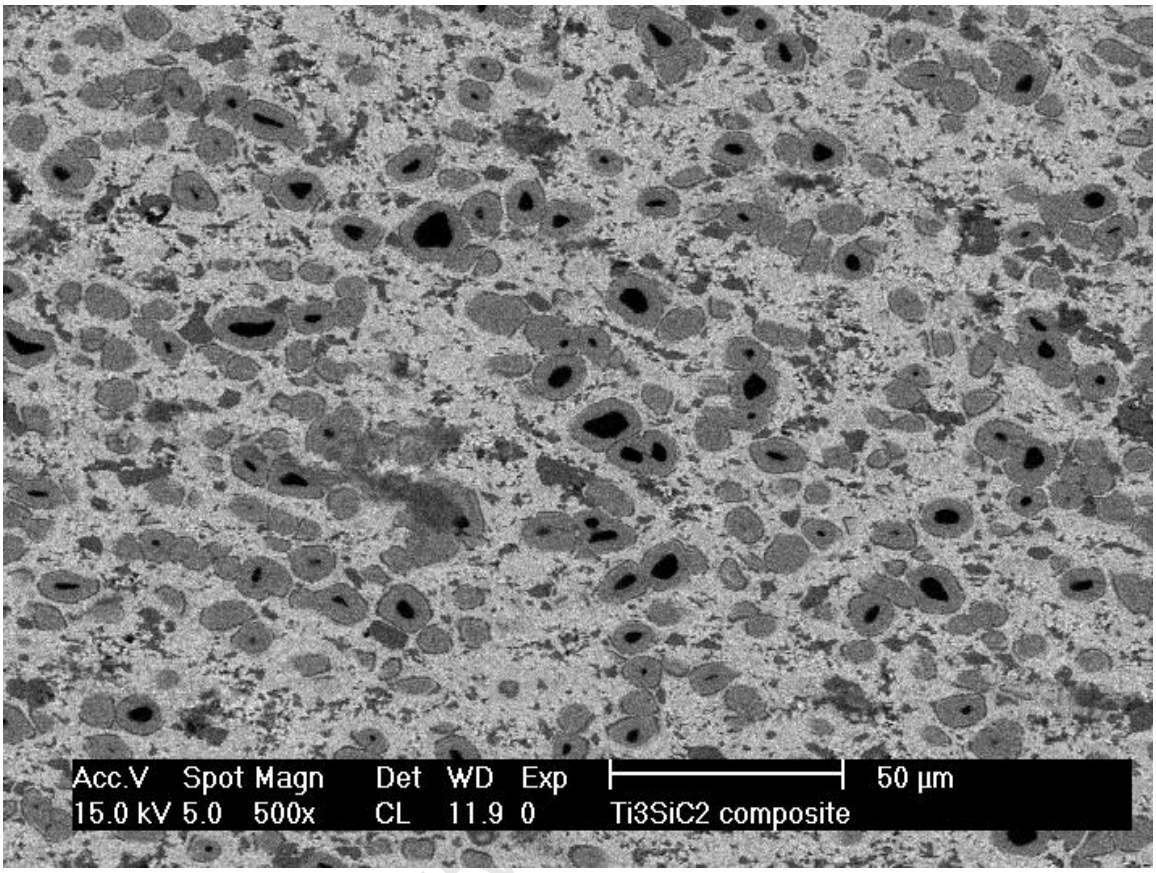

Figure 4. 36: SEM BSE (CL) image of Ti_3SiC_2/c-BN composite sintered at 10MPa, 1400°C for 30 minutes.

Figure 4.36 shows a SEM image of a polished cross section of a spark plasma sintered Ti_2AlC/c-BN composite. A black phase is seen to be dispersed in a matrix of white and dark grey. The black areas are surrounded by a light grey phase "rim". Figure 4.37 is an EDS analysis of the different phases seen in figure 4.36, and figure 4.38 is a higher magnification EDS analysis of figure 4.37: The black phases are c-BN (fig 4.37) and the light grey rim around them is the reaction area containing Ti, Al, Si N and oxygen (fig 4.37). This area therefore is likely to consist of TiAl, TiN and $TiSi_2$. The larger dark grey phases are Al_2O_3 from the milling balls(fig 4.38).The lighter grey phases seen in fig 4.37 contain Ti and B, and could be TiB_2. The white phase contains Ti, Si, C Al and boron (fig 4.38); this could be the MAX phase and some secondary phases. The dark grey phase (top left fig 4.38) contains Al, O, Ti, Si and C this could be MAX phase and alumna. Overall, the c-BN is seen to be well dispersed in the MAX phase matrix.

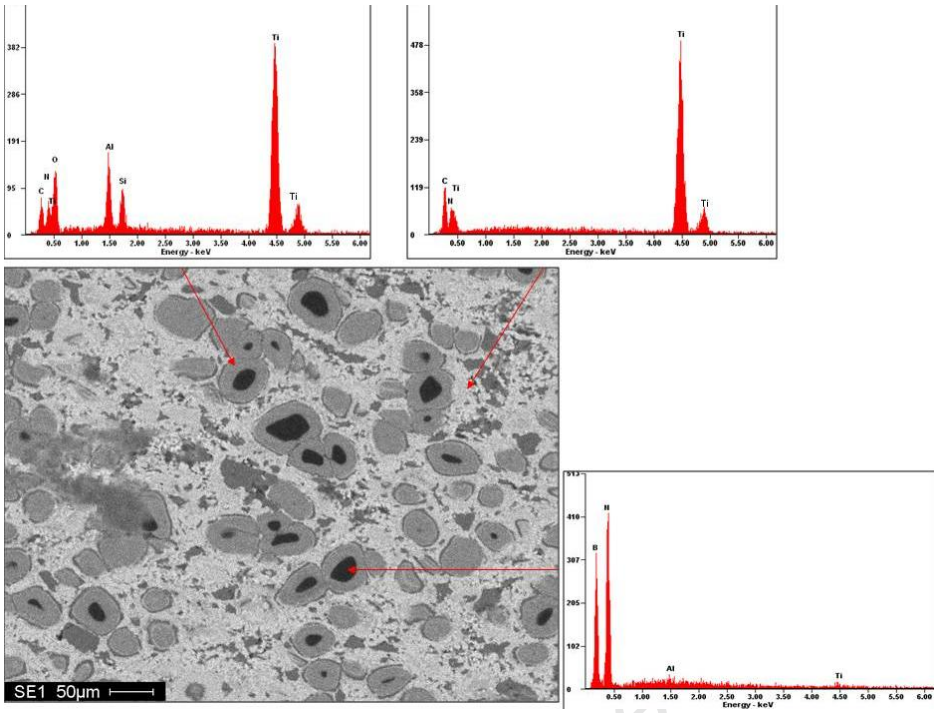

Figure 4. 37: EDS secondary electron (SE) image analysis of Ti_3SiC_2/c-BN composite.

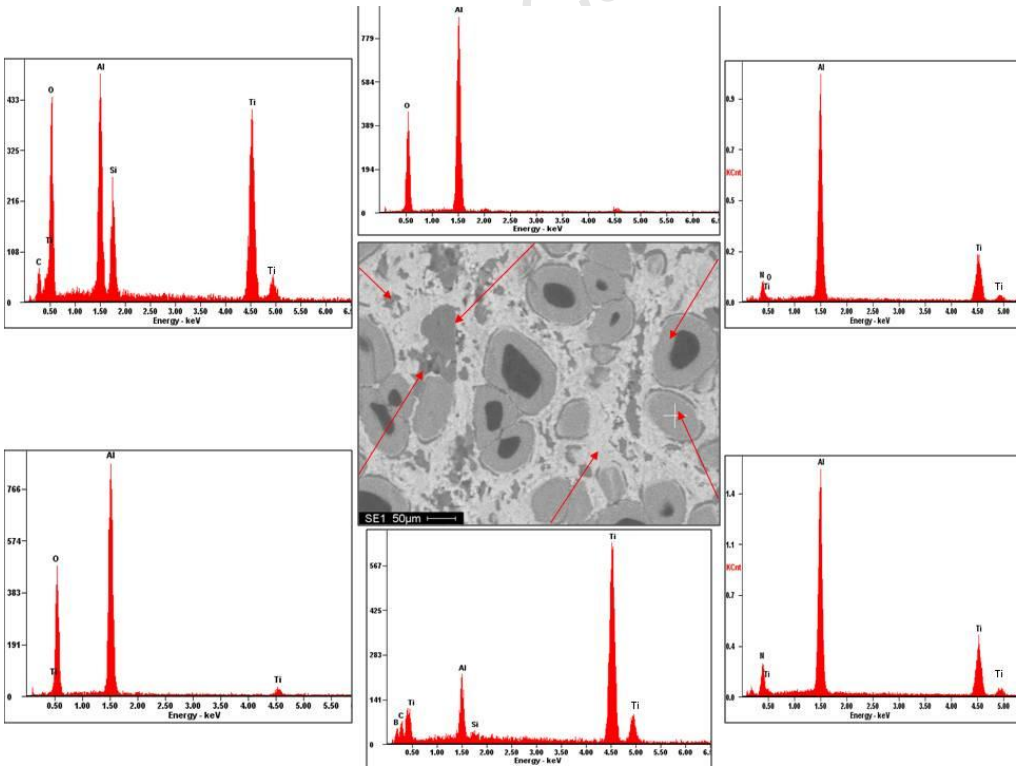

Figure 4. 38: EDS secondary electron (SE) image analysis of Ti_3SiC_2/c-BN composite at higher magnification.

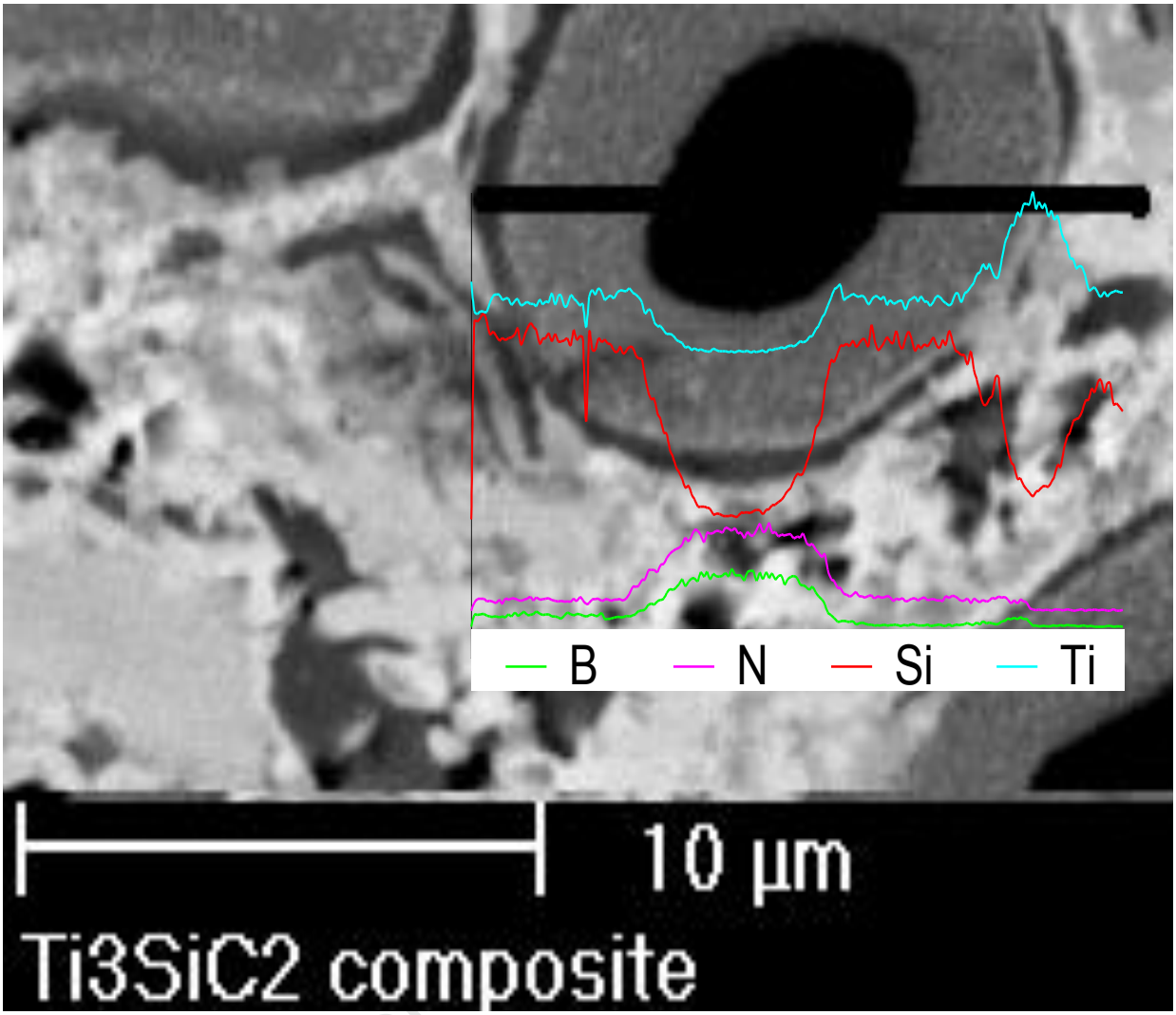

Figure 4. 39: Enlarged SE image with EDS line scan of the Ti_3SiC_2/c-BN composite sintered at 1400°C, 30 minute and 10MPa pressure.

Figure 4.39 shows the EDS line scan of the Ti_3SiC_2/c-BN reaction area around the c-BN: B and N increase near the c-BN phase and peak across the c-BN phase, decreasing again in the interfacial region and levelling off across the MAX phase matrix. The Ti and Si phases do the opposite. There is a Ti spike and a Si drop as the line touches the outside of the reaction area (the dark grey lining). The presence of Si, Ti, B and N in the reaction region around the c-BN shows that the two materials reacted at these conditions as predicted by the reaction couples in section 4.3.2, the reaction region however seems to be thicker than desired

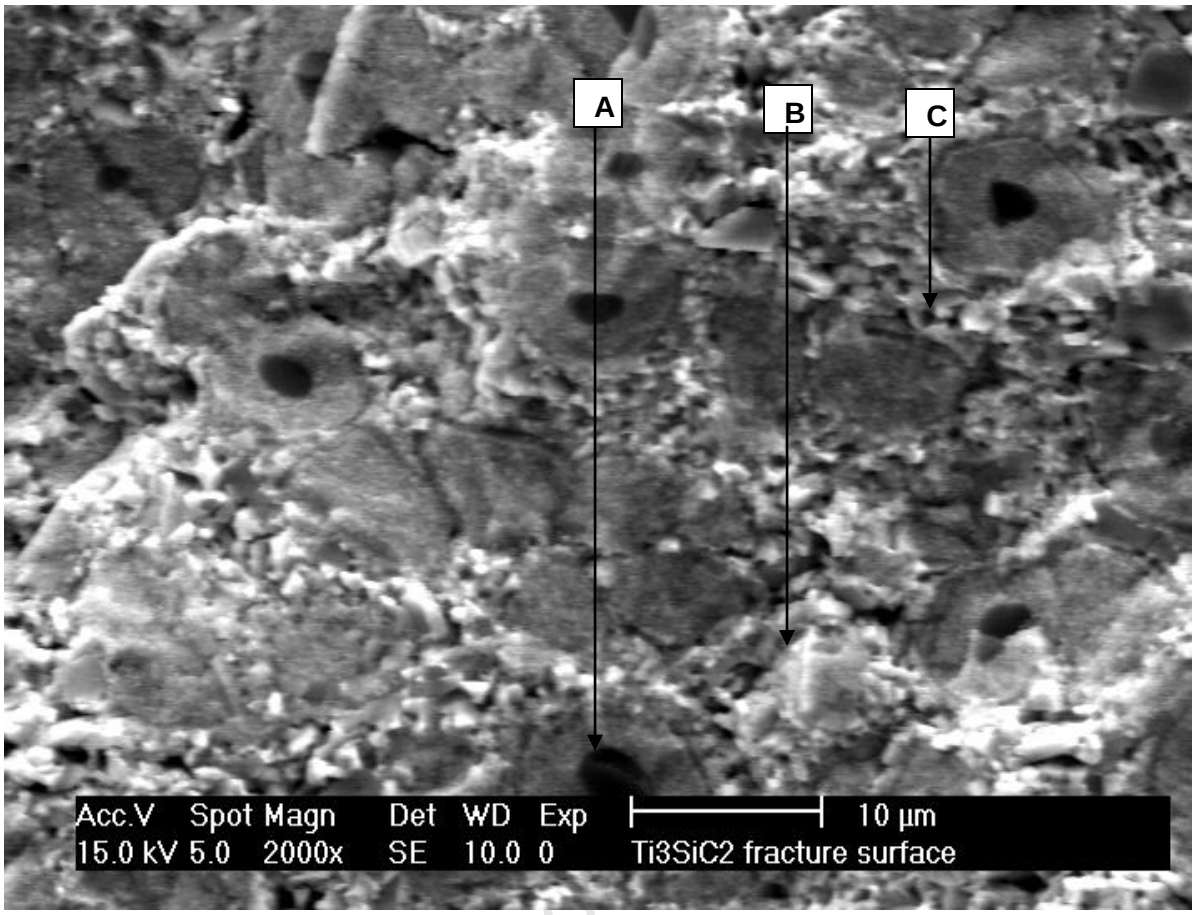

Figure 4. 40: SEM SE image of Ti_3SiC_2/c-BN composite fracture surface sintered at 10MPa, 1400°C for 30 minutes.

Figure 4.40 shows the fracture surface of a Ti_3SiC_2/c-BN composite. Three types of microstructural region may be observed: c-BN without a reaction region on the exposed surface (A); c-BN with a reaction region still around it (B); Ti_2AlC and a surrounding matrix (C). The fracture therefore appears to have stripped some c-BN particles of the reaction region rim (A), and elsewhere to have been deflected around the rim (B).

CHAPTER FIVE:
DISCUSSION

5.1 Powder preparation

Milling all three powder combinations (for synthesising Ti_2AlC, Ti_3AlC_2 and Ti_3SiC_2) at 300 rpm for 6 hours facilitated the homogeneous dispersion of each elemental powder in the mixture with negligible agglomeration, as shown in figure 5.1. Milling at these conditions did not cause any reaction between the powders used, and no new phases were formed as seen in figures 4.2, 4.4 and 4.6. The oxygen in the carbon-containing regions may be due to the trapping of oxygen by the organic-based resin during curing. The utilisation of hexane was successful in facilitating the dispersion of the powder; and in preventing both the oxidation of the metal powders and the combustion of the activated carbon during milling.

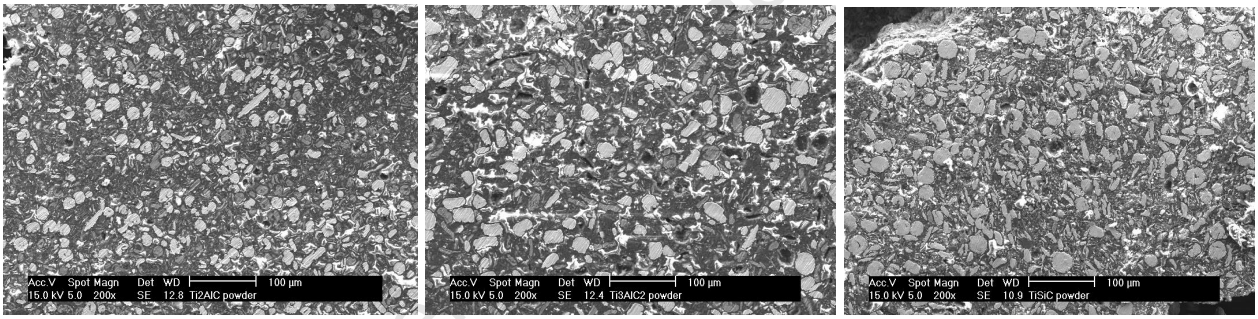

Figure 5. 1: Image of mixed powders used to synthesise (from left to right) Ti_2AlC, Ti_3AlC_2 and Ti_3SiC_2.

Use of alumina milling balls might have caused the deformation of some Ti particles, and almost all the Al particles, in all powder combinations: as we can see some are elongated (deformed) and some are round. The smaller particle size of the powders used to synthesise Ti_2AlC (relative to the other two powder combinations, as seen in figure 5.1) is more marked than the difference between the other two powder combinations. This difference probably arises from the small amount of powder that was milled for Ti_2AlC: as seen in Table 3.2 the total amount of powder is 13.465g (Ti_2AlC), 19.465g (Ti_3AlC_2) and 19.564g (Ti_3SiC_2). The same number of alumina balls and processing was used for milling the three powder mixtures; therefore it is not clear at this time why the Ti_3AlC_2 powder mixture is twice the size of the other mixtures.

5.2 MAX phases

5.2.1 Ti_2AlC

The composition of the sintered products formed by different time/temperature profiles is shown in figure 5.2. These results are not consistent with the results of Zhu *et al.* [53], who reported that fully dense, single phase Ti_2AlC could be synthesised by hot pressing at 1300°C for 1 hour. Zhu *et al*. [53] further reported that increasing the temperature to 1350°C resulted in the formation of some Ti_3AlC_2, which was not observed in the present work. Increasing the temperature, as shown in figure 5.2, resulted in an increase of the Ti_2AlC phase instead of the formation of the Ti_3AlC_2, and a decrease (but not elimination) of the TiC phase. The presence of TiC after sintering could be due to the evaporation of the Al at elevated temperatures or oxidation of Al since there is Al_2O_3 on the products.

In the present work, no reactions were observed between elemental powders after milling (sections 4.1 and 5.1). Zhu *et al.* [53], who used a planetary ball mill at 1000rpm, suggested that $TiAl_3$ intermetallics and TiC were formed by Ti, C and Al during high-energy milling. These pre-existing phases may account for the formation of MAX phases during sintering at lower temperatures in Zhu *et al*.'s work, since some of the intermediate phases were already present.

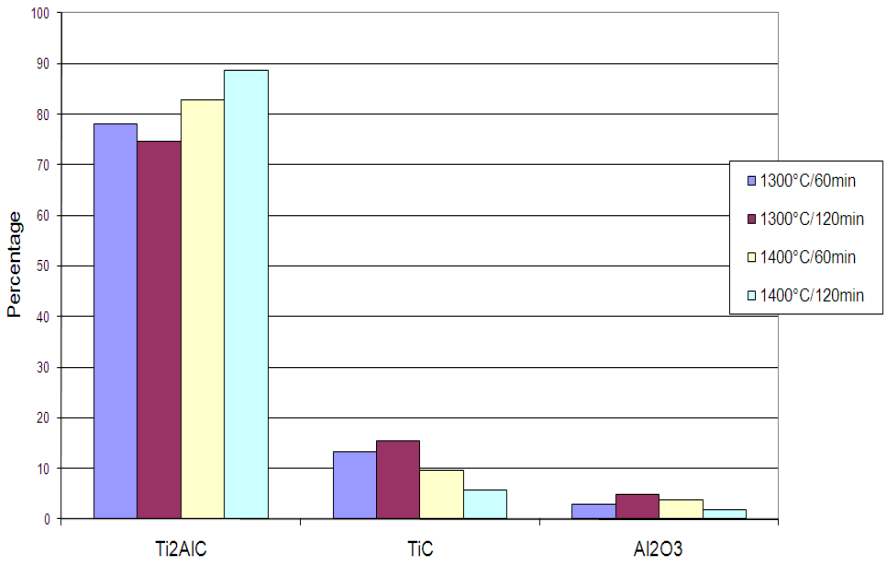

Figure 5. 2: A summary of the products formed during the sintering of Ti_2AlC at different time/temperature profiles.

5.2.2 Ti_3AlC_2

Peng [56] reported that fully dense and nearly pure Ti_3AlC_2 bulk ceramic with minor TiC as an impurity could be synthesised from Ti, Al and graphite by hot pressing at 1400°C for 2 hours. Using these conditions in this case did not yield the same results, as shown in figure 5.3. The TiC presence may, again, be due to the evaporation of the Al at elevated temperatures as Peng [56] also reported. Increasing the temperature results in an increase of the Ti_2AlC phase and also increases the formation of the Ti_3AlC_2 and a decrease of the TiC phase, but not a complete elimination of TiC. Increasing the temperature from 1300°C to 1400°C increases the Ti_3AlC_2 phase, but increasing the time from 60 minutes to 120 minutes causes a decrease in the Ti_3AlC_2 phase. Therefore, a higher temperature, for instance 1500°C, and shorter time, 30 minutes or less, might be more favourable conditions for the formation of the Ti_3AlC_2 phase, by driving the reaction $Ti_2AlC + TiC \rightarrow Ti_3AlC_2$, and limiting the time for the reverse to occur. A possible reason why it may be possible to make this MAX phase at 1000°C more than that reported by Peng [56] might be the same as why it we were able to make Ti_2AlC at a 1000°C more than Zhu *et al.* [53] as reported in section 5.2.1

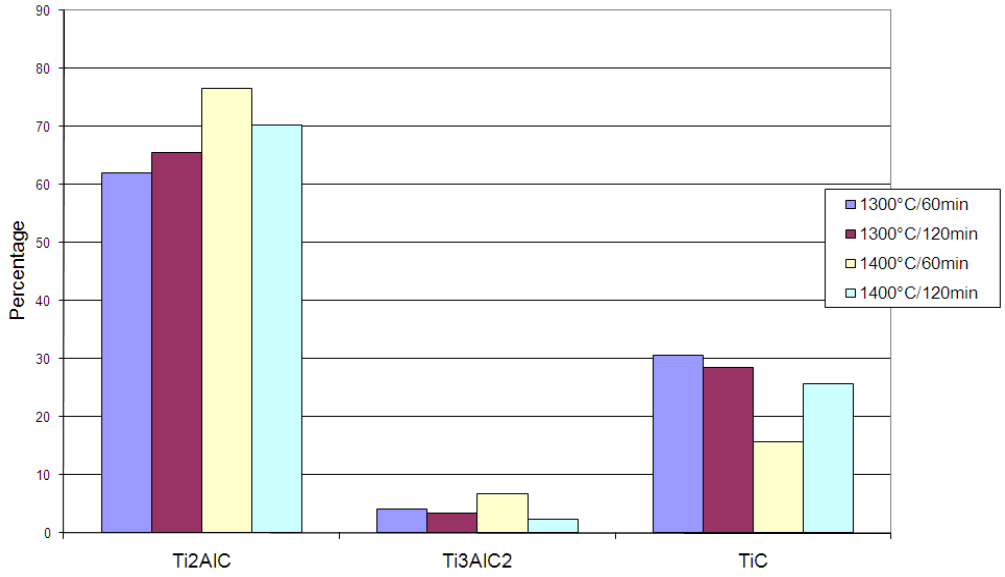

Figure 5. 3: A summary of the products formed during the sintering of Ti_3AlC_2 at different time/temperature profiles.

5.2.3 Ti_3SiC_2

Tang *et al.* [53] reported that fully dense and single phase Ti_3SiC_2 bulk ceramic could be synthesised from Ti, SiC and graphite by hot pressing at 1500°C for 2 hours. Tang *et al*. [53] further reported that before the temperature reaches 1480 °C, there is no liquid phase, and only some 'secondary reaction' (i.e. not the reaction to form Ti_3SiC_2) takes place. This was not observed in the present work, as shown in figure 5.4. Tang *et al.* [53] further reported that when the temperature is less than 1400°C formation of TiC, $Ti_5Si_3C_x$ and other phases can occur, which was observed here for the first two phases where x = 0 (i.e. $Ti_5Si_3C_x$ becomes Ti_5Si_3). The presence of TiC this case could be due to the phase field of Ti_3SiC_2 being very narrow: a second phase (mainly TiC particles) commonly co-exists with Ti_3SiC_2 as explained by Tang *et al.* [62]. The presence of SiC could result from non-reacted SiC from the staring powders; this could be eliminated by reacting at higher temperatures for reaction of all the powders.

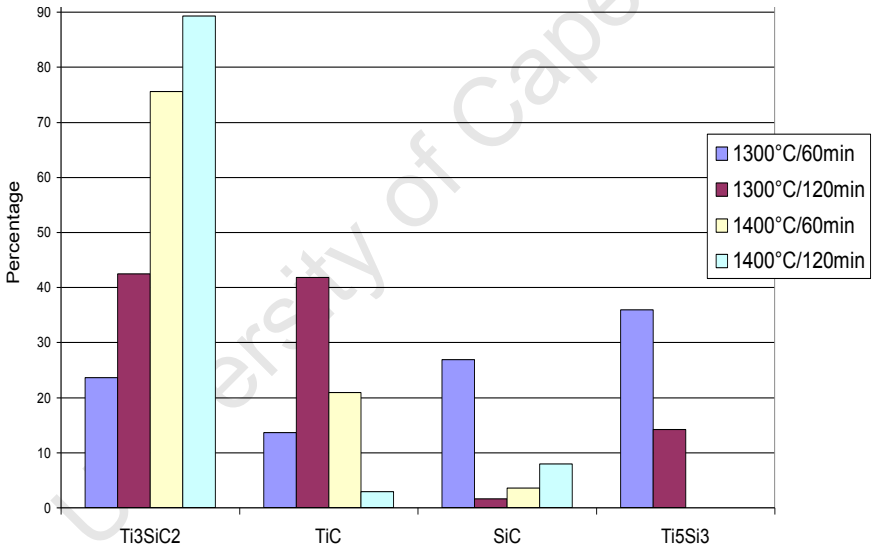

Figure 5. 4: A summary of the products formed during the sintering of Ti_3SiC_2 at different time/temperature profiles.

The fracture surfaces of all MAX phases synthesised here reveal layered structures, as also reported in the literature [56,57,59]. Also seen in the images (figs 4.9, 4.13 and 4.17) are some planar regions which were also observed by Peng [56], who reported them to be MAX phases. The densities of the MAX phases synthesised at different time and temperature profiles are smilingly dependent on the time or temperature (Table 4.1). The highest density is for Ti_2AlC at 99.16% of the theoretical density, then 98.21% for the Ti_3SiC_2 and lastly 89.78% for the Ti_3AlC_2.

The lower density for the Ti_3AlC_2 is due to presence of the Ti_2AlC phase, which is the dominant phase here given the fact that the majority of the phase formed during synthesis for Ti_3AlC_2 was Ti_2AlC; this means the densification is higher than the tabulated values. This is because the tabulated values are calculated in relation to Ti_3AlC_2. If this were corrected by using the fact that the sample is majority Ti_2AlC then the density could be at least 95%. This is supported by the tabulated porosity. Therefore densification is not the biggest challenge in this work but the phase formation, especially for Ti_3AlC_2. Overall, only the results obtained for Ti_2AlC and Ti_3SiC_2 were satisfactory to use the samples for further experiments with c-BN.

5.3 Reaction couples

5.3.1 Ti_2AlC/c-BN couple

Reacting Ti_2AlC and c-BN at 1400°C for 30 minutes resulted in a reaction between the two materials. The pores between MAX phase and the reaction area, seen in figure 5.5 (left), could have been caused by the difference in the densities of the phases present: the denser materials are expected to contract more during cooling than the less dense materials. In this case it is observed that the reaction area is pulling away from the MAX phase, suggesting that the interfacial phases are higher in density than the MAX phase and similar in density to the c-BN. There is, however, good bonding of the c-BN and the interfacial phases, and good bonding between the MAX phase and the interfacial phases (where there is contact).

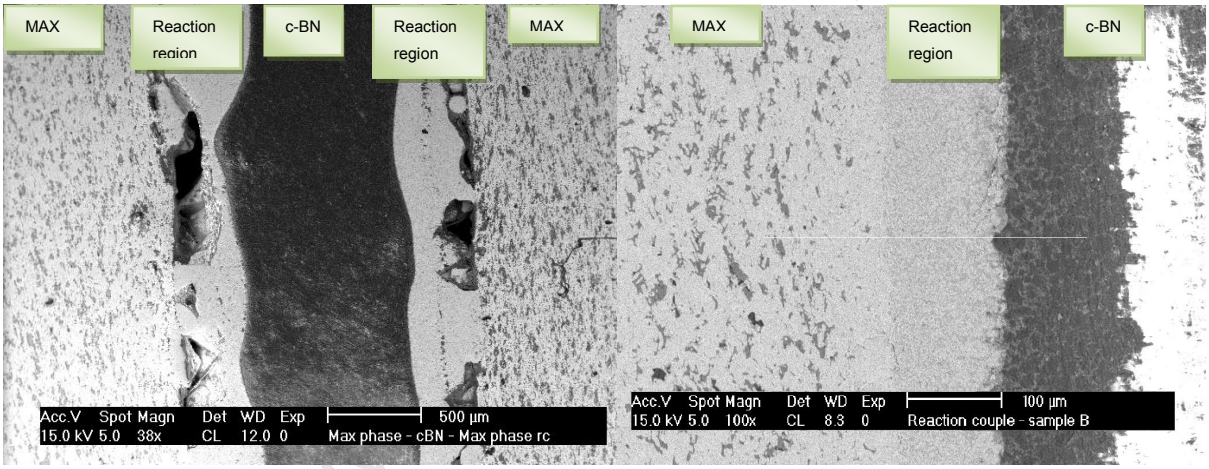

Figure 5. 5: Images of the reaction couple Ti_2AlC/c-BN reacted at 1500°C, 30 minutes and ambient pressure (left) and 1500°C, 30 minute and 10MPa pressure (right).

The line scan of this reaction couple (fig 4.20) shows that there is B, N, Ti, Al, and C in the interfacial region and the point scan of the interface shows some phases such as TiAl, TiC and TiB_2. The XRD results confirm this, showing that in addition to the original phases (TiC, Al_2O_3-MAX; and c-BN, AlN-c-BN) there are also TiB_2 and TiN phases present. Some TiC and AlN are also possible products from the reacting of the two materials. The scan also shows the presence of Ti_3AlC_2 instead of Ti_2AlC, indicating a transformation of the Ti_2AlC. A partial transformation of Ti_2AlC to Ti_3AlC_2 was also reported to occur at 1350°C by Zhu *et al.* [53].

Applying a 10MPa pressure eliminates the contraction of the reaction region away from the MAX phase, by forcing the two together until room temperature is reached (figure 5.5). In this case also, the line scan of this reaction couple shows that there is B, N, TI, Al, and C in the interface; the point scan of the interface however shows some phases such as TiAl, TiC, TiN, SiC and TiB_2. The XRD results confirm this for phases such as TiC, TiN and TiB_2. TiAl and SiC are not seen in this case; the SiC seen before could have been a contamination from the SiC grinding paper when preparing that sample. The scan also shows a presence of Ti_3AlC_2 instead of Ti_2AlC resulting from a non-desired transformation of the Ti_2AlC.

The transformation of the Ti_2AlC to Ti_3AlC_2 in both reaction couples supports the postulate that synthesising the latter at 1500°C and 30 minutes would result in a much better Ti_3AlC_2 phase presence in the synthesis of this phase, as stated in section 5.2.2.

5.3.2 Ti_3SiC_2/c-BN couple

The heating of this couple to 1500°C resulted in the partial decomposition of the MAX phase, as the XRD scan shows some Ti_3SiC_2 still present even though the surface appears to have decomposed. The apparent transformation of the c-BN to h-BN, inferred from the dimensional change, is not confirmed by the XRD results (figure 4.28, 4.30), and could simply be a dimensional change arising from the conditions the sample was subjected to. The c-BN and Ti_3SiC_2 samples did not react at 1500°C and ambient pressure: instead of a reaction, only a decomposition of the MAX phase occurred, which could have hindered the reaction process (figure 5.6). Barsoum [4] reported that the decomposition temperature is a function of many variables, the most important of which is oxygen contamination and/or other impurities, which could account for the decomposition of the Ti_3SiC_2 phase at this temperature.

Lowering the temperature to 1400°C and application of 10MPa pressure promotes the reaction of the MAX phase with c-BN rather than the decomposition of the MAX phase (figure 5.6). This is confirmed by the line scan of this reaction couple which shows that there is B, N, Ti, Si, and C in the interface; the point scan of the interface shows some phases such as TiN, $TiSi_2$ and TiB_2. The XRD results confirm this for some phases such as TiB_2 and TiN but it does not show the additional TiS_2.

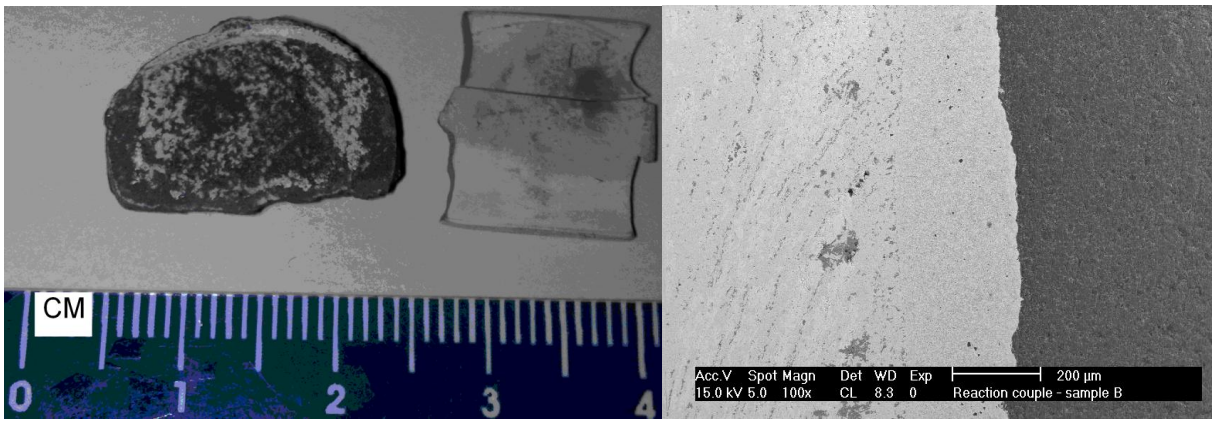

Figure 5. 6: Image of the reaction site of the samples Ti_3SiC_2/c-BN reacted at 1500°C, 30 minutes, ambient pressure (left) and the reaction couple reacted at 1400°C, 30 minutes and 10 MPa pressure (right).

Overall the two MAX phases Ti_2AlC and Ti_3SiC_2 can be successfully reacted with c-BN at 1500°C and 1400°C respectively, and 10MPa pressure for 30 minutes. The observed transformation of the Ti_2AlC phase under these conditions is not optimal; nevertheless these conditions were selected for reaction of the two materials to make a composite.

5.4 Composites

The crushing of the MAX phase samples to make MAX phase powder was a high-energy process which resulted in a high contamination of alumina in the powders (and ultimately in the composite). The subsequent mixing of c-BN and MAX phase powders for synthesis of a composite yielded relatively good mixing, although not as homogeneous as is necessary for high quality composite. This can be solved by increasing the mixing time by about 2 hours in order to promote mixing.

5.4.1 Ti_2AlC/c-BN composite

As predicted by reaction couples sintered at selected temperature-pressure profiles, the TI_2AlC/c-BN composite was successfully synthesised, although the interface was thicker than expected (about 2 μm). The secondary phases obtained here were TiAl, TiB_2, TiC and AlN. Benko *et al.* [63] synthesised composites of c-BN using TiC and c-BN powders instead of Ti_2AlC and c-BN powders (vol.% of TiC:c-BN as 50:50 instead of 80:20 in the present work, and at 7 GPa and 1750°C instead of at 10MPa and 1500°C). The obtained secondary phases in this case were TiB_2 as seen also in the present work, and $TiC_{0.8}N_{0.2}$ instead of TiC. Rong *et al.* synthesised composites of c-BN using TIN, Al and c-BN powders instead of Ti_2AlC and c-BN powders (vol.% of Al:TiN:c-BN as 12:13:75 instead of 80:20, and at 30.7 GPa and 1400°C instead of at 10MPa and 1500°C). The obtained secondary phases in this case were TiB_2 and AlN as seen in the present work.

Fractography showed that the c-BN particles in the MAX phase deflect cracks, which is expected to improve the toughness of the material. The interface is bonded well with both the c-BN and the MAX phase, as observed from the crack, which is observed to travel around the c-BN interface region and also through the interface but around the c-BN. There is also some crack deflection around some MAX phase grains as shown in figure 5.7.

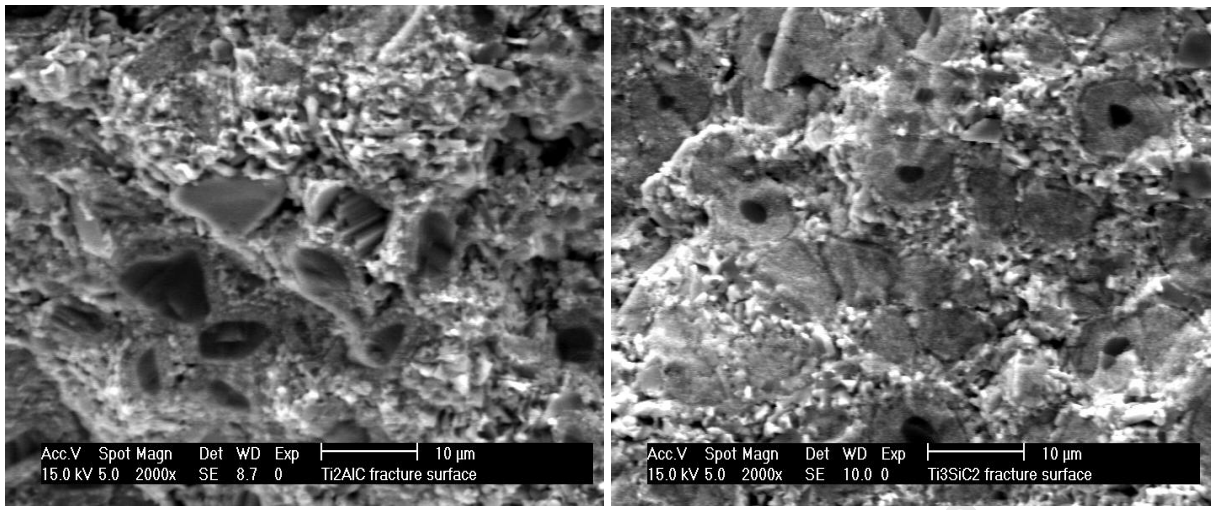

Figure 5. 7: Images of Ti_2AlC/c-BN (left) and Ti_3SiC_2/c-BN (right) composite fracture surfaces.

5.4.2 Ti_3SiC_2/c-BN composite

As predicted by reaction couples at selected temperature-pressure profiles, the TI_3SiC_2/c-BN composite was successfully synthesised, although the interface region was thicker than expected (about 3 µm). The secondary phases obtained here were TiN, TiB_2, TiC and TiS_2. Benko *et al.* [60] synthesised the same composites of c-BN using Ti_3SiC_2 and c-BN powders (vol.% of Ti_3SiC_2:c-BN as 75:25 instead of 80:20, and at 7 GPa and 1750°C instead of at 10MPa and 1500°C). The obtained secondary phases in this case were TiC, SiC and TiB_2 as seen with our experiments and SiB_4 and SiC instead of $TiSi_2$ and TiN as seen in figure 5.8.

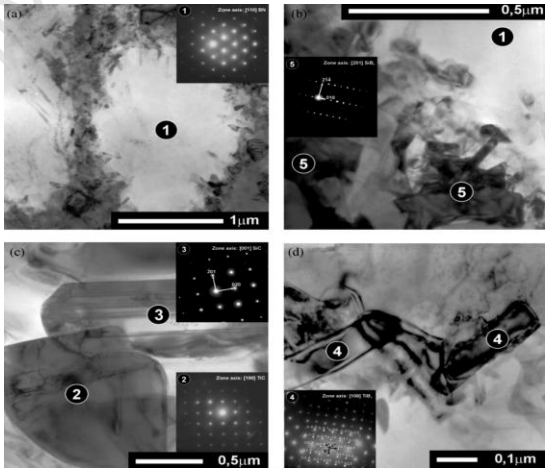

Figure 5. 8: Microstructure of c-BN sintered with Ti_3SiC_2 and Electron diffractions characteristics for phases present. (1) c-BN, (2) TiC, (3) SiC, (4) TiB_2 and (5) SiB_4. (After Benko *et al.* [60]).

As observed for the Ti_2AlC composite, the c-BN particles in the MAX phase cause a crack to be deflected around it; this is expected to result in a tougher material. The interface is bonded well with the c-BN and with the MAX phase, illustrated by crack propagation around the c-BN interface region and also through the interface but around the c-BN. There is also some crack deflection around some MAX phase grains as shown in figure 5.7.

\

CHAPTER SIX:
CONCLUSIONS AND RECOMMENDATIONS

From the discussion of the results obtained in these experiments, the following were concluded:

1. Samples of Ti_2AlC and Ti_3SiC_2 with little TiC present can be successfully synthesised with high densities, 99.16% and 98.21%, respectively, of the theoretical density.
2. MAX/c-BN composites can be synthesised using 10MPa, 30 minutes and 1500°C (TI_2AlC) or 1400°C (Ti_3SiC_2), both can react at these conditions and still remain intact.
3. Ti_2AlC and Ti_3SiC_2 are fully compatible with c-BN for synthesis of a composite. Improved properties, such as toughness, are predicted for the respective composites.

The following recommendations were therefore made:

1. Sintering of MAX phases: investigate increasing the molar ratio of Al to the other powders, by about 0.2, to facilitate the preservation of the Al even after some evaporates to improve the purity of the samples.
2. Sinter the composite MAX phase/c-BN s for longer at lower temperature in order to achieve some reaction, but a thinner interface.
3. MAX phase/c-BN composites are promising materials. Their properties should be investigated for industrial applications which need a material of high fracture toughness, high temperatures and high pressure applications.

REFERENCES

1 D. Akyuz and T. El-Raghy, *Tools for cutting solid materials United States Patent application Publication*, US2003/186636 A1, United states of America, 2003.

2 L. Vel, G. Demazeau and J. Etourneau, *Mat. Sci. Eng.,* 1991, **B10**, 149-164 (DOI:10.1016/0921-5107(91)90121-B).

3 ECVV Co., Ltd. *Zhecheng Hongxiang Superhard Material Co., Ltd. Diamond Drill Bit and Diamond Grinding Wheel Manufacturer from China.* 2011.

4 M. W. Barsoum, in *Encyclopedia of Materials: Science and Technology*, ed. K. H. Jürgen Buschow, R. W. Cahn, M. C. Flemings, B. (. Ilschner, E. J. Kramer, S. Mahajan and P. Veyssière), Elsevier, Oxford, 2006, p. 1-11.

5 L. Farber and M. W. Barsoum, *J. Mater. Res.*, 1999, **14**, 2560-2566 (DOI: 10.1557/JMR.1999.0343)

6 Y. Du, J. Schuster, H. Seifert and F. Aldinger, *J. Am. Ceram. Soc.,* 2000, **83**, 197-203 (DOI:10.1111/j.1151-2916.2000.tb01170.x).

7 W. Jeitschko and H. Nowotny, *Monatschrift für Chemie/chemical monthly,* 1967, **98**, 329-337 (DOI:10.1007/BF00899949).

8 J. J. Nickl, K. K. Schweitzer and P. Luxenberg, *J. Less Common Metals,* 1972, **26**, 335-353 (DOI:10.1016/0022-5088(72)90083-5).

9 R. Pampuch, J. Lis, L. Stobierski and M. Tymkiewicz, *J. Eur. Ceram. Soc.,* 1989, **5**, 283-287 (DOI:10.1016/0955-2219(89)90022-8).

10 M. W. Barsoum and T. El-Raghy, *Am. Sci.,* 2001, **89**, 334-343 (DOI:10.1511/2001.4.334).

11 I. Kero, Licentiate thesis, Luleå University of Technology, 2007.

12 L. Farber, M. W. Barsoum, A. Zavaliangos, T. El-Raghy and I. Levin, *J. Amer. Cer. Soc.,* 1998, **81**, 1677-1681 (DOI:10.1111/j.1151-2916.1998.tb02532.x).

13 M. W. Barsoum, L. Farber and T. El-Raghy, *Met. Mater. Trans.,* 1999, **30A**, 1727-1738 (DOI:10.1007/s11661-999-0172-z).

14 L. Farber, *Phil. Mag. Lett.,* 1999, **79**, 163-170.

15 M. W. Barsoum and M. Radovic, in *Encyclopedia of Materials: Science and Technology*, ed. K. H. Jürgen Buschow, R. W. Cahn, M. C. Flemings, B. (. Ilschner, E. J. Kramer, S. Mahajan and P. Veyssière), Elsevier, Oxford, 2004, p. 1-16.

16 B. J. Kooi, R. J. Poppen, N. J. M. Carvalho, De Hosson, J. Th. M. and M. W. Barsoum, *Acta Mater.,* 2003, **51**, 2859-2872 (DOI:10.1016/S1359-6454(03)00091-0).

17 J. B. Hess and C. S. Barrett, *Trans. AIME,* 1949, **185**, 599-605.

18 R. Yu, Q. Zhang, L. L. He, Y. C. Zhou and H. Q. Ye, *Phil. Mag. Lett.,* 2003, **83**, 325-331 (DOI:10.1080/0950083031000104367).

19 M. W. Barsoum and T. El-Raghy, *Met. Mater. Trans.,* 1999, **30A**, 363-369 (DOI:10.1007/s11661-999-0325-0).

20 M. Radovic, M. W. Barsoum, T. El-Raghy and S. M. Wiederhorn, *J. Alloy. Compnds.,* 2003, **361**, 299-312 (DOI:10.1016/S0925-8388(03)00435-3).

21 N. V. Tzenov and M. W. Barsoum, *J. Amer. Cer. Soc.,* 2000, **83**, 825-832 (DOI:10.1111/j.1151-2916.2000.tb01281.x).

22 M. W. Barsoum, T. El-Raghy and M. Ali, *Met. Mater. Trans.,* 2000, **31A**, 1857-1865 (DOI:10.1007/s11661-006-0243-3)

23 M. W. Barsoum, *Prog. Solid State Chem.,* 2000, **28**, 201-281 (DOI:10.1016/S0079-6786(00)00006-6).

24 Y. Kuroda, I. M. Low, M. W. Barsoum, T. J. El-Raghy, *Aust. Ceram. Soc.*, 2001, **37**, 95-102.

25 T. Goto and T. Hirai, *Mater. Res. Bull.,* 1987, **22**, 1195-1201 (DOI: 10.1016/0025-5408(87)90128-0).

26 A. Murugaiah, M. W. Barsoum, S. R. Kalidindi and T. Zhen, *J. Mater. Res.,* 2004, **19**, 1139-11498 (DOI:10.1557/JMR.2004.0148).

27 T. El-Raghy, A. Zavaliangos, M. W. Barsoum and S. R. Kalidindi, *J. Amer. Cer. Soc.,* 1997, **80**, 513-516 (DOI:10.1111/j.1151-2916.1997.tb02861.x).

28 T. El-Raghy, M. W. Barsoum, A. Zavaliangos and S. R. Kalidindi, *J. Amer. Cer. Soc.,* 1999, **82**, 2855-2860 (DOI:10.1111/j.1151-2916.1999.tb02167.x).

29 A. T. Procopio, M. W. Barsoum and T. El-Raghy, *Met. Mater. Trans.,* 2000, **A31**, 333-337.

30 M. W. Barsoum and T. El-Raghy, *J. Am. Ceram Soc.,* 1996, **79**, 1953-1956 (DOI:10.1111/j.1151-2916.1996.tb08018.x).

31 H. 0. Pierson, *Handbook of Refractoy Carbides and Nitrides*, Noyes Publications., Westwood. NJ, 1996.

32 A. Onodera, H. Hirano, T. Yuasa, N. F. Gao and Y. Miyamoto, *Appl. Phys. Lett.,* 1999, **74**, 3782-4 (DOI:10.1063/1.124178).

33 V. Keppens, D. Mandrus, B. C. Sales, B. C. Chakoumakos, P. Dai, R. Coldea, M. B. Maple, D. A. Gajewski, E. J. Freeman and S. Bennington, *Nature,* 1998, **395**, 876-878 (DOI:10.1038/27625).

34 B. C. Sales, B. C. Chakoumakos, D. Mandrus and J. W. Sharp, *J. Solid Stale Chem.,* 1999, **146**, 528-532 (DOI:10.1006/jssc.1999.8354).

35 M. W. Barsoum, T. El-Raghy, C. J. Rawn, W. D. Porter, H. Wang, E. A. Payzant and C. R. Hubbard, *J. Phy. Chem. Solids,* 1999, **60**, 429-439 (DOI:10.1016/S0022-3697(98)00313-8).

36 M. W. Barsoum, C. J. Rawn, T. El-Raghy, A. T. Procopio, W. D. Porter, H. Wang and C. R. Hubbard , *J. Appl. Phys.,* 2000, **87**, 8407-8414 (DOI:10.1063/1.373555).

37 T. El-Raghy, S. Chakraborty and M. W. Barsoum, *J. Eur. Ceram. Soc.,* 2000, **20**, 2619-2625 (DOI:10.1016/S0955-2219(00)00127-8).

38 B. Manoun, H. P. Liermann, R. P. Gulve, S. K. Saxena, A. Ganguly, M. W. Barsoum and C. S. Zha, *Appl. Phys. Left.,* 2004, **84**, 2799-2801 (DOI:10.1063/1.1699477).

39 B. Manoun, S. K. Saxena, R. Gulve, H. P. Liermann, E. L. Hoffman, M. W. Barsoum, S. Zha and G. Hug, *Appl. Phys. Lett.,* 2004, **85**, 1514-1516 (DOI:10.1063/1.1784516).

40 Z. Oo, I. M. Low and B. H. O'Connor, *Physica,* 2006, **B385-386**, 499-501 (DOI:10.1016/j.physb.2006.05.255).

41 N. Tzenov, M. W. Barsoum and T. El-Raghy, *J. Eur. Ceram. Soc.,* 2000, **20**, 801-806 (DOI:10.1016/S0955-2219(99)00166-1).

42 T. El-Raghy and M. W. Barsoum, *J. Appl. Phys.,* 1998, **83**, 112-119 (DOI:10.1063/1.366707).

43 M. W. Barsoum, T. El-Raghy, L. Farber, M. Amer, R. Christini and A. Adams, *J. Electrochem. Soc.,* 1999, **146**, 3919-3923 (DOI: 10.1149/1.1392573).

44 T. El-Raghy, M. W. Barsoum and M. Sika, *Mater. Sci. Eng.,* 2001, **A298**, 174-178 (DOI:10.1016/S0921-5093(00)01281-8).

45 M. W. Barsoum, J. Golczewski, H. J. Siefert and F. Aldinger, *J . Alloys. Compd.,* 2002, **340**, 173-179 (DOI:10.1016/S0925-8388(02)00107-X).

46 M. W. Barsoum, T. El-Raghy and L. Ogbuji, *J. Electrochem. Soc.,* 1997, **144**, 2508-2516 (DOI:35400006805510.0560).

47 M. W. Barsoum, L. H. Ho-Duc, M. Radovic and T. El-Raghy, *J. Electrochem. Soc.,* 2003, **150**, B166-B175 (DOI:4925, 35400006403357.0530).

48 M. Sundberg, G. Malmqvist, A. Magnusson and T. El-Raghy, *Ceram. Int.,* 2004, **30**, 1899-1904 (DOI:10.1016/j.ceramint.2003.12.046).

49 S. Chakraborty, T. El-Raghy and M. W. Barsoum, *Oxid. Metals.,* 2003, **59**, 83-96 (DOI:10.1023/A:1023018032160).

50 M. W. Barsoum, *J. Electrochem. Soc.,* 2001, **148**, C544-C550 (DOI:10.1149/1.1380255).

51 M. W. Barsoum, N. Tzenov, A. Procopio, T. El-Raghy and M. Ali, *J. Electrochem. Soc.,* 2001, **148**, C551-C562 (DOI:10.1149/1.1380256).

52 J. Qin, D. He, L. Lei, P. An, L. Fang, Y. Li, F. Wang and Z. Kou, *J. Alloys Compounds,* 2009, **476**, L8-L10 (DOI: 10.1016/j.jallcom.2008.09.010).

53 J. Zhu, J. Gao, J. Yang, F. Wang and K. Niihara, *Mat. Sci. Eng.,* 2008, **A490**, 62-65 (DOI:10.1016/j.msea.2008.01.017).

54 B. Manoun, F. X. Zhang, S. K. Saxena, T. El-Raghy and M. W. Barsoum, *J. Phy. Chem. Solids,* 2006, **67**, 2091-2094 (DOI: 10.1016/j.jpcs.2006.05.051).

55 M. Radovic, M. W. Barsoum, A. Ganguly, T. Zhen, P. Finkel, S. R. Kalidindi, E. Lara-Curzio, *Acta Mater,* 2006, **54,** 2757.

56 L. M. Peng, *J. Am. Ceram. Soc.,* 2007, **90**, 1312-1314 (DOI:10.1111/j.1551-2916.2007.01517.x).

57 K. Tang, C. Wang, Y. Huang, Q. Zan and X. Xu, *Mater. Sci. Eng.,* 2002, **A328**, 206-212 (DOI:10.1016/S0921-5093(01)01704-X).

58 Element six, *The Properties of Cubic Boron Nitride*, Element six, 2008.

59 W. P. Brown, *Part 6. Cubic and hexagonal boron nitride*, Dr. W. P. Brown, 2000-2011.(http://www.docbrown.info/page03/nanochem06.htm)

60 E. Benko, P. Klimczyk, S. Mackiewics, T. L. Barr and E. Piskorska, *Diamond and Related Materials,* 2004, **13**, 521-525 (DOI:10.1016/j.diamond.2003.12.029).

61 X. Rong, T. Tsurumi, O. Fukunaga and T. Yano, *Diamond and Related Materials,* 2002, **11**, 280-286 (DOI: 10.1016/S0925-9635(01)00692-6).

62 K. Tang, C. Wang, Y. Huang, X. Xu, *Journal of Alloys and Compounds,* **329,** 2001, 136 – 141 (DOI:10.1016/S0925-8388(01)01680-2)

63 E. Benko, T. L. Barr, S. Hardcastle, E. Hoppe, A. Bernasik and J. Morgiel, *Ceramics International*, **27**, 2001, 637-643 (DOI: 10.1016/S0925-9635(99)00131-4)

BIBLIOGRAPHY

M. W. Barsoum, A. Murugaiah, S. Kalidindi and T. Zhen, *Phys. Rev. Lett.,* 2004, **92**, 255508-255511 (DOI:10.1103/PhysRevLett.92.255508).

M. W. Barsoum, A. Murugaiah, S. R. Kalidindi, T. Zhen and Y. Gogotsi, *Carbon,* 2004, **42**, 1435-1445 (DOI: 10.1016/j.carbon.2003.12.090).

M. W. Barsoum, H. -. Yoo, I. K. Polushina, V. Y. . Rud, Y. V. Rud and T. El-Raghy, *Phys. Rev.,* 2000, **B62**, 10194-10198 (DOI:10.1103/PhysRevB.62.10194).

M. W. Chase Jr., *NIST-JANAF Thermochemical Tables, 4th ed*, American Chemical Society and American Institute of Physics., New York, 1998.

Y. Chen, M. Yan, Y. Sun, B. Mei and J. Zhu, *Ceram. Int.,* 2009, **35**, 1807-1812 (DOI: 10.1016/j.ceramint.2008.10.009).

G. Demazeau, G. Biardeau and L. Vel, *Mater Lett,* 1990, **10**, 139-144 (DOI: 10.1016/0167-577X(90)90048-Q).

P. Eklund, M. Beckers, U. Jansson, H. Högberg and L. Hultman, *Thin Solid Films,* 2010, **518**, 1851-1878 (DOI: 10.1016/j.tsf.2009.07.184).

A. Ganguly, T. Zhen and M. W. Barsoum, *J. Alloys Compnds.,* 2004, **376**, 287-295 (DOI:10.1016/j.jallcom.2004.01.011).

V. Gauthier-Brunet, T. Cabioc'h, P. Chartier, M. Jaouen and S. Dubois, *J. Eur. Cerem. Soc.,* 2009, **29**, 187-194 (DOI: 10.1016/j.jeurceramsoc.2008.05.039).

R. A. Guyer, K. R. McCall and G. N. Boitnott, *Phys. Rev. Lett.,* 1995, **74**, 3491-3494 (DOI:10.1103/PhysRevLett.74.3491).

J. Han, S. Hwang, D. Lee and S. Park, *J. Eur. Ceram. Soc.,* 2008, **28**, 979-988 (DOI: 10.1016/j.jeurceramsoc.2007.09.015).

G. Hug, M. Jaouen and M. W. Barsoum, *Phys. Rev.,* 2005, **B71**, 024105-024116 (DOI:10.1103/PhysRevB.71.024105).

V. D. Jovic, B. M. Jovic, S. Gupta, T. El-Raghy and M. W. Barsoum, *Corros. Sci.,* 2006, **48**, 4274-4282 (DOI: 10.1016/j.corsci.2006.04.005).

T. Kobayashi, K. Susa and S. Taniguchi, *Mater. Res. Bull.,* 1975, **10**, 1231-1235 (DOI: 10.1016/0025-5408(75)90032-X).

T. Kobayashi, *Mater. Res. Bull.,* 1979, **14**, 1541-1551 (DOI: 10.1016/0025-5408(72)90224-3).

T. Kabayama, *Method of synthesizing cubic crystal structure boron nitride*, 3,959,443, United states, 1976.

S. E. Lofland, J. D. Hettinger, K. F. Harrell P., S. Gupta, M. W. Barsoum and G. Hug, *Appl. Phys. Lett.,* 2004, **84**, 508-510 (DOI:10.1063/1.1641177).

S. B. Li, J. X. Xie, L. T. Zhang and L. F. Cheng, *Mat. Sci. Tech.,* 2005, **21**, 1054-1058 (DOI:10.1179/174328405X58841).

N. I. Medvedeva, D. L. Novikov, A. L. Ivanovsky, M. V. Kuznetsov and A. J. Freeman, *Phys. Rev.,* 1998, **B58**, 16042-16050 (DOI:10.1103/PhysRevB.58.16042).

B. Mei and Y. Miyamoto, *Mater. Chem. Phys.,* 2002, **75**, 291-295 (DOI: 10.1016/S0254-0584(02)00078-0).

R. Pampuch, J. Lis, J. Piekarczyk and L. Stobierski, *J. Mater. Synth.,* 1993, **1**, 93-94.

J. Qin, D. He, C. Chen, J. Wang, J. Hu and B. Yang, *J. Alloys Compounds,* 2008, **462**, L24-L27 (DOI: 10.1016/j.jallcom.2007.08.032).

K. Susa, T. Kobayashi and S. Taniguchi, *Mater. Res. Bull.,* 1974, **9**, 1443-1446 (DOI: 10.1016/0025-5408(74)90090-7).

G. M. Song, Y. T. Pei, W. G. Sloof, S. B. Li, De Hosson, J. Th. M. and S. van der Zwaag, *Scr. Mater.,* 2008, **58**, 13-16 (DOI: 10.1016/j.scriptamat.2007.09.006).

K. Tang, C. Wang, L. Wu, X. Guo, X. Xu and Y. Huang, *Ceram. Int.,* 2002, **28**, 761-765 (DOI:10.1016/S0272-8842(02)00040-8).

P. Wang, B. Mei, X. Hong and W. Zhou, *Trans. Nonferrous Met. Soc. China,* 2007, **17**, 1001-1004 (DOI:10.1016/S1003-6326(07)60215-5).

R. H. Wentorf, *j. Chem. Phys.,* 1957, **26**, 956 (DOI:10.1063/1.1745964).

R. H. J. Wentorf, *J. Chem. Phys.,* 1961, **34**, 809-812 (DOI:10.1063/1.1731679).
M. W. Barsoum, T. Zhen, S. R. Kalidindi, M. Radovic and A. Murugaiah, *Nature Mater.,* 2003, **2**, 107-111 (DOI:10.1038/nmat814).

X. H. Wang and Y. C. Zhou, *Corros. Sci.,* 2003, **45**, 891-907 (DOI:10.1016/S0010-938X(02)00177-4).

M. Yan, Chen, B. Mei and J. Zhu, *Trans. Nonferrous Met. Soc. China,* 2008, **18**, 82-85 (DOI:10.1016/S1003-6326(08)60015-1).

B. Zhang, Y. C. Zhou, Y. W. Bao, M. S. Li and J. Y. Wang, *J. Eur. Ceram. Soc.,* 2006, **26**, 2373-2380 (DOI:10.1016/j.jeurceramsoc.2005.04.010).

Z. F. Zhang, Z. M. Sun, H. Hashimoto and T. Abe, *J. Alloys Compounds,* 2003, **352**, 283-289 (DOI:10.1016/S0925-8388(02)01171-4).

W. Zhou, B. Mei and J. Zhu, *Ceram. Int.,* 2007, **33**, 1399-1402 (DOI:10.1016/j.ceramint.2006.04.018).

APPENDICES

XRD for MAX phase synthesis

Ti_2AlC

1300°C/60 minutes

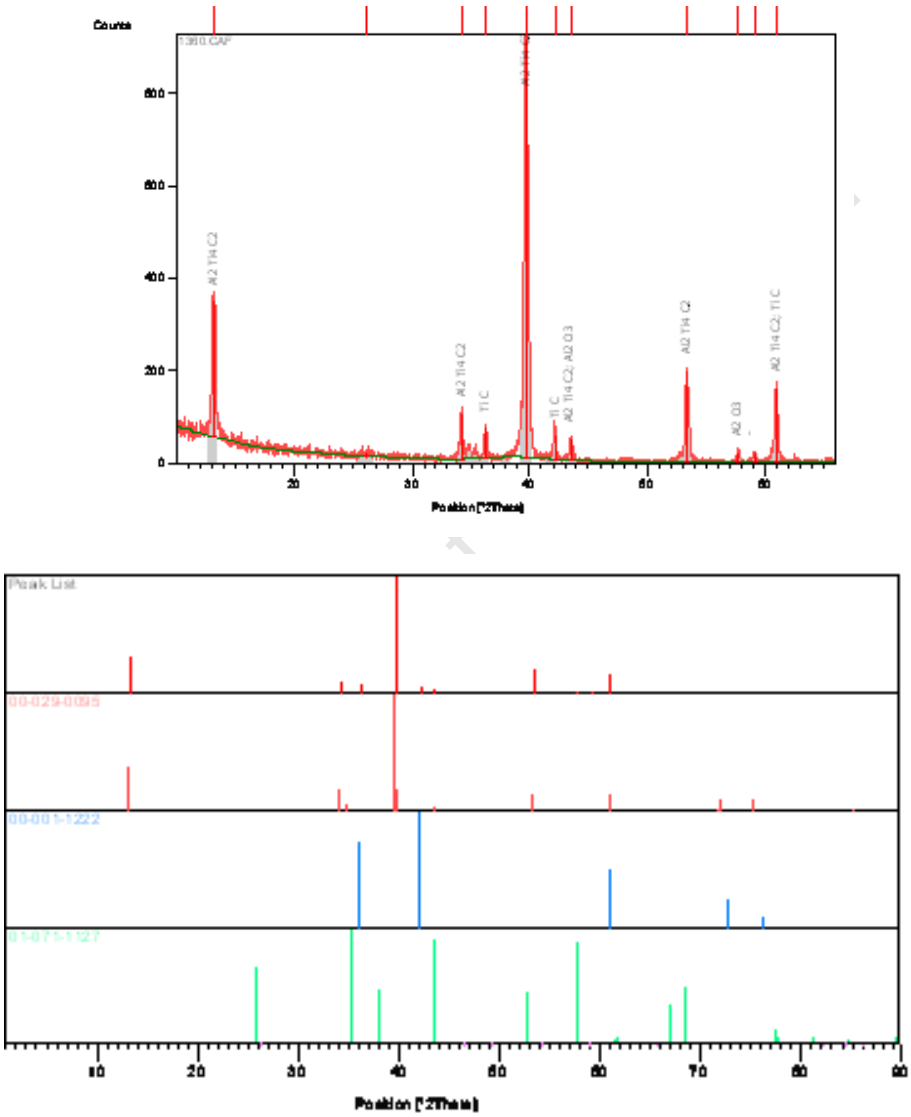

Visible	Ref. Code	Score	Compound Name	Displacement [°2Th.]	Scale Factor	Chemical Formula
*	00-029-0095	53	Titanium Aluminum Carbide	0.000	0.708	Ti_2AlC
*	00-001-1222	17	Titanium Carbide	0.000	0.076	TiC
*	01-071-1127	30	Corundum	0.000	0.033	Al_2O_3

1300°C/120 minutes

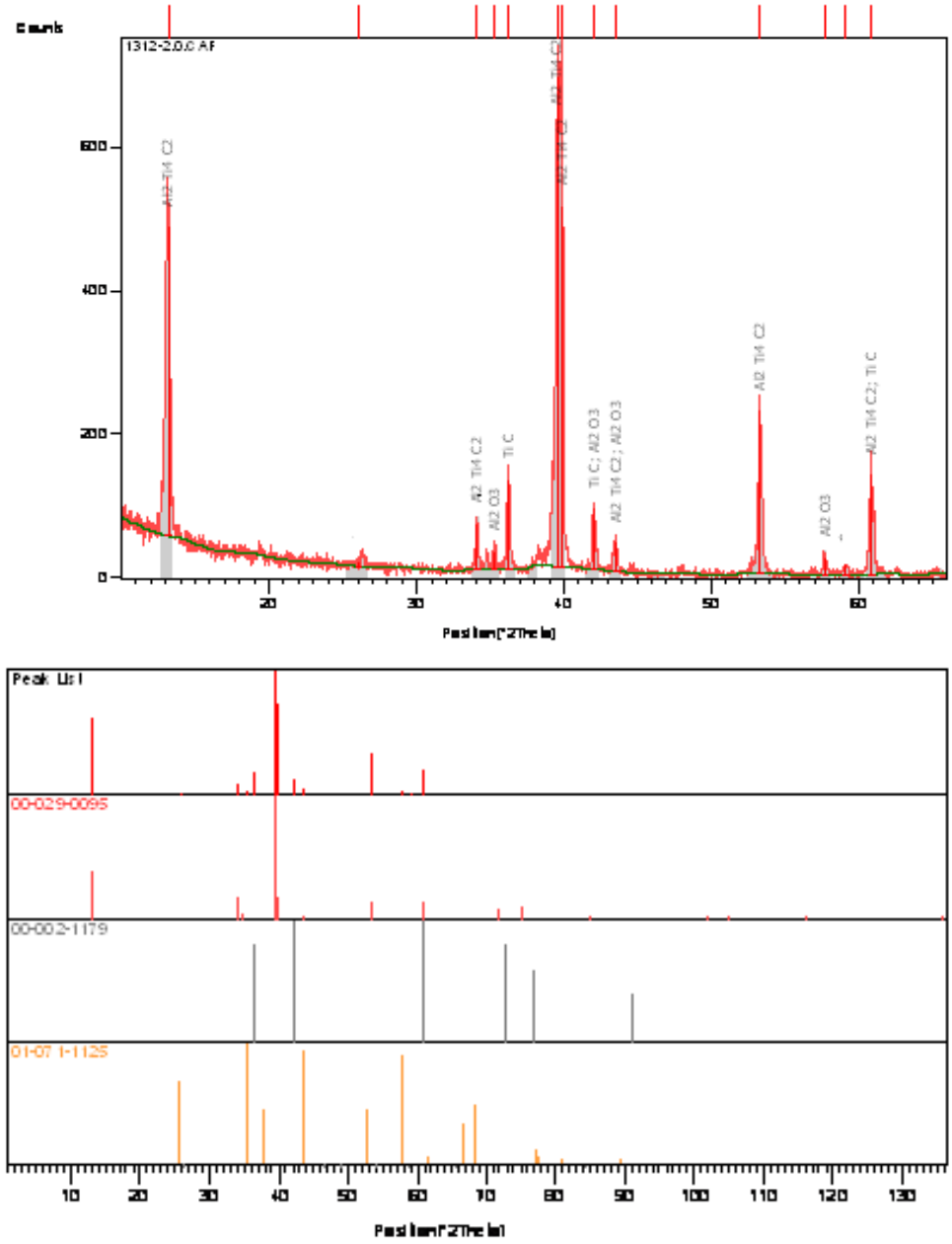

Visible	Ref. Code	Score	Compound Name	Displacement [°2Th.]	Scale Factor	Chemical Formula
*	00-029-0095	52	Titanium Aluminum Carbide	0.000	0.948	Ti_2AlC
*	00-002-1179	44	Titanium Carbide	0.000	0.132	TiC
*	01-071-1125	29	Corundum	0.000	0.047	Al_2O_3

1400°C/60 minutes

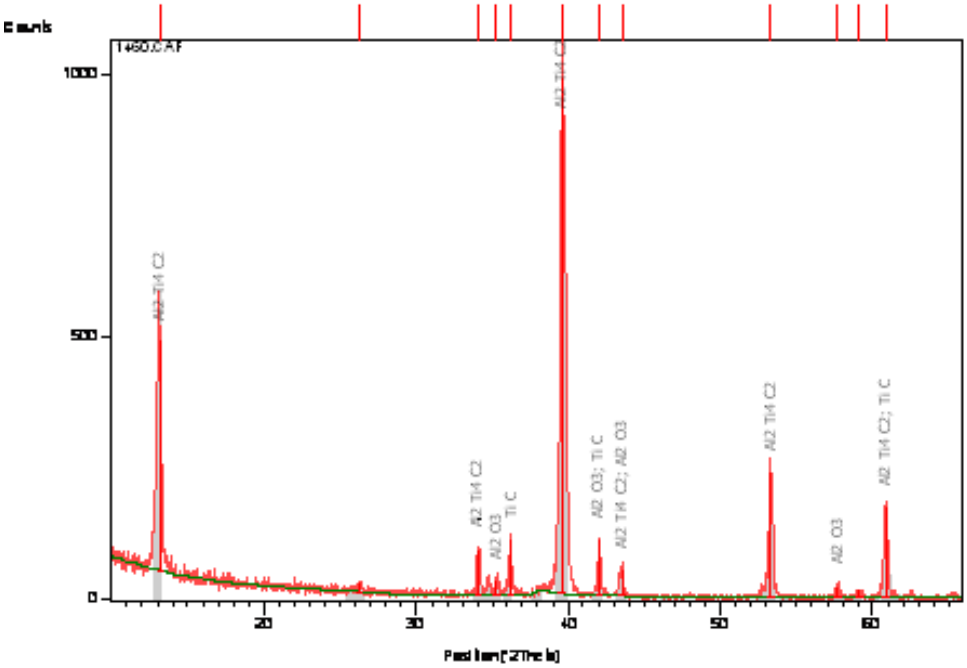

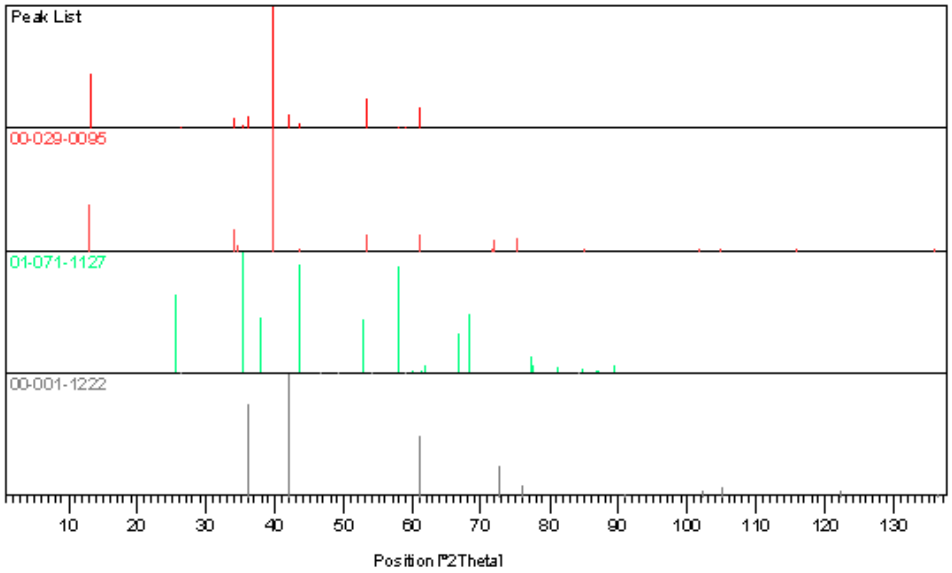

Visible	Ref. Code	Score	Compound Name	Displacement [°2Th.]	Scale Factor	Chemical Formula
*	00-029-0095	31	Titanium Aluminum Carbide	0.000	0.929	Ti_2AlC
*	01-071-1127	16	Corundum	0.000	0.031	Al_2O_3
*	00-001-1222	15	Titanium Carbide	0.000	0.091	TiC

1400°C/120 minutes

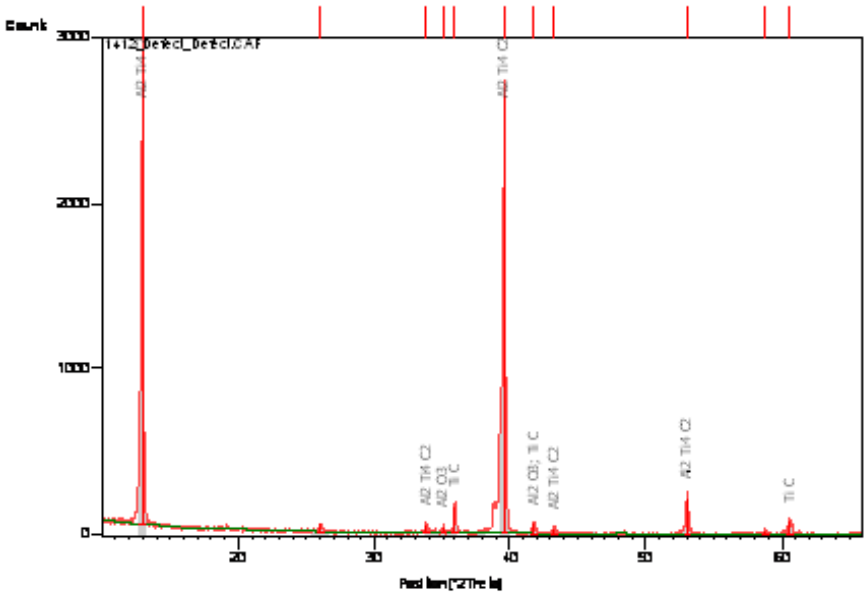

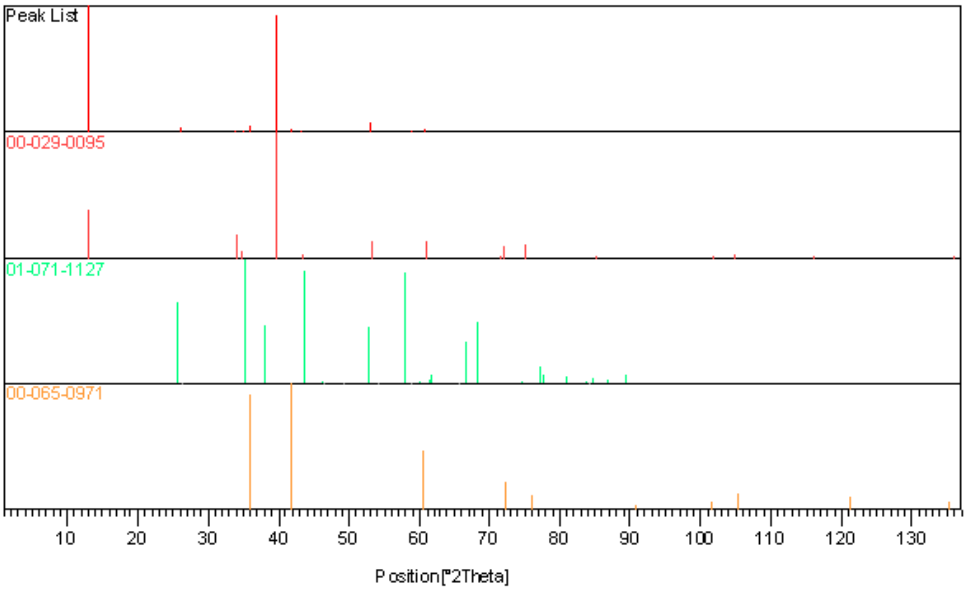

Visible	Ref. Code	Score	Compound Name	Displacement [°2Th.]	Scale Factor	Chemical Formula
*	00-029-0095	34	Titanium Aluminum Carbide	0.000	0.890	Ti_2AlC
*	01-071-1127	2	Corundum	0.000	0.021	Al_2O_3
*	01-075-0444	5	Carbon	0.000	0.005	C
*	00-065-0971	36	Titanium Carbide	0.000	0.018	TiC

Ti_3AlC_2

1300°C/60 minutes

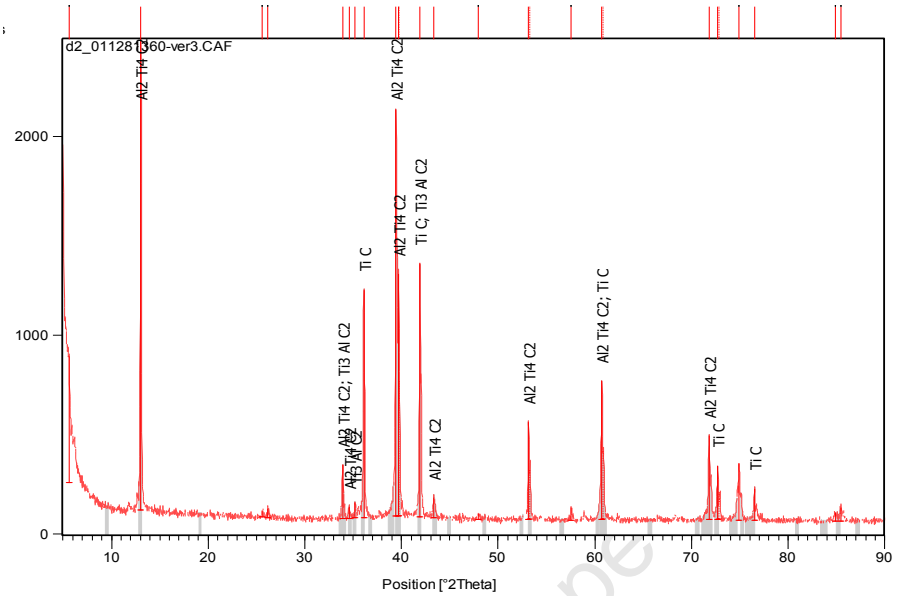

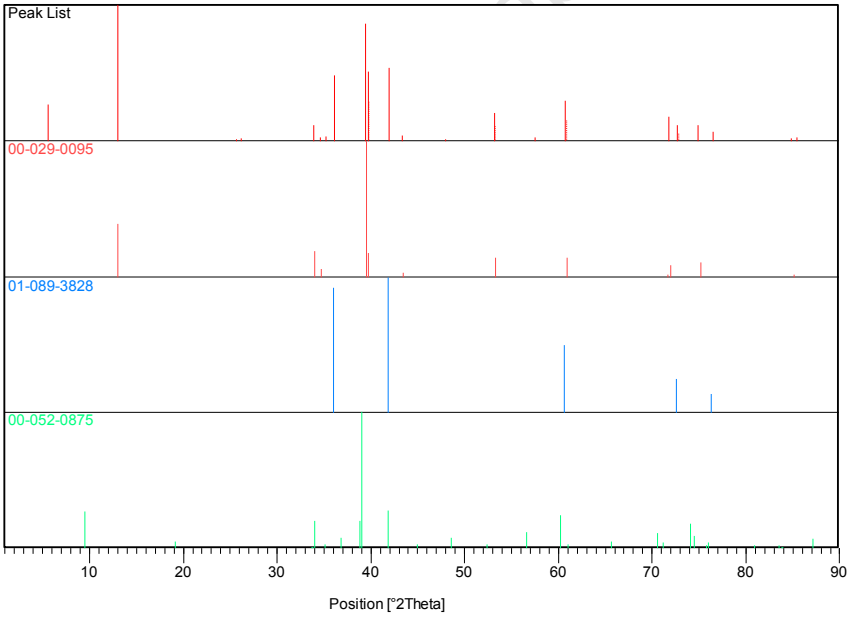

Visible	Ref. Code	Score	Compound Name	Displacement [°2Th.]	Scale Factor	Chemical Formula
*	00-029-0095	25	Titanium Aluminum Carbide	0.000	0.480	Ti_2AlC
*	01-089-3828	26	Khamrabaevite, syn	0.000	0.132	TiC
*	00-052-0875	11	Aluminum Titanium Carbide	0.000	0.053	Ti_3AlC_2

1300°C/120 minutes

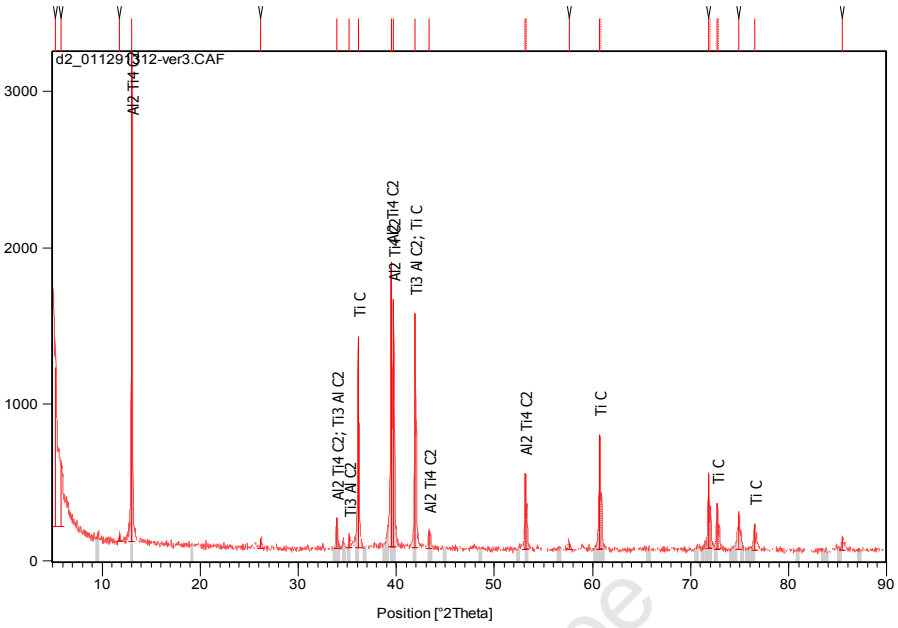

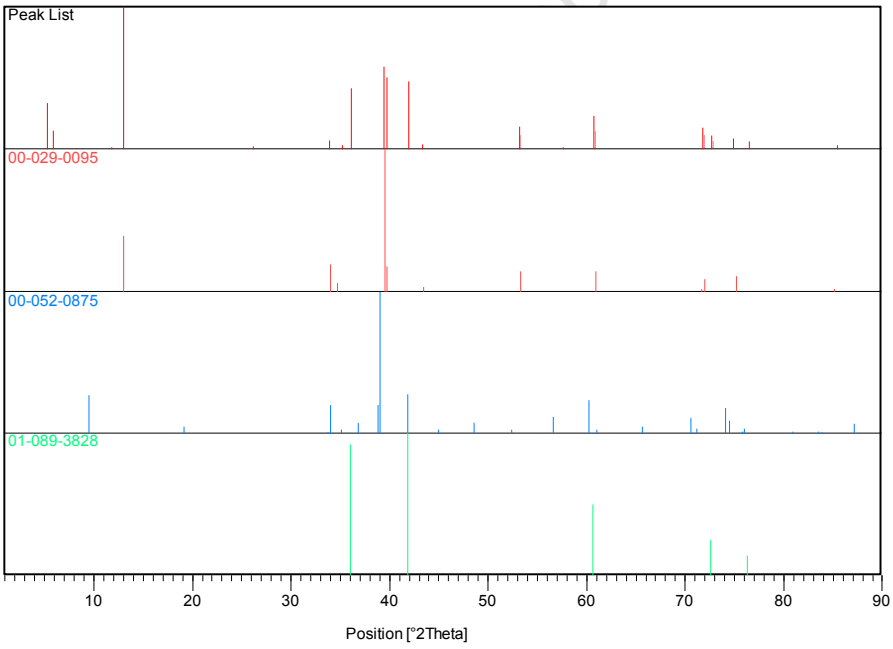

Visible	Ref. Code	Score	Compound Name	Displacement [°2Th.]	Scale Factor	Chemical Formula
*	00-029-0095	18	Titanium Aluminum Carbide	0.000	0.418	Ti_2AlC
*	00-052-0875	12	Aluminum Titanium Carbide	0.000	0.045	Ti_3AlC_2
*	01-089-3828	16	Khamrabaevite, syn	0.000	0.116	TiC

1400°C/60 minutes

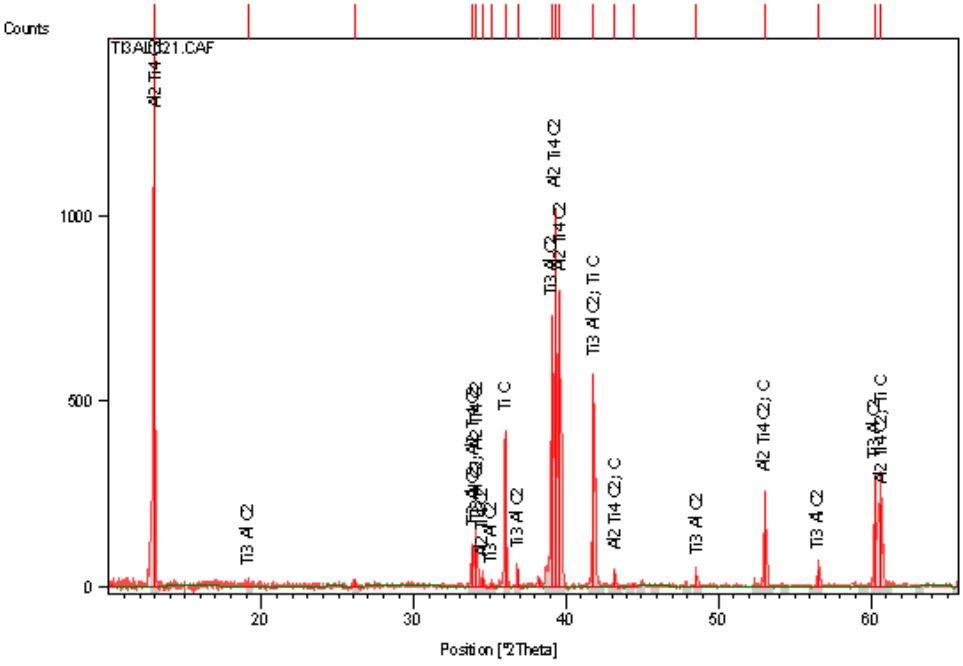

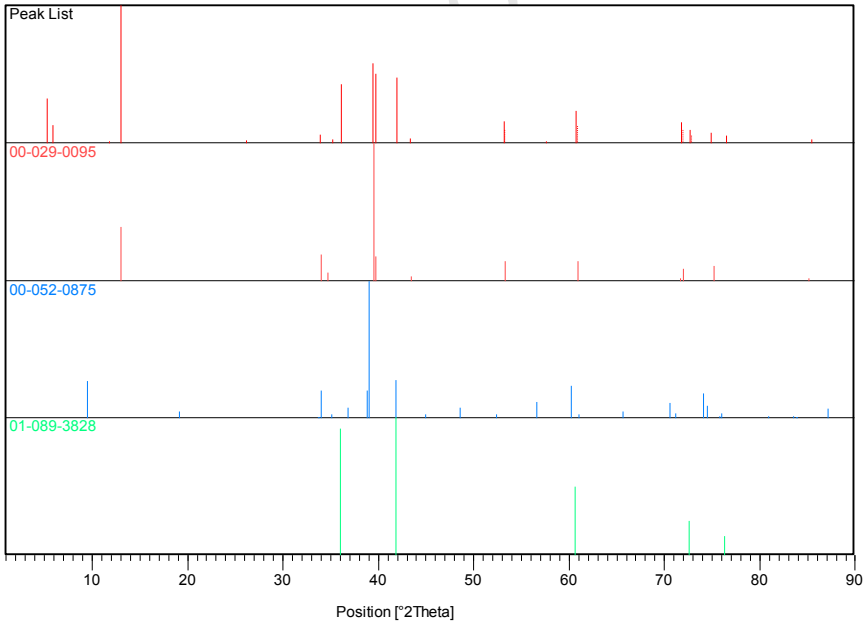

Visible	Ref. Code	Score	Compound Name	Displacement [°2Th.]	Scale Factor	Chemical Formula
*	00-029-0095	18	Titanium Aluminum Carbide	0.000	0.418	Ti_2AlC
*	00-052-0875	12	Aluminum Titanium Carbide	0.000	0.045	Ti_3AlC_2
*	01-089-3828	16	Khamrabaevite, syn	0.000	0.116	TiC

1400°C/120 minutes

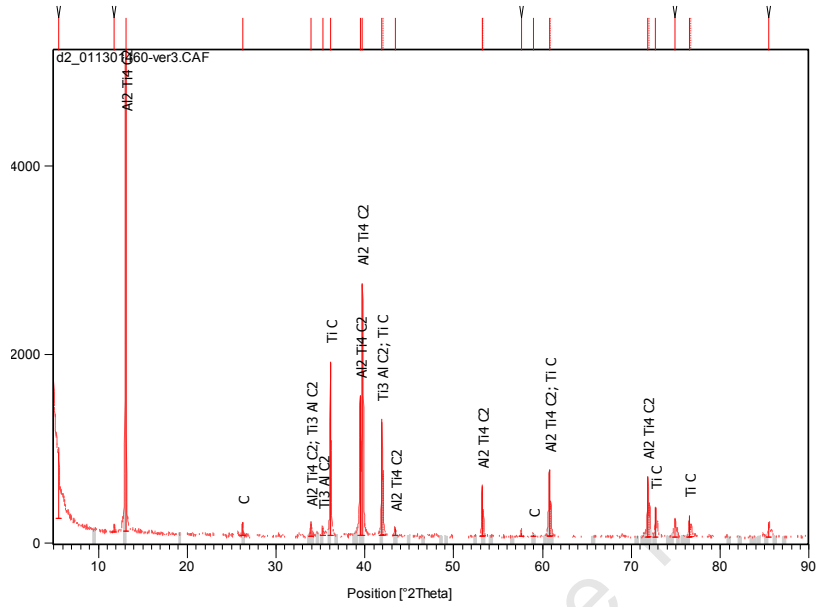

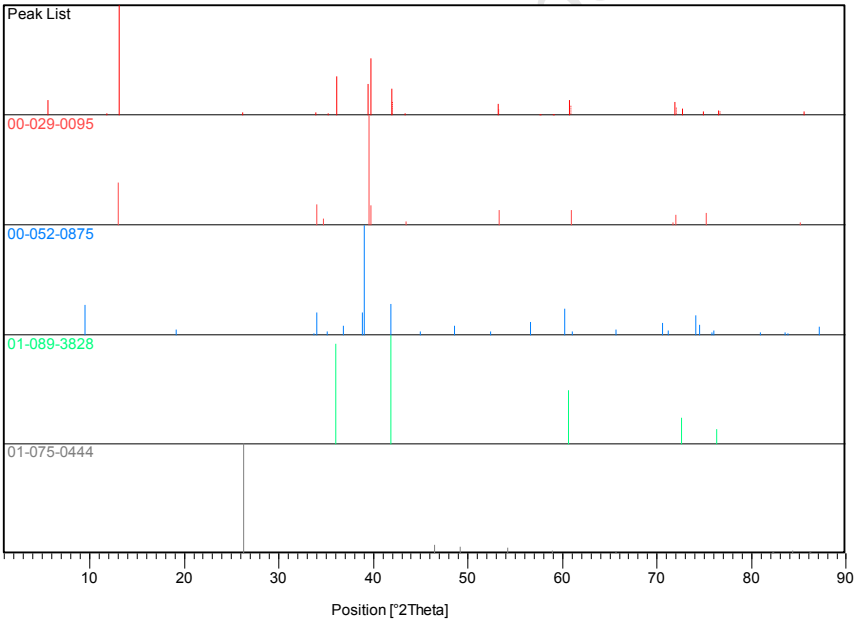

Visible	Ref. Code	Score	Compound Name	Displacement [°2Th.]	Scale Factor	Chemical Formula
*	00-029-0095	28	Titanium Aluminum Carbide	0.000	0.317	Ti_2AlC
*	00-052-0875	10	Aluminum Titanium Carbide	0.000	0.016	Ti_3AlC_2
*	01-089-3828	24	Khamrabaevite, syn	0.000	0.045	TiC
*	01-075-0444	7	Carbon	0.000	0.005	C

Ti_3SiC_2

1300°C/60 minutes

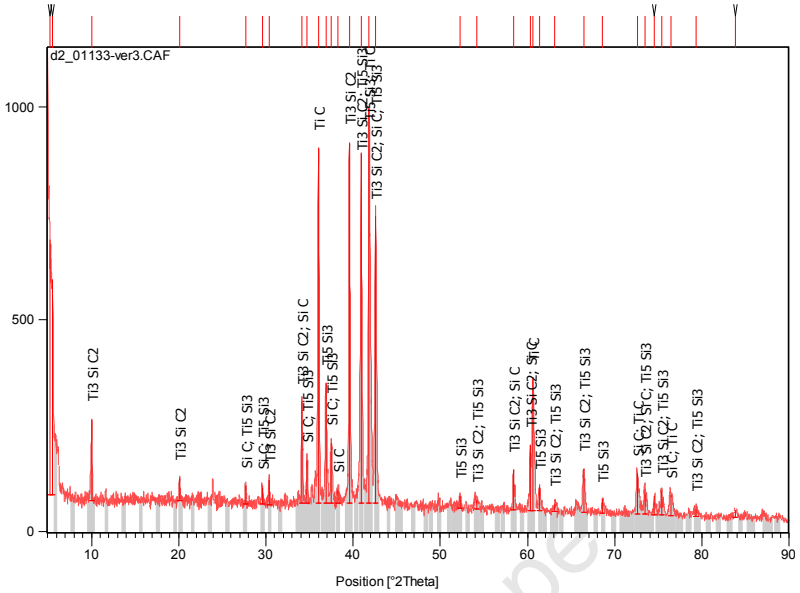

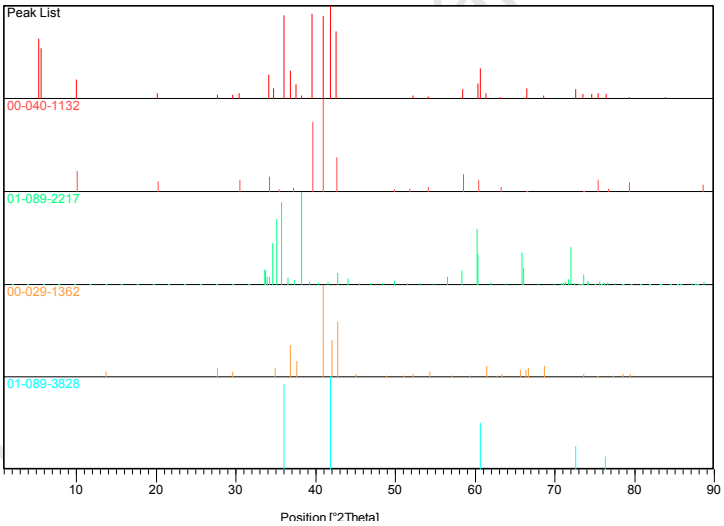

Visible	Ref. Code	Score	Compound Name	Displacement [°2Th.]	Scale Factor	Chemical Formula
*	00-040-1132	33	Titanium Silicon Carbide	0.000	0.499	Ti_3SiC_2
*	01-089-2217	21	Moissanite 18H - synthetic	0.000	0.066	SiC
*	00-029-1362	35	Titanium Silicon	0.000	0.569	Ti_5Si_3
*	01-089-3828	34	Khamrabaevite, syn	0.000	0.863	TiC

1300°C/120 minutes

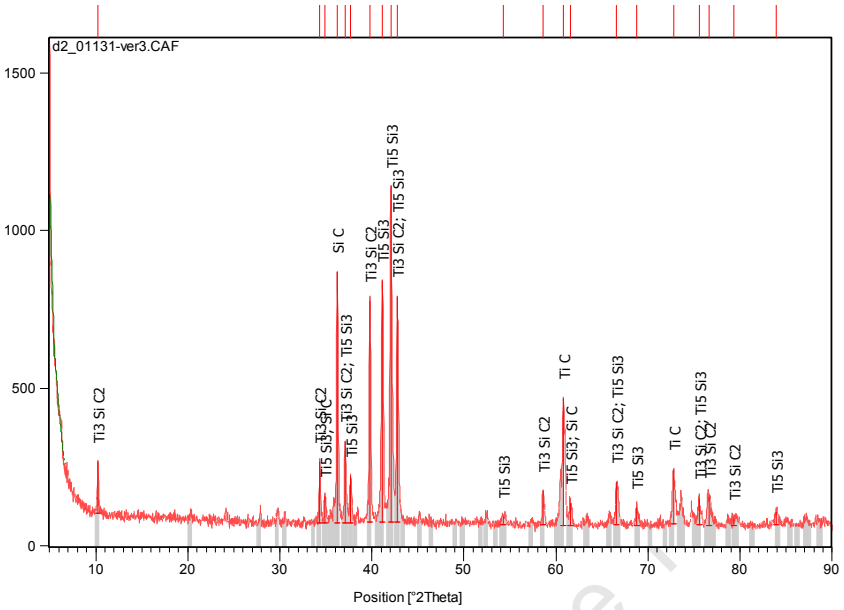

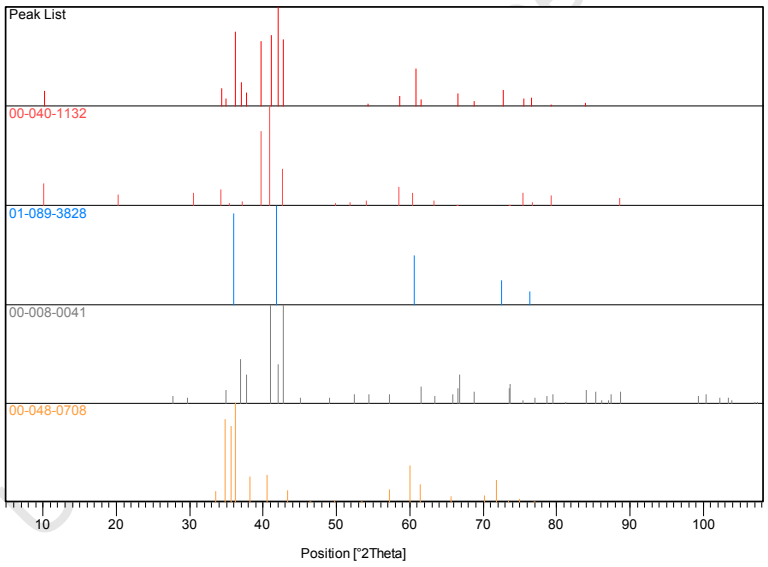

Visible	Ref. Code	Score	Compound Name	Displacement [°2Th.]	Scale Factor	Chemical Formula
*	00-040-1132	36	Titanium Silicon Carbide	0.000	0.225	Ti_3SiC_2
*	01-089-3828	21	Khamrabaevite, syn	0.000	0.083	TiC
*	00-008-0041	48	Titanium Silicon	0.000	0.529	Ti_5Si_3
*	00-048-0708	14	Moissanite-8\ITH\RG, syn	0.000	0.289	SiC

1400°C/60 minutes

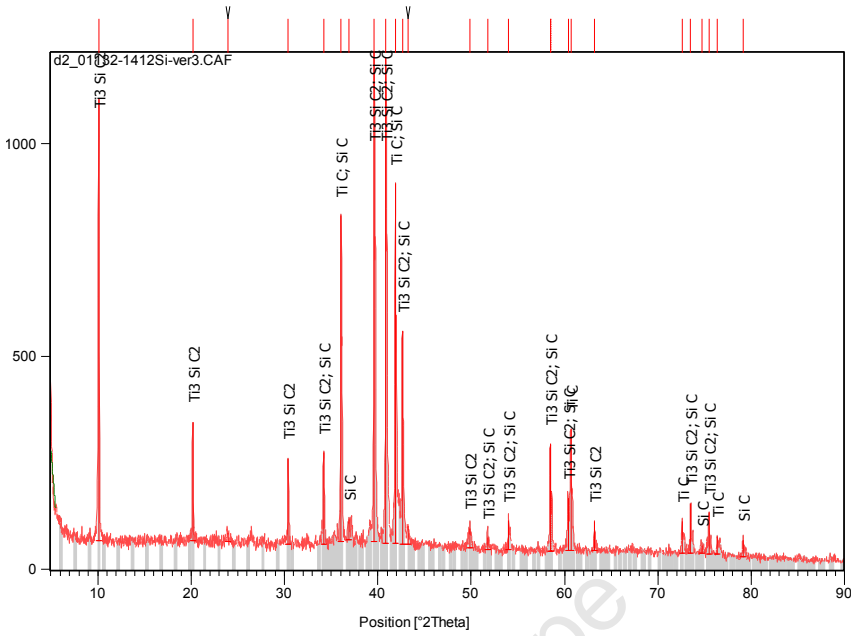

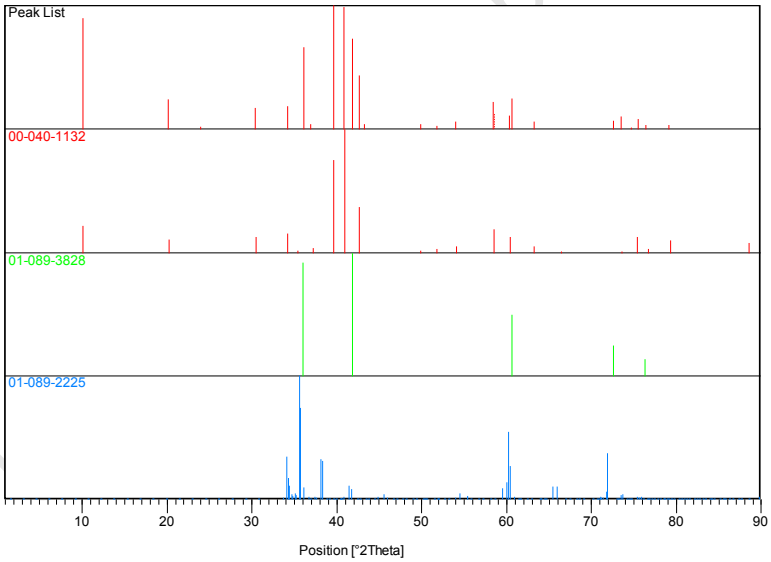

Visible	Ref. Code	Score	Compound Name	Displacement [°2Th.]	Scale Factor	Chemical Formula
*	00-040-1132	57	Titanium Silicon Carbide	0.000	0.721	Ti_3SiC_2
*	01-089-3828	34	Khamrabaevite, syn	0.000	0.219	TiC
*	01-089-2225	7	Moissanite 69R - synthetic	0.000	0.080	SiC

1400°C/120 minutes

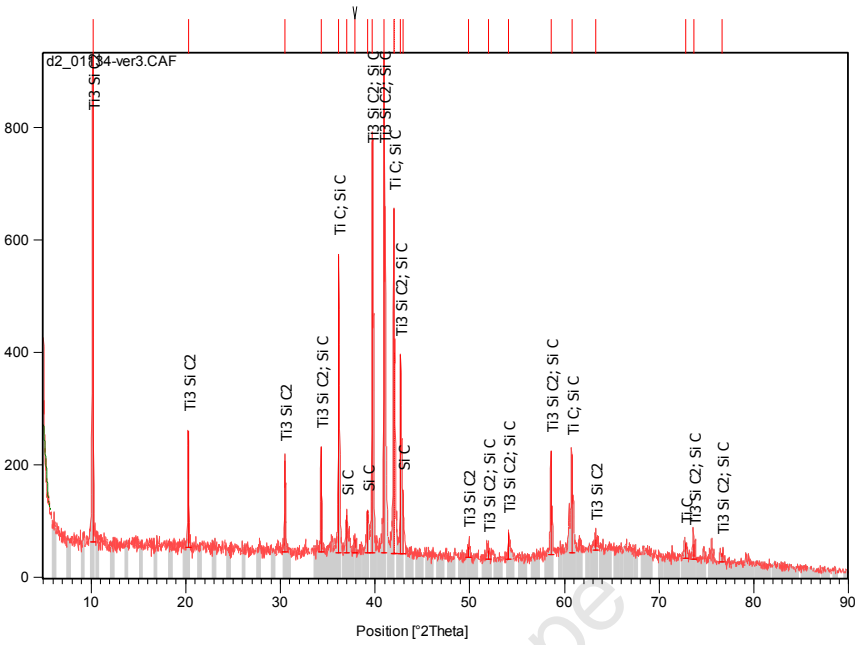

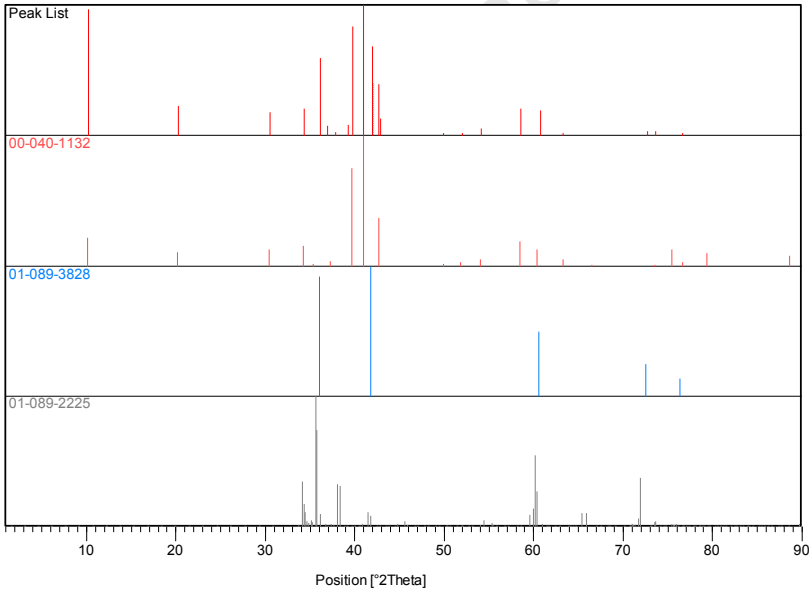

Visible	Ref. Code	Score	Compound Name	Displacement [°2Th.]	Scale Factor	Chemical Formula
*	00-040-1132	57	Titanium Silicon Carbide	0.000	0.502	Ti_3SiC_2
*	01-089-3828	20	Khamrabaevite, syn	0.000	0.046	TiC
*	01-089-2225	6	Moissanite 69R - synthetic	0.000	0.072	SiC

XRD for reaction couples

Ti_2AlC/cBN

1500°C, 30min, pressure less

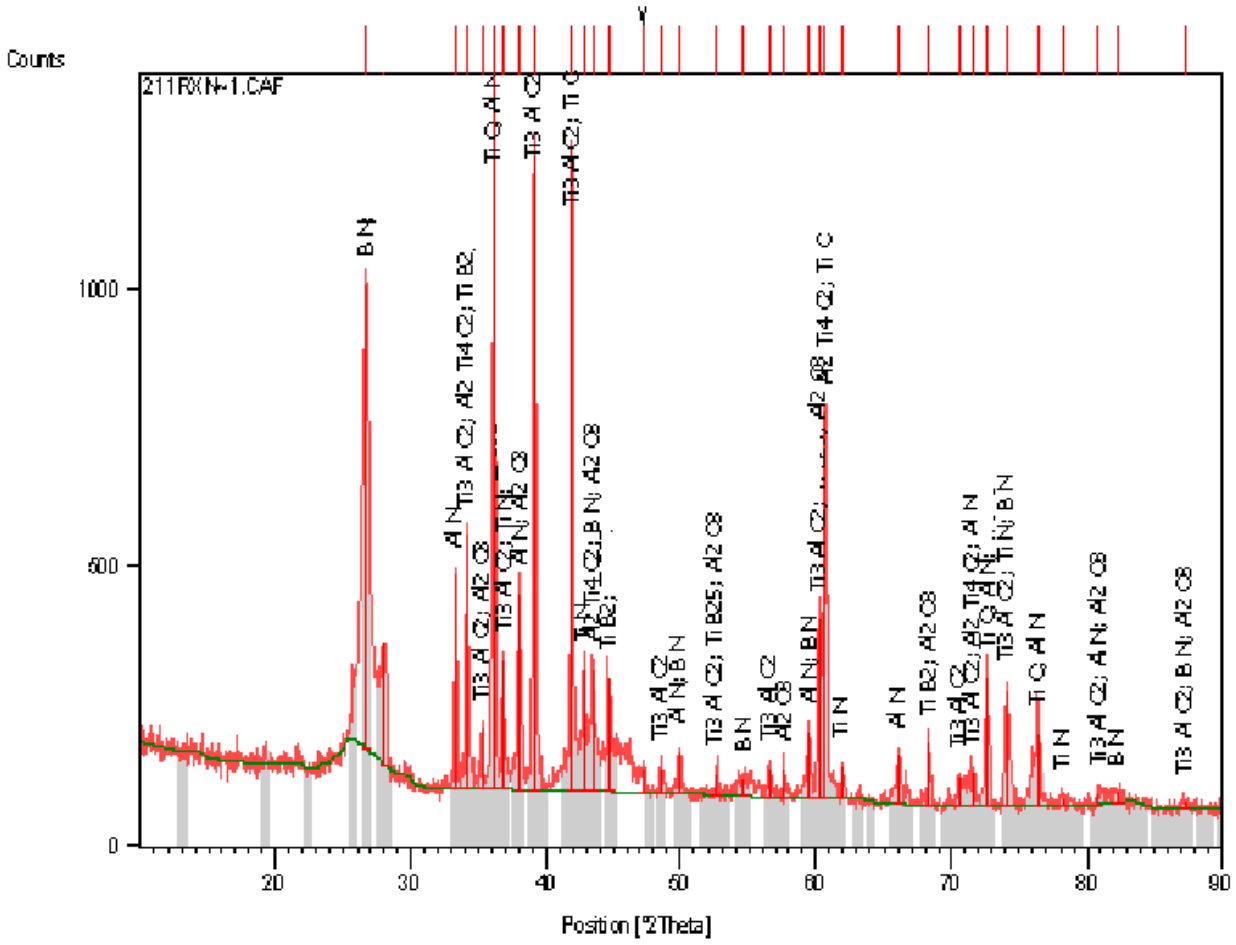

Visible	Ref. Code	Score	Compound Name	Displacement [°2Th.]	Scale Factor	Chemical Formula
*	00-052-0875	45	Aluminum Titanium Carbide	0.000	0.885	$Ti_3Al C_2$
*	00-029-0095	8	Aluminum Titanium Carbide	0.000	0.107	Ti_2AlC
*	01-089-3828	35	Khamrabaevite, syn	0.000	0.684	TiC
*	01-076-0565	36	Aluminum Nitride	0.000	0.371	AlN
*	01-087-0633	28	Osbornite, syn	0.000	0.094	TiN
*	00-035-1365	17	borazon	0.000	0.127	BN
*	01-085-1068	32	Boron Nitride	0.000	0.516	BN
*	00-008-0121	27	Boron Titanium	0.000	0.178	TiB_2
*	00-002-1227	21	Corundum	0.000	0.065	Al_2O_3

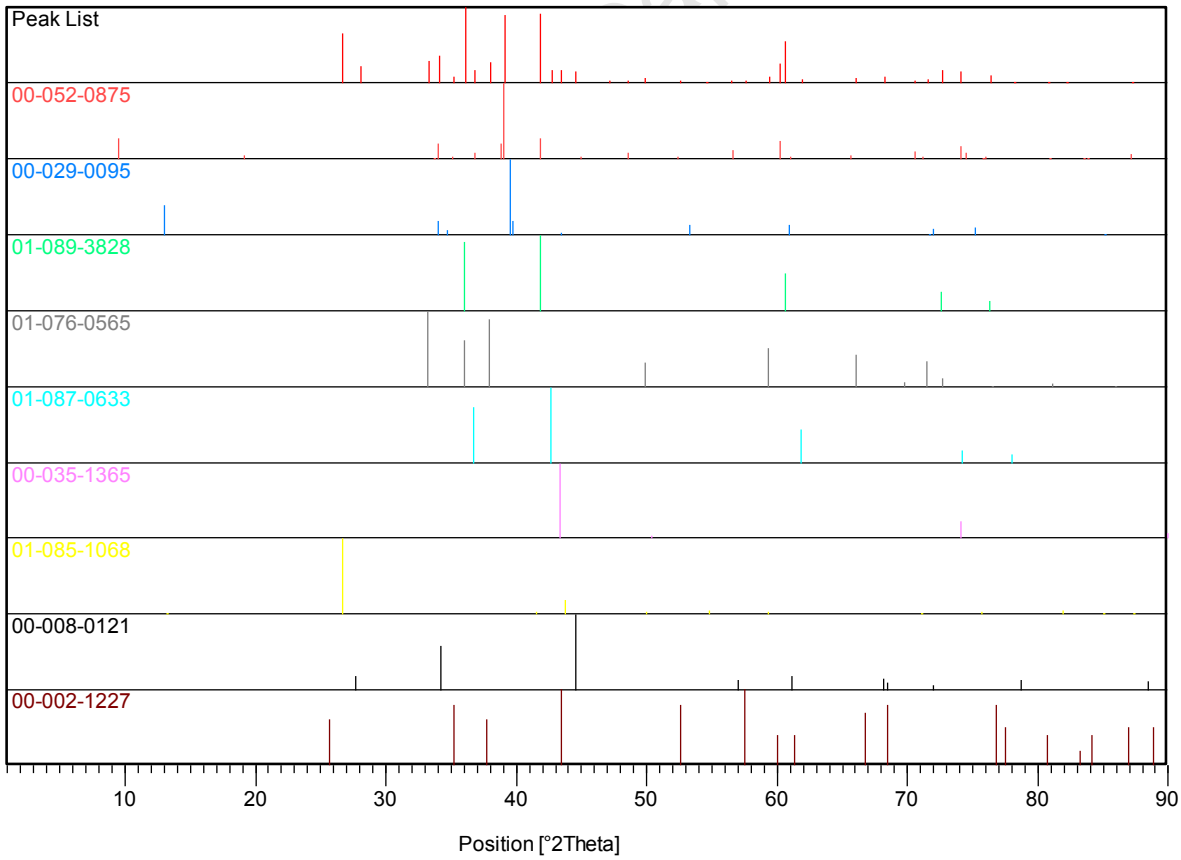

1500°C, 30min, 10MPa pressure

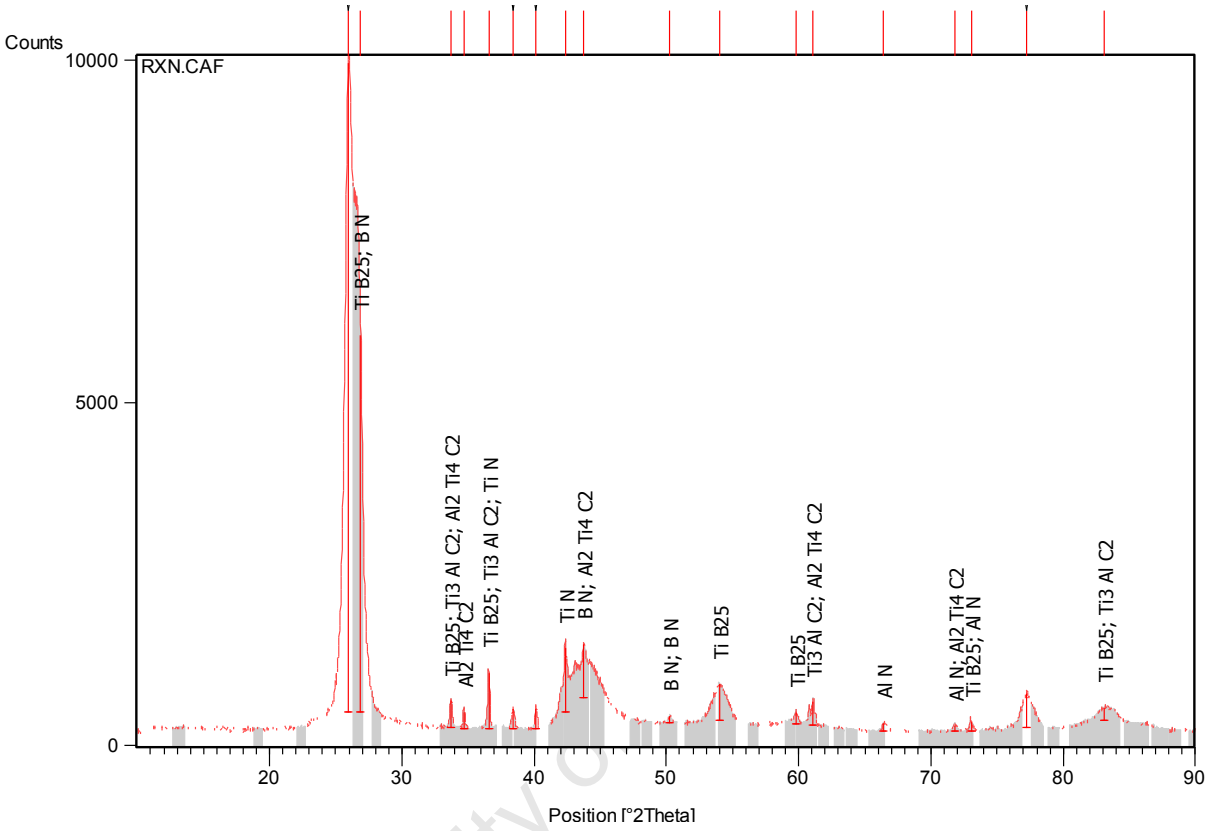

Visible	Ref. Code	Score	Compound Name	Displacement [°2Th.]	Scale Factor	Chemical Formula
*	00-035-1365	9	borazon	0.000	0.062	BN
*	00-052-0844	11	Boron Titanium	0.000	0.036	TiB_{25}
*	00-052-0875	6	Aluminum Titanium Carbide	0.000	0.011	Ti_3AlC_2
*	01-076-0565	10	Aluminum Nitride	0.000	0.006	AlN
*	01-085-1068	23	Boron Nitride	0.000	0.746	BN
*	01-087-0633	9	Osbornite, syn	0.000	0.031	TiN
*	01-089-3828	11	Khamrabaevite, syn	0.000	0.011	TiC
*	00-029-0095	6	Aluminum Titanium Carbide	0.000	0.134	Ti_2AlC

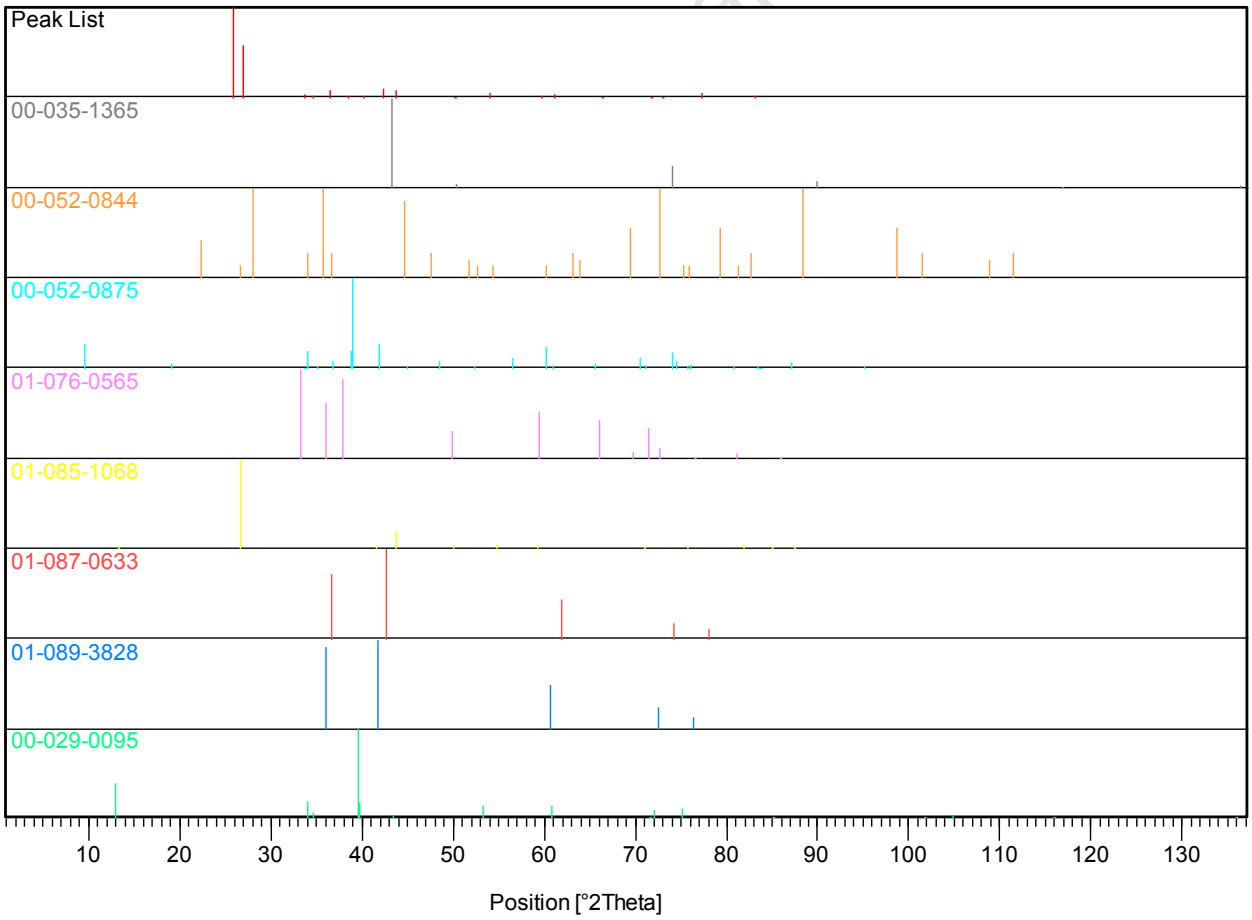

Ti_3SiC_2/cBN

1500°C, 30min, pressure less

Reacted cBN

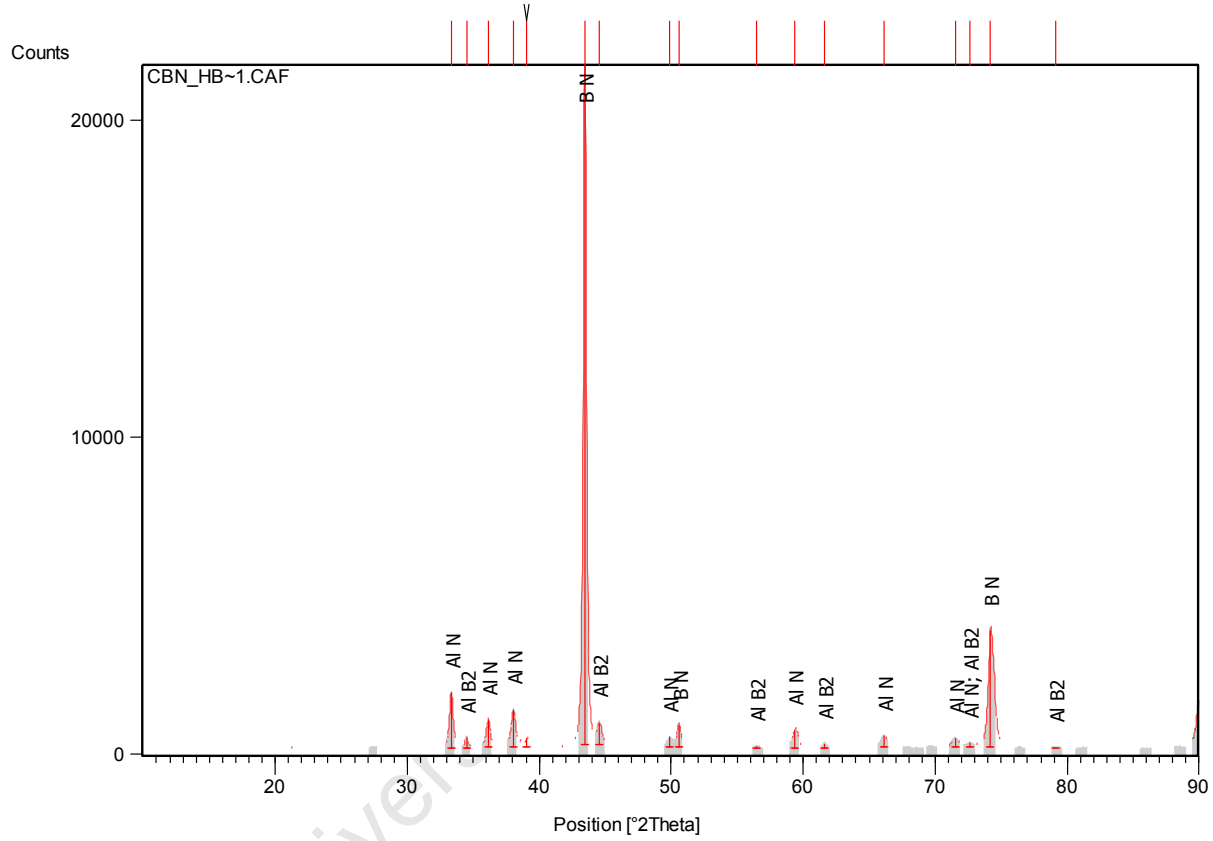

Visible	Ref. Code	Score	Compound Name	Displacement [°2Th.]	Scale Factor	Chemical Formula
*	01-075-1620	64	Aluminum Nitride	0.000	0.048	Al N
*	01-089-1498	33	Borazone	0.000	0.460	B N
*	00-065-3381	43	Aluminum Boron	0.000	0.028	Al B2

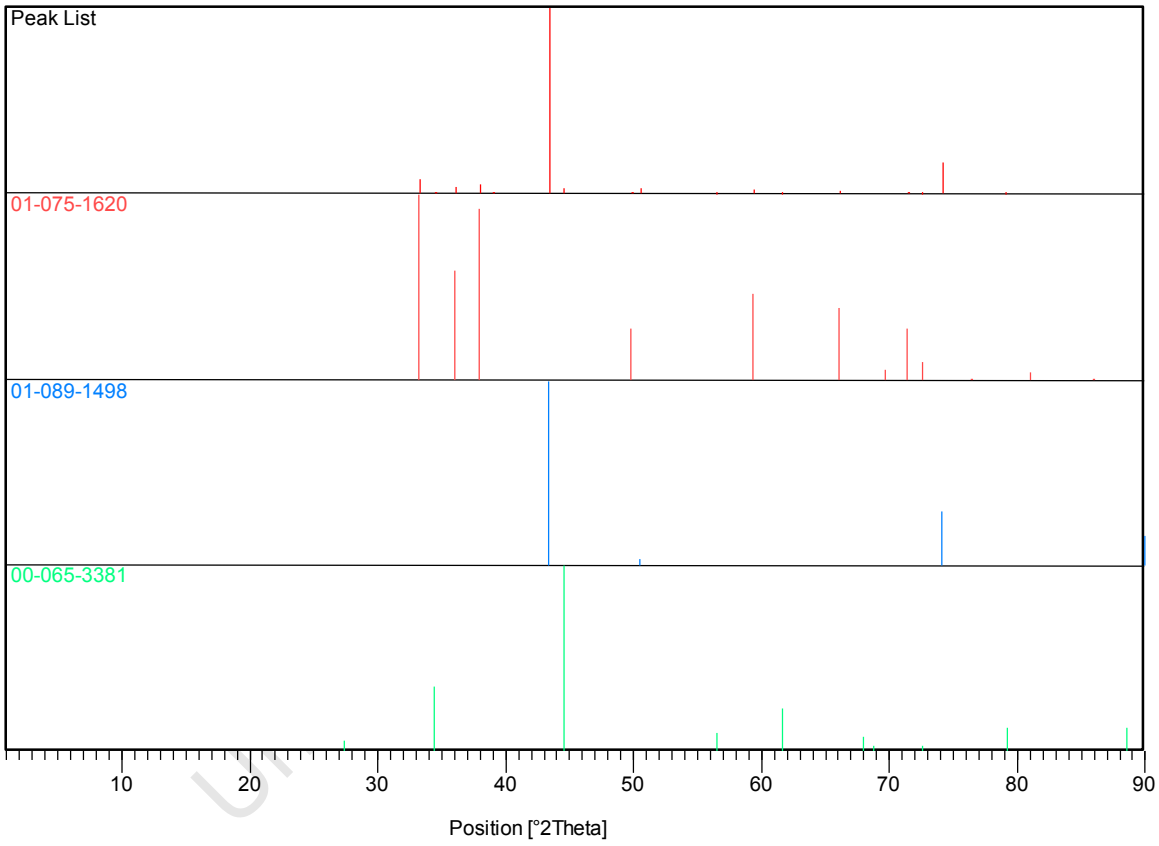

Reacted Ti_3SiC_2

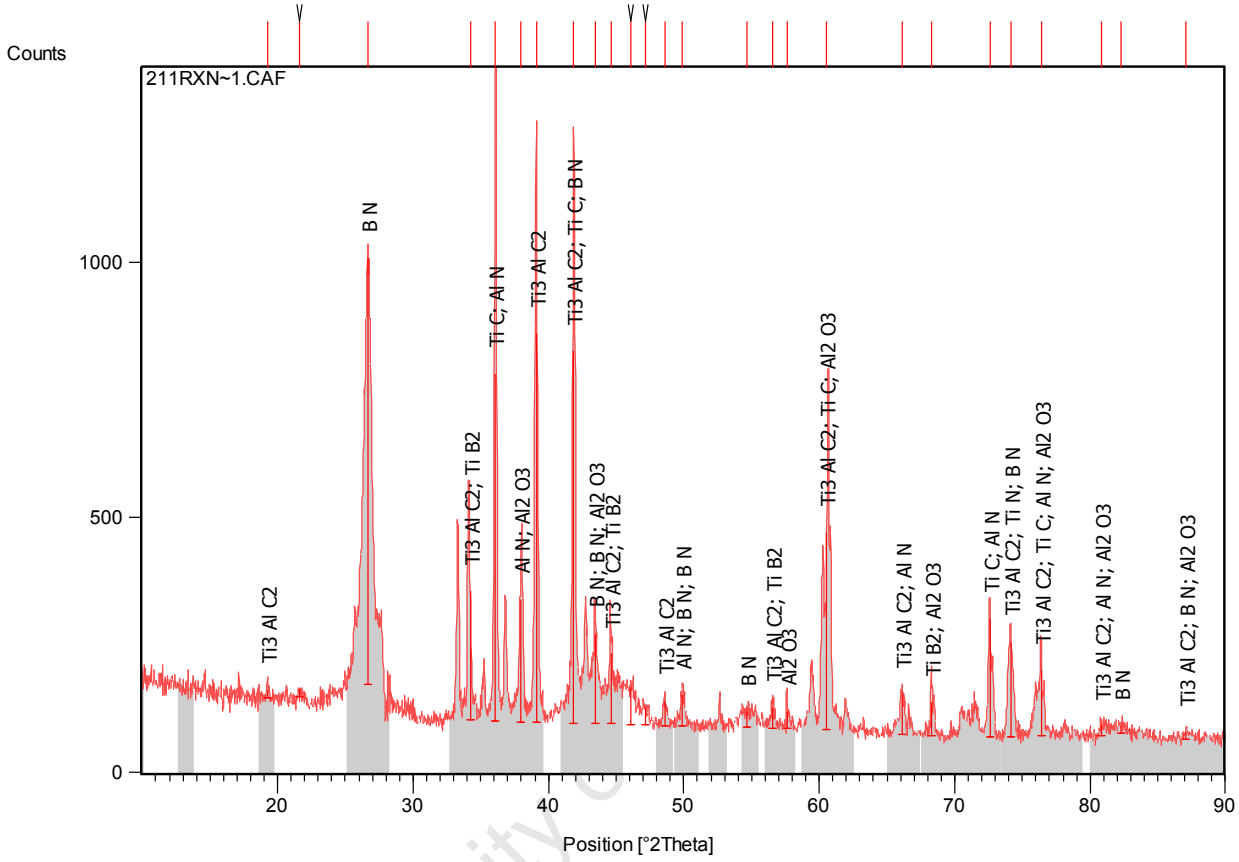

Visible	Ref. Code	Score	Compound Name	Displacement [°2Th.]	Scale Factor	Chemical Formula
*	00-052-0875	52	Aluminum Titanium Carbide	0.000	0.885	Ti3 Al C2
*	01-089-3828	42	Khamrabaevite, syn	0.000	0.684	Ti C
*	01-076-0565	31	Aluminum Nitride	0.000	0.371	Al N
*	01-087-0633	18	Osbornite, syn	0.000	0.094	Ti N
*	00-035-1365	22	borazon	0.000	0.127	B N
*	01-085-1068	40	Boron Nitride	0.000	0.516	B N
*	00-008-0121	34	Boron Titanium	0.000	0.178	Ti B2
*	00-002-1227	24	Corundum	0.000	0.065	Al2 O3

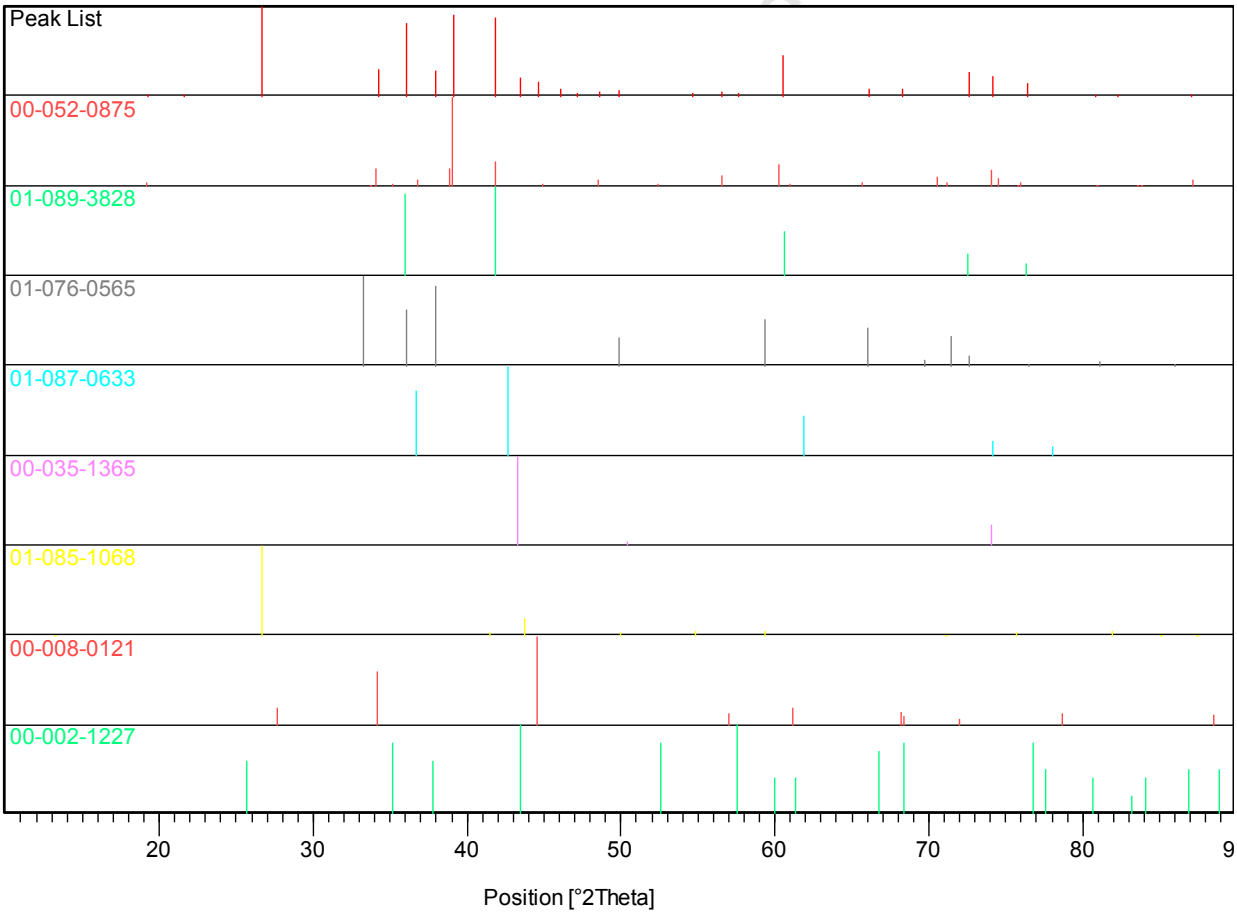

Non-reacted c-BN

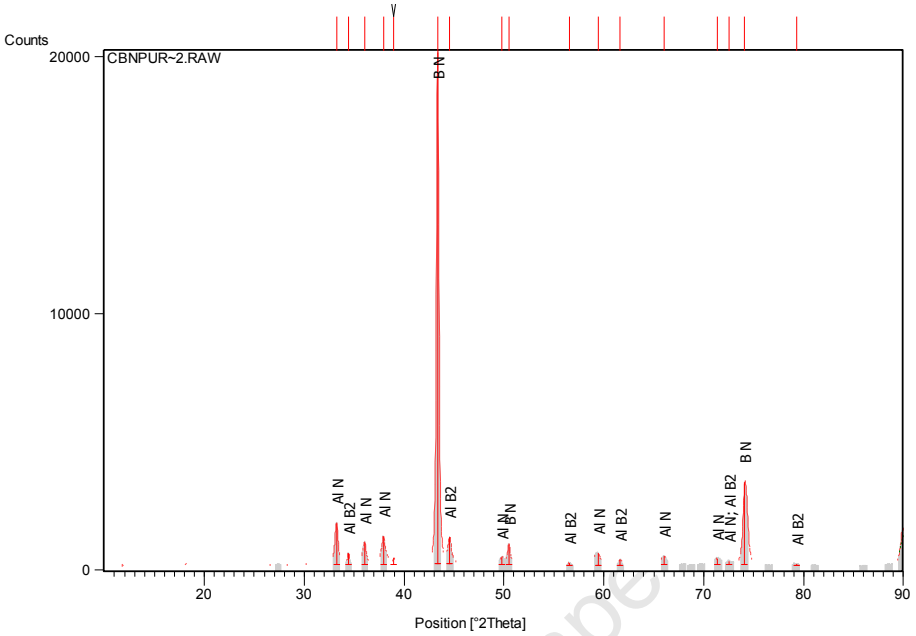

Visible	Ref. Code	Score	Compound Name	Displacement [°2Th.]	Scale Factor	Chemical Formula
*	01-076-0565	66	Aluminum Nitride	0.000	0.058	AlN
*	00-035-1365	41	borazon	0.000	0.939	BN
*	00-065-3381	48	Aluminum Boron	0.000	0.047	AlB_2

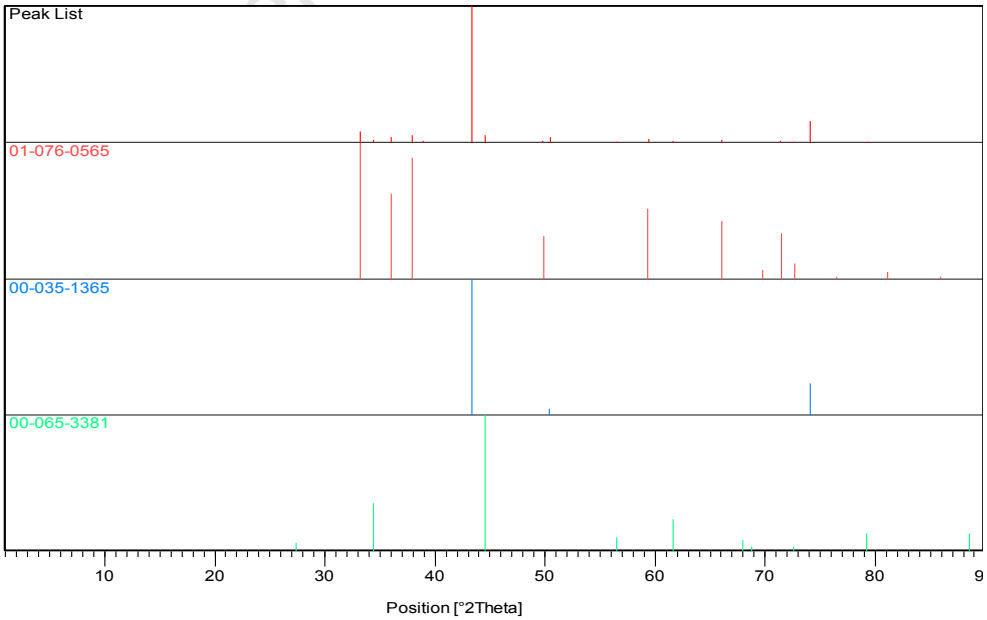

1400°C, 30min, 10MPa pressure

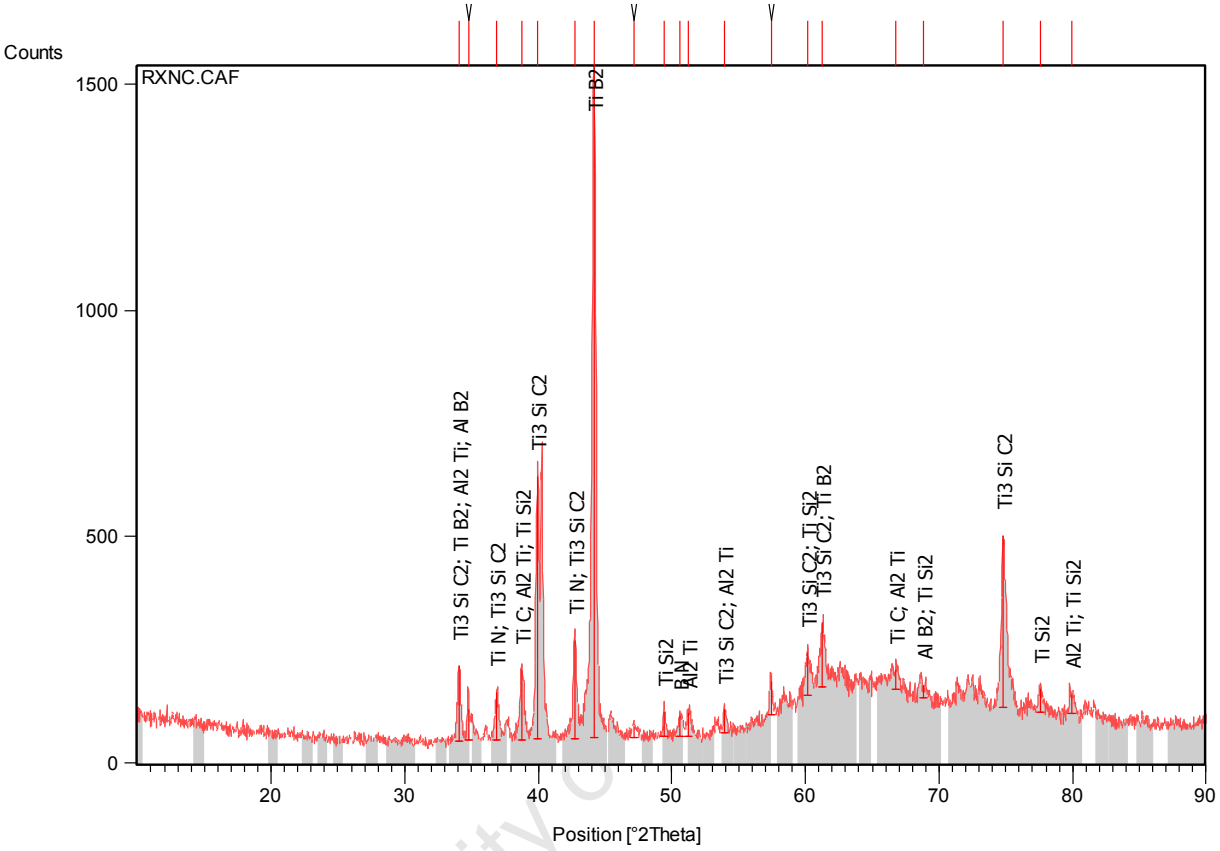

Visible	Ref. Code	Score	Compound Name	Displacement [°2Th.]	Scale Factor	Chemical Formula
*	00-006-0642	29	Osbornite, syn	0.000	0.080	Ti N
*	01-089-1356	28	Titanium Silicon Carbide	0.000	0.109	Ti3 Si C2
*	01-075-0967	17	Titanium Boron	0.000	0.071	Ti B2
*	00-035-1365	9	borazon	0.000	0.021	B N
*	00-002-0942	10	Titanium Carbide	0.000	0.030	Ti C
*	00-052-0861	16	Aluminum Titanium	0.000	0.030	Al2 Ti
*	00-039-1483	7	Aluminum Boron	0.000	0.057	Al B2
*	00-035-0785	16	Titanium Silicon	0.000	0.039	Ti Si2